

**Multiscale Modelling for Automotive
Exhaust-Gas Aftertreatment
– From the Quantum Chemistry to the Engineering Level**

DISSERTATION

submitted to the

Combined Faculties for the Natural Sciences and for Mathematics
of the Rupertus-Carola University of Heidelberg, Germany

for the degree of
Doctor of Natural Sciences

presented by

Oliver Richard Inderwildi, M.Sc.

born in Zurich, Switzerland

Examiners: Prof. Dr. Dr. h.c. Jürgen Warnatz

Prof. Dr. Olaf Deutschmann

Heidelberg, 15th of July 2005

Interdisziplinäres Zentrum für Wissenschaftliches Rechnen

Ruprecht - Karls - Universität Heidelberg

2005

DISSERTATION

submitted to the

Combined Faculties for the Natural Sciences and for Mathematics
of the Rupertus-Carola University of Heidelberg, Germany

for the degree of

Doctor of Natural Sciences

presented by

Oliver Richard Inderwildi, M.Sc.

born in Zurich, Switzerland

**Multiscale Modelling for Automotive
Exhaust-Gas Aftertreatment
– From the Quantum Chemistry to the Engineering Level**

Examiners: Prof. Dr. Dr. h.c. Jürgen Warnatz
Prof. Dr. Olaf Deutschmann

Abstract

In this work the behaviour of a novel automotive catalytic converter is theoretically investigated using a multiscale-modelling approach. Processes ranging from the nano-scale (chemical reactions) to the macro-scale (transient conversions in a single monolithic channel of a catalyst) are addressed by different modelling techniques. These independent techniques are combined in a hierarchical multiscale-modelling approach to yield a comprehensive model of an automotive catalytic converter.

The investigated rhodium-based exhaust-gas aftertreatment system converts poisonous nitrogen oxides (NO_x , $x = 1,2$) into nitrogen (N_2) in an oxygen-rich environment with short, oxygen-lean fuel-rich pulses (0.1 s – 5 s). Experimental investigations of NO_x and oxygen on stepped as well as low-index rhodium surfaces indicate that rhodium is inactive towards NO_x decomposition. Since oxygen decomposes much faster on any rhodium surface and is present in a vast excess, the rhodium surface should be blocked by oxygen rather instantaneously and, hence, inactive towards NO_x decomposition.

In order to achieve a more detailed comprehension of the relevant surface processes, surface reactions and diffusion of surface species were studied by means of quantum-chemical density functional theory (DFT) calculations. It was shown that the predominant plane in real fcc metal catalyst particles (111) is rather inactive towards NO dissociation. This is even more distinct when the surface is covered with oxygen to a high extent. Furthermore, it was shown that oxygen initially dissociates fast on this facet of rhodium, while this process is self-inhibiting; the activation barrier increases with increasing coverage. Charge analysis supports that these deactivation effects are due to the electron withdrawing effect of the electronegative oxygen precoverage in case of either decomposition reaction (O_2 and NO).

DFT investigations of monatomic steps, the most common defects on rhodium catalyst particles, showed that decomposition is more likely to occur here, while it is also deactivated by electron withdrawing coadsorbants. Furthermore, it was shown that even though electronic effects influence the probability of dissociation, steric effects are more important.

The qualitative knowledge gained by DFT investigation of surface processes was incorporated into time-dependent simulations of reactive flows using the computational tool DETCHEM^{TRANSIENT}. DETCHEM^{TRANSIENT}, a module of DETCHEM (O. Deutschmann *et al.*), which was developed as part of the presented work, simulates the transient behaviour of reactive flows based on a hierarchical modelling approach.

Time-dependent conversions calculated by DETCHEM^{TRANSIENT} based on elementary-step reaction mechanisms, which were improved significantly by knowledge gained from DFT calculations, could reproduce experimentally determined conversions.

It can be summarised that this thesis presents a significant step towards a detailed multiscale-modelling of automotive catalytic converters. In a comprehensive approach processes have to be described on different relevant levels from the microscopic to the macroscopic level, *i.e.*, from the quantum chemistry to the continuum engineering level. In particular, insight gained on the quantum-chemistry level can aid the understanding of processes on much higher length and time scales, if properly incorporated within a multiscale modelling approach.

Kurzfassung

Gegenstand der vorliegenden Arbeit ist die theoretische Untersuchung eines neuartigen Abgas-Nachbehandlungssystemes unter Verwendung eines Multiskalen-Modellierungsansatzes. Prozesse vom Nanobereich (chemische Reaktionen) bis zum Makrobereich (zeitabhängige Umsätze im katalytischen Einzelkanal) wurden durch verschiedene Modellierungstechniken beschrieben. Diese unabhängigen Techniken wurden im Rahmen eines Multiskalen-Modellierungsansatzes vereint, um ein umfassendes Modell eines Autoabgas-Katalysators zu erreichen.

Das untersuchte Rhodium-basierte Abgaskatalysator-System reduziert giftige Stickoxide (NO_x , $x = 1,2$) selektiv zu Stickstoff (N_2) in einem Sauerstoff-reichen Abgas, in welchem kurzzeitig (0,1 s – 5 s) reduzierende Bedingungen generiert werden. Experimentelle Untersuchungen von Stickoxiden und Sauerstoff auf gestuften und nieder-indizierten Rhodium-Oberflächen weisen darauf hin, dass diese Oberflächen Stickoxide nicht zersetzen können, da sie umgehend Sauerstoff-vergiftet sind.

Um ein genaueres Verständnis der relevanten Oberflächenprozesse zu erreichen, wurden Oberflächenreaktionen sowie Oberflächenmobilitäten mittels quantenchemischer Dichtefunktional (DFT)-Berechnungen untersucht. Es wurde gezeigt, dass die vorherrschende Oberflächenfacette auf Katalysatorpartikeln, die (111)-Oberfläche, relativ inaktiv bzgl. der NO-Zersetzung ist. Die Oberfläche wird zusätzlich durch die Präsenz einer Sauerstoff-Vorbelegung deaktiviert. Des Weiteren wurde gezeigt, dass Sauerstoff sich anfänglich sehr schnell auf Rhodium(111) zersetzt, während dieser Prozess selbsthemmend ist; die Aktivierungsenergie steigt mit steigender Sauerstoffbedeckung. Die Vermutung, dass die Deaktivierung in beiden Fällen (NO und O_2) auf die dem Rhodium Elektronen-entziehende Wirkung der Sauerstoffvorbelegung zurückzuführen ist, wird durch Ladungsanalysen unterstützt.

DFT-Untersuchungen von monoatomaren Stufen, dem häufigsten Defekt auf Katalysatorpartikeln, zeigten, dass die NO-Zersetzung hier wesentlich wahrscheinlicher ist, während der Prozess ebenfalls durch Sauerstoffvorbelegung deaktiviert wird. Es wurde aufgezeigt, dass, obwohl elektronische Effekte die Reaktionswahrscheinlichkeit beeinflussen, sterische Effekte einflussreicher sind.

Das qualitative Wissen, welches aus diesen DFT-Studien gewonnen wurde, war die Basis von zeitabhängigen Simulationen der reaktiven Strömung in Autoabgaskatalysatoren mittels DETCHEM^{TRANSIENT}. DETCHEM^{TRANSIENT} ist ein Modul von DETCHEM (O. Deutschmann *et al.*), welches als Teil der vorliegenden Arbeit entwickelt wurde. Es simuliert das instationäre Verhalten von reaktiven Strömungen mittels eines hierarchischen Modellierungsansatzes.

Zeitabhängige Umsätze simuliert durch DETCHEM^{TRANSIENT}, basierend auf Elementarreaktions-Mechanismen, welche durch DFT-Berechnungen optimiert wurden (s.o.), konnten experimentell bestimmte Umsatzkurven erfolgreich reproduzieren.

Die vorliegende Arbeit ist ein wichtiger Schritt zu einer detaillierten Multiskalen-Modellierung von Autoabgaskatalysatoren. In einem umfassenden Ansatz müssen Prozesse auf den relevanten Skalen vom Mikroskopischen zum Makroskopischen (von der Quantenchemie zum Strömungsverhalten) beschrieben werden. Im Speziellen konnten Erkenntnisse aus der Quantenchemie dazu beitragen, Prozesse auf höheren Zeit- und Längenskalen zu verstehen.

TABLE OF CONTENT

Chapter 1: Introduction.....	1
1.1 Catalysis	1
1.1.1 History	1
1.1.2 Influence	2
1.1.3 Concept.....	2
1.2 Catalytic Exhaust-Gas Aftertreatment	4
1.2.1 Environmental Pollution	4
1.2.2 Methods of NO _x , Soot and Simultaneous NO _x -Soot Removal	6
1.2.3 Content of this Thesis.....	10
1.3 Modelling and Simulation – Computer Aided Science.....	10
1.3.1 Multiscale Modelling – A Hierarchical Approach	11
1.3.2 Continuous Feedback Method	13
1.4 Scope of the Research	14
Chapter 2: Physical and Chemical Foundation	17
2.1 Quantum Mechanics.....	17
2.1.1 Schrödinger’s Equation	18
2.1.2 The Born-Oppenheimer Approximation	19
2.1.3 Density Functional Theory (DFT)	20
2.1.4 Hohenberg-Kohn Theorem.....	20
2.1.5 Implementation of DFT – The CASTEP Code	23
2.1.6 Bloch Theorem and Plane Waves	24
2.1.7 Pseudopotentials	26
2.1.8 Brillouin-Zone Sampling.....	27
2.1.9 Structural Optimisations with CASTEP.....	29
2.2 Reactive Flows.....	32
2.2.1 Microkinetic Simulations	34
2.2.2 Simulation of the Flow in Monolithic Reactors	40
2.2.3 Coupling of Microkinetic Simulations to CFD	45
2.2.4 Implementation – The DETCHEM Package.....	46
Chapter 3: Simulation of the Transient Behaviour of a Monolithic Channel	53
3.1 Motivation	53
3.2 Results and Discussion.....	54
3.2.1 Operation with Altering Feed Composition	54
3.2.2 Comparison of the Outlet Gas Composition with Experimental Data.....	55
3.2.3 Time Resolution of the Surface Coverage	57
3.2.4 Nitrogen Monoxide Reduction by Hydrogen Pulsing.....	60
3.3 Conclusions	63
Chapter 4: Carbon-Monoxide-Adsorption and -Coadsorption on Rhodium(111)	65
4.1 Motivation	65
4.2 Results and Discussion.....	65
4.2.1 Carbon Monoxide on Rhodium(111).....	65
4.2.2 Carbon Monoxide and Atomic Oxygen on Rhodium(111).....	68
4.2.3 Electron Donation from the Surface to the Adsorbant.....	70
4.3 Conclusions	71

Chapter 5: Coverage Dependence of the Oxygen Decomposition.....	73
5.1 Motivation	73
5.2 Results and Discussions	73
5.2.1 Clean Rhodium and Molecular Oxygen.....	74
5.2.2 Molecular Oxygen on Rh(111).....	74
5.2.3 Decomposition Process	77
5.3 Conclusions	84
Chapter 6: Coverage Dependence of the Nitrogen Oxide Decomposition	87
6.1 Motivation	87
6.2 Results and Discussion.....	87
6.2.1 Nitrogen Oxide on Rhodium(111).....	87
6.2.2 Oxygen Coverage Dependence of the NO Adsorption on Rhodium(111).....	90
6.2.3 NO Decomposition over Rhodium(111) and Oxygen Influence.....	92
6.3 Conclusions	97
Chapter 7: Surface Diffusion on Rhodium(111)	101
7.1 Motivation	101
7.2 Results and Discussion.....	101
7.2.1 Diffusion of Atomic Species	101
7.2.2 Diffusion of Molecular Species	105
7.2.3 Overview	107
7.2.4 Coverage Dependence of the Oxygen Single-site Jump.....	107
7.3 Conclusions	108
Chapter 8: Nitrogen Monoxide Dissociation on Stepped Surfaces	111
8.1 Motivation	111
8.2 Results and Discussion.....	111
8.2.1 Rhodium(331) Plane	111
8.2.2 NO Dissociation on Rhodium(331)	112
8.2.3 NO Dissociation in Presence of Oxygen.....	115
8.2.4 NO Dissociation in Presence of Further Coadsorbants.....	117
8.3 Conclusions	118
Chapter 9: Influence of Coverage-Dependent Kinetics on the Catalyst Behaviour	119
9.1 Motivation	119
9.2 Results and Discussion.....	120
9.2.1 Oxygen Flow with CO pulses - Revisited.....	120
9.2.2 NO Reduction and Nitrogen Formation - Revisited	125
9.2.3 Influence of a Coverage-Dependent Kinetic Parameter on the NO-Oxidation.....	127
9.3 Conclusions	129
Chapter 10: Conclusion and Outlook.....	131
References	133
Appendices	141
Appendix A: Reaction Mechanism	141
Appendix B: Atom Colouring in Surface Visualisations (Chapters 4 to 8).....	143
Appendix C: Catalyst characterisation & Experimental Techniques (Chapters 3 & 9).....	144

Chapter 1: Introduction

1.1 Catalysis

1.1.1 History

The expression “catalysis” stems from the Greek word for “dissolve”. It was first understood by the Swedish chemist Berzelius that the addition of a certain compound accelerates a reaction even though the compound is not consumed in the reaction [1]. Yet catalysis was already widely applied; without knowing, mankind utilised catalytic processes such as fermentation for thousands of years. Nature applies sophisticated biocatalysts (enzymes) ever since there is life [2]. Enzymes enable for instance the human body to synthesise elaborate compounds at benignant conditions (*e.g.*, $T \sim 37^\circ \text{C}$, $\text{pH} \sim 7$). The synthesis of the same compounds in an organic chemistry laboratory would require harsh conditions (*i.e.*, high T , strong acid/ base etc.).

At the turn of the 18th century, it was observed that metals and oxides assist the decomposition of various chemical compounds. In subsequent studies it was noticed that also the selectivity of decomposition reactions could be controlled by additives. In 1834 Faraday assumed that adsorption of the reactants on the solid catalyst surface was crucial for the activity of the catalytic additive [1]. Faraday’s and Berzelius’ observations were brought into a coherent picture by Ostwald (Nobel Prize 1909), who concluded that a catalyst does not affect the thermodynamics of an equilibrium, nevertheless affects the reaction rate. Ostwald’s basic definition of catalysis is still valid [1].

1.1.2 Influence

Catalysis is and will continue to be the cornerstone of the chemical industry [1]. Nowadays, almost no product is manufactured without at least an indirect participation of a catalytic process. The influence of catalytic processes such as Haber and Bosch's ammonia synthesis on the world population cannot be neglected [3]. But not only the chemical and the pharmaceutical industry, but also car manufacturers employ catalysts. Even though traffic increased continuously in recent years, the pollution stagnates, the emission of certain pollutants even decreases. The influence of automotive exhaust-gas aftertreatment on our environment is explained in more detail in Section 1.2.

1.1.3 Concept

The concept of catalysis is to open up reaction pathways, which would not be possible in the absence of a catalytic component such as a metal or an acid. The essence is that the catalytic component lowers the energy barriers for certain reactions by enabling an alternative pathway. Even though the catalyst is involved in the chemical reaction it stays per definitionem chemically unaffected in the global reaction. Hence the catalyst can undergo the same reaction over and over again.

Catalysis can roughly be divided in homogeneous catalysis where catalyst as well as substrates are in the same phase [4] – either gaseous or liquid – and heterogeneous catalysis where the catalyst is – in general – solid and substrates react at the solid interface or inside a porous structure [5, 6].

This thesis will focus on heterogeneous catalysis, more precisely in automotive exhaust-gas aftertreatment [7, 8]. The aim of automotive exhaust-gas aftertreatment is the conversion of environmentally harmful compounds such as carbon monoxide and nitrogen monoxide to non-hazardous compounds as preferably nitrogen and carbon dioxide according to Reaction Equation 1.1.



The NO molecule adsorbs on the metal surface and the metal assists in the bond breaking, meaning, it unclothes an alternative reaction pathway with a lower activation energy (Figure 1.1, left). This may be as follows: After the bond breaking the atomic oxygen on the surface reacts with an adsorbed CO molecule to form the non-toxic CO₂ (Figure 1.1, blue arrow). The N atom combines with another N to form molecular nitrogen (red arrow). This elementary-step reaction mechanism on a metal surface is shown in Figure 1.1.

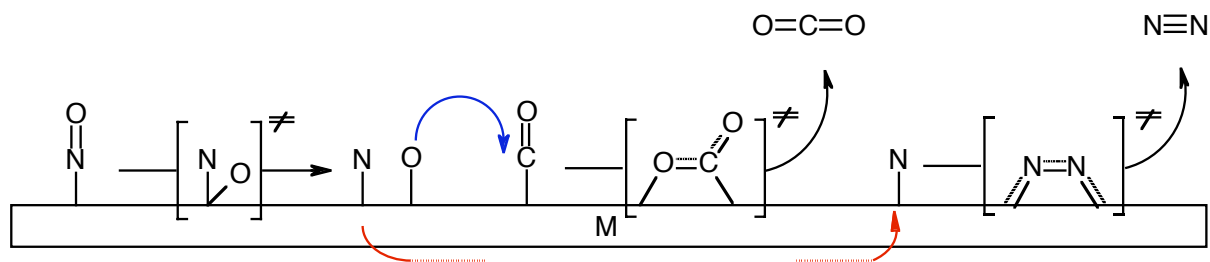


Figure 1.1: Elementary-step mechanism of the NO decomposition and CO oxidation on rhodium

As can be seen from Equation 1.1, one pollutant is removed by use of the other and conversely, pointing out the sophistication of the principle of nowadays automotive catalysts [8]. Moreover, the composition of the exhaust gas as well as its temperature is given by the operation conditions of the internal combustion engine and the aftertreatment facilities are subject to these constraints. Minor changes in exhaust-gas composition for a limited time are the only concessions made by motor management.

One topic investigated in this thesis is the determination of activation energies for reactions on transition metal catalysts aiming towards the generation of input parameters for microkinetic simulations. In Section 1.4 it will be outlined how this approach can be exploited for a completely computational description of the processes in a monolithic catalysts from the quantum chemistry level (length scale in the order of 10^{-10} m) up to the chemical engineering level (length scale in the order of meters).

Computational modelling of catalytic processes cannot only add to experimental investigations, but can in some places substitute expensive experiments. *E.g.*, when conditions are explored that are difficult to investigate experimentally (*e.g.*, extremely high temperatures, pressures or a combination of both) simulations can provide information, while experimental data are not reliable [9].

1.2 Catalytic Exhaust-Gas Aftertreatment

1.2.1 Environmental Pollution

Environmental pollution is one of the consequences of the energy provision by combustion of fossil fuels. Nevertheless, this type of energy recovery is the main reason for prosperity and mobility in industrial countries. Most energy is provided by internal combustion engines as applied in nowadays motor vehicles. The main pollutants emitted by these internal combustion engines are the green house gases nitrous oxide (N_2O) and carbon dioxide (CO_2), the toxic carbon monoxide (CO), carcinogenic soot as well as harmful nitrogen oxides (NO_x). Furthermore, volatile organic compounds (VOC) and sulphur compounds such as sulphur dioxide (SO_2) are emitted. Meanwhile those emissions have led to a variation of the composition of the earth's atmosphere. This in turn has led to effects such as global warming, the consequent deglacification of the earth's poles, smog, acid rain and tropospheric ozone [10].

To control further atmospheric defilement by street traffic, the US federal state of California – as a precursor – enacted a law in 1976 that restricted the amount of toxic pollutants emitted by motor vehicles. European legislation measured up to those limits in 1985, and they could be met by applying the well-known 3-way catalyst to the exhaust gas. The 3-way-catalyst oxidises hydrocarbons (1st way) as well as carbon monoxide (2nd way) and reduces NO_x ($x = 1,2$) (3rd way) leading to near-zero emissions for these pollutants [11]. The disadvantages of this exhaust-gas aftertreatment system are that it is only efficient in a narrow range around stoichiometric conditions ($\lambda \sim 1$) and only at elevated temperatures ($> 550 \text{ K}$). Figure 1.2 shows pollutant conversions as functions of the λ -value in a three-way catalyst.

However, not only the toxic pollutants affect the earth's atmosphere, but also the green house gases carbon dioxide and nitrous oxide. Since these compounds are inert, they cannot be simply converted. Hence, measures for their abatement must be taken prior to the catalytic converter. Since a reduction of carbon dioxide production is conterminous with a reduction of fuel consumption, the efficiency of the internal combustion engines has to be optimised. Combustion engines with a higher degree of efficiency are engines that are operated under

oxidising conditions such as the Diesel engine or lean-run gasoline¹ engines. The disadvantage of those engines is that considerable amounts of nitrogen oxides are emitted and soot is formed.

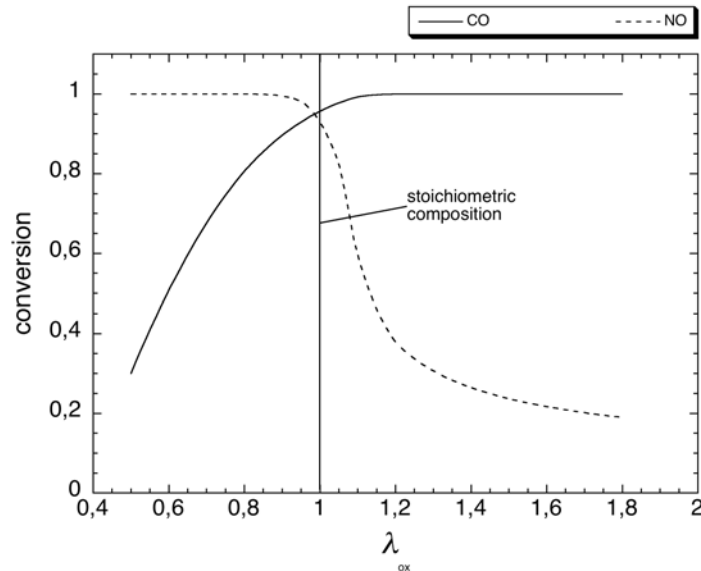


Figure 1.2: Pollutant conversions in a three-way catalyst as functions of the λ -value, comparison between simulation (lines) and experiments (points), 1 denotes 100% conversion [12]

Owing to this and the health risk exposed by those pollutants, European legislation has introduced strict emission limits. Following first restrictions in the 1990s, the Euro-3 norm was introduced in 2000. This restriction is followed up by Euro-4 in the beginning of 2005. The Euro-5 norm is due in either 2008 or 2010. In case of particle emission this corresponds to an emission reduction by a factor of 20 in 10 years, see Figure 1.3.

The conventional 3-way catalyst is not applicable here, because the conditions are too oxidising (too high λ value), see Figure 1.2. Therefore, special NO_x -reduction systems and methods to eliminate soot from the exhaust-gas are developed at present. In the case of the nitrogen oxide removal it has to be mentioned that it is a challenging task to chemically reduce a compound in an oxygen rich environment. Therefore, several approaches to remove

¹ To be more precise: inhomogeneously operated gasoline engines such as the FSI (VW) or the GDI (Mitsubishi) engine

NO_x and soot from the exhaust-gas were suggested and are partially already applied in modern automobiles (see subsequent paragraph).

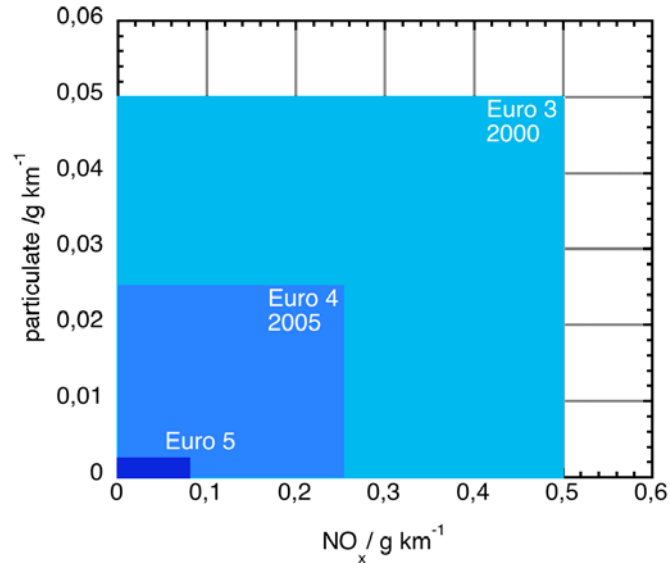


Figure 1.3: European Union pollutant emission restrictions; the maximum NO_x emission is plotted on the abscissa, the maximum soot particle emission is plotted on the coordinate

1.2.2 Methods of NO_x , Soot and Simultaneous NO_x -Soot Removal

a NO_x Removal

Reduction Catalyst (SCR, HC-SCR)

One of the first suggestions how to reduce NO_x in an oxidising environment was to add an excess of ammonia to the exhaust gas (SCR method; selective catalytic reduction) [8, 13]. Ammonia reduces NO_x selectively to nitrogen catalysed by a mixture of metal oxides while the excess is reduced to nitrogen and oxidised to NO_x by oxygen (the latter is again reduced). Since it is dangerous to transport larger amounts of gaseous ammonia in an automobile, ammonia has to be generated *in-situ* from urea by thermohydrolysis. Liquid urea would have to be provided at least at a percentage of filling stations, meaning an expensive infrastructure is required for this solution of the NO_x problem.



The SCR method is especially advantageous for heavy-duty vehicles, which emit vast and strongly varying amounts of NO_x . By using additives for the reduction of NO_x , these variations can be compensated by the additive dosing and hence in case of heavy-duty vehicles, the SCR method is the most likely solution to the NO_x problem. Recently, the SCR method is also considered for application in passenger vehicles, because alternative approaches appear not to be sufficient to comply with Euro-V criteria.

An analogue approach that would avoid the addition of a reducing agent is the selective catalytic reduction of NO_x with hydrocarbons (HC-SCR) emitted by the combustion engine itself. Investigation of the HC-SCR over platinum showed that this system converts NO_x very well, however, not to the desired nitrogen, but to the greenhouse gas nitrous oxide. Further studies with metal oxides could improve the activity and the selectivity, but could not exhibit the performance of the ammonia counterpart though [8].

Storage Reduction Catalyst

A conceptual different approach is to store NO_x inside the catalyst – NO_x storage catalyst (NSC). This can be accomplished by adding a component to the catalyst that forms nitrites and nitrates when exposed to NO_x , *e.g.*, metal oxides such as barium oxide [13]. As soon as almost all storage material is converted to nitrites and nitrates, the storage component has to be regenerated. This is achieved by switching the engine conditions to fuel-rich conditions for a short period. Owing to the fuel-rich conditions, more CO_2 is formed, and the nitrogen oxide compounds of barium are replaced by the thermodynamically more stable barium carbonate [14]. The nitrogen oxides released are subsequently reduced under the currently fuel-rich (reducing) conditions. The catalyst is then again able to store nitrogen oxides under lean conditions. The crucial drawback is that this system is poisoned rapidly when sulphur-containing compounds are present. Since the petroleum manufacturing industry is not able to reduce the sulphur content of gasoline beneath 5 ppm, this has become a major restriction for

the application of NSCs, especially in the case of fuel-consuming SUVs² and limousines. For smaller cars, such as for instance the Volkswagen Lupo, special regeneration cycles for the sulphur poisoning (analogue to the storage regeneration) have been implemented into the electronic motor management (Motronic).

Nakatsuji Decomposition Catalyst

A promising approach for a sulphur-resistant DeNO_x catalyst was suggested by Nakatsuji [15, 16]. A rhodium-based zeolitic catalyst operated alternately under short lean (time scale in the order of seconds) and very short rich (time scale in the order of 0.1 s) conditions appeared to be sulphur-resistant while highly active towards nitrogen oxide decomposition. The major drawback of this emission control system is that it deteriorates for reasons not completely understood yet. Furthermore, the surface chemistry of this system can barely be linked to the global behaviour of the catalyst. This system is one of the topics of the Competence Network Catalysis (ConNeCat) initiated by the German Federal Ministry for Education and Research (BMBF) and will be discussed in detail in this thesis.

b Soot Removal

Diesel Particulate Filter

A device for the particulate removal from automotive exhaust gases, the Diesel particulate filter (DPF) developed by PSA International, is permanently present in the media these days. This system successfully removes even very small particles (which are the most carcinogenic) from the exhaust gas. The filter is, as the NSC, regenerated by a post-injection that creates a temporary fuel-rich environment in the exhaust gas stream. In case of the DPF the soot particles are removed from the filter by flame cleaning. The major drawback of the DPF system is that the filter creates a higher counterpressure, and this lowers the degree of efficiency of the engine. Since the high degree of efficiency is the reason for the promotion of lean-run engines, the DPF system can only be a temporary solution because it is

² Sport utility vehicles

counterproductive. German car manufacturers, for instance, could reduce the amount of particles emitted by inner motor measures, a Japanese system is explained later.

c Simultaneous NO_x-Soot Removal

Advanced Particulate Filter

The most advantageous means to remove the two main pollutants – NO_x and soot – would be the utilisation of one type of pollutant as reductant for the other type. Kureti *et al.* showed that iron-containing oxidic structures, coated on a common particulate filter, can effectively remove NO_x and soot simultaneously [17]. Furthermore, this system is highly selective towards the production of nitrogen over a broad temperature range with a maximum at ~450°C. These types of catalysts are also a main focus of the research carried out within the ConNeCat project parallel to the Nakatsuji NO_x decomposition system.

Diesel Particulate NO_x Reduction

The currently supreme system for the removal of pollutants from the exhaust gas of oxygen-rich exhaust gases is the D-Cat (Diesel clean advanced technology) system by Toyota. This system removes NO_x as well as soot to a high degree from the exhaust gas utilising a Diesel particulate NO_x reduction (DPNR) system and engine electronical control of exhaust-gas recirculation as well as combustion. The D-Cat system is absolutely sulphur-resistant. In case of a 2 l Diesel engine with 86 kW the D-Cat system is able to reduce the NO_x emitted to 50 % of the Euro-4 limit while the amount of particles emitted could be reduced to 10 % of the Euro-4 emission maximum.

Non-Catalytic Approach – Plasma Reactor

The only promising non-catalytic approach to purify automotive exhaust gases applies a plasma source. The exhaust gas is lead through a reactor with a non-thermal plasma inside. Collisions of the exhaust gas molecules with the high-energetic electrons of the plasma generate radicals, which initiate chain reactions involving mainly pollutants. While hydrocarbons are converted to carbon dioxide and water, NO is mainly oxidised to NO₂. As

long as this method is not improved with regard to NO_x decomposition, a catalytic system for this process would still be required [18-20].

1.2.3 Content of this Thesis

Aim of this thesis is to support the development of the emission control units presented in this section by means of computer modelling. Since processes in an automotive catalytic converter are complex and occur on different time and length scales, these cannot be addressed by a single theoretical description, new approaches have to be considered.

1.3 Modelling and Simulation – Computer Aided Science

A computer simulation is the performance of a computer program, which attempts to describe a certain system by solving equations resulting from an abstract, simplified model of it. In short, computers try to imitate real systems.

Especially in science and engineering, computer simulation has become an important method to obtain more insight into a certain aspect. Computer models are based on a theoretical, mathematical description of a specific system. Comparing a computer simulation based on a certain theoretical description with measurement of the real system can be used to evaluate either theory or experiment. The most common type of simulation is the numerical solution of differential equations, which cannot be solved analytically.

Computer simulations became more and more popular with the rapid growth of computer processor speed. While high-end computer systems were necessary to model small systems in the 1980s, today common personal computers can solve quantum-mechanical problems or calculate the behaviour of transient reacting flows.

Most theoretical approaches describe closed systems at certain length and time scales. However, as soon as a real system is to be described, one has to consider processes at different time and length scales. Since there is no theoretical description that covers all phenomena over all time and length scales, a hierarchical approach has to be adopted, see following paragraph.

1.3.1 Multiscale Modelling – A Hierarchical Approach

Computer modelling has the potential to provide new insights into processes that are relevant for catalytically active systems such as reaction pathways, diffusion or flow. For example, quantum-mechanical configuration predictions combined with the simulation of spectroscopic data, can bring information from many different experimental techniques into a coherent picture. Owing to this a fruitful dual-feedback mode, where experiments are used to validate modelling results and modelling results are used to explain experimental observations and suggest new experiments, was established recently.

The behaviour of a real catalytic system is complex, and the processes that determine it span over a wide range of time and length scales. Since many of these processes interact, it makes the simulation of real catalysts extremely challenging.

For example, consider the processes in an automotive converter from the entrance of the exhaust gas into the monolithic catalyst to its outlet. Molecules first have to enter into the catalyst, adsorb in its washcoat, diffuse through the pores of washcoat to adsorb on the catalytically active component. On this component the molecule might decompose, [15, 16] diffuse until it reacts with another molecule, or desorbs again. The product molecule has to traverse the converse pathway to get back into the exhaust gas stream. Length scales of these processes span from 10^{-10} meters (catalytic site) to decimetres (chemical reactor) and the time scales span from femtoseconds (surface reactions) to minutes or even minutes (long-time temperature behaviour) [21]. Since for the time being a computational approach, which addresses all these issues en bloc is inconceivable, one has to adopt a hierarchical approach.

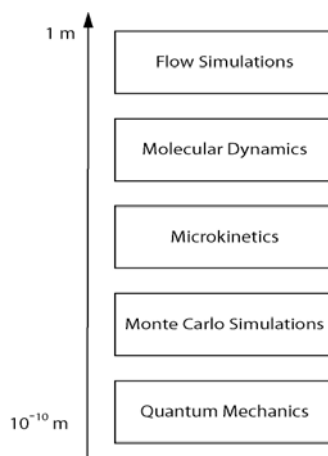


Figure 1.4: Hierarchical approach to multiscale modelling

In this approach different computational methods for different time as well as length scales are utilised. Linking these results together answers questions from the atomic to the macroscopic level. This approach is illustrated in Figure 1.4.

At the most detailed level of description, electronic structure calculations are utilised to predict adsorption energies and activation energies of surface reactions. Using, *e.g.*, density functional theory (DFT) calculations (see Chapter 2) one can predict preferred surface geometries and simulate spectroscopic data for comparison with spectroscopic data of the real catalytic system to gain more insight into the relevant processes.

Moreover, diffusion coefficients can be determined by calculating the activation energy for single-site jumps of molecules and atoms. These informations are again input parameters for Dynamical Monte-Carlo (DMC) simulations of the catalytically active surface. DMC methods are – among many possibilities – a way to resolve a surface in 2 dimensions utilising a stochastic procedure. The surface is resolved using a two-dimensional grid; every grid point represents an adsorption site and the occupancy of the adsorption site is filed. The probability of a single-site jump is expressed in terms of the activation energy for the process; the lower the activation barrier, the more likely the surface-site jump. These activation energies can be taken from DFT calculations. Herewith, the time evolution of the surface can be calculated using this stochastic DMC method based on knowledge gained from DFT calculations.

An advantage of DMC models is that the local environment of the adsorbate is included explicitly, while the mean-field approach (see below) considers the surface as well as the distribution of the adsorbants to be uniform. The two-dimensional resolution is especially advantageous when reactions occur at certain inhomogenities of the surface, *e.g.*, at steps or kinks.

Furthermore, by calculating the potential energy surface (PES) of surface transformations (see Chapter 2) kinetic parameters can be determined. Herewith elementary-step reaction mechanisms can either be developed or evaluated. Whenever competing reaction pathways have to be considered, the energetically more favourable can be identified using these tools. The elementary-step reaction mechanisms improved by DFT investigations are in turn input for microkinetic simulations, *e.g.*, based on a mean field approach, a method were the surface is considered to be uniform and the adsorbants to be randomly distributed.

At the longest time and length scales, engineering modelling approaches such as fluid dynamics calculations are used to calculate global, macroscopic properties of a catalyst, based on microkinetic calculations (DMC or mean-field). *Nota bene*: Since information on a certain

scale is obtained while processes on other time scales proceed, feedback between the different levels of the hierarchical model is absolutely crucial.

1.3.2 Continuous Feedback Method

In Figure 1.5 an example for information exchange in such a continuous feedback method – the simulation of the temperature evolution of a monolithic catalyst – is given. Flow simulation provides microkinetic simulation of the heterogeneous chemistry with gas-phase concentrations above the catalytically active surface. These gas-phase concentrations are the basis for microkinetic simulations. The production/consumption of species on the surface as well as the composition of the surface overlayer is calculated. Production and consumption of species are again input parameters for flow simulation. Furthermore, flow simulations provide the simulation of the thermal behaviour of the catalyst with the heat source terms. These heat source terms are in turn utilised by the simulation tool for the thermal behaviour to calculate the temperature profile of the catalyst. The calculated temperature profile is again utilised by the flow simulation.

Furthermore, flow simulations provide the simulation of the thermal behaviour of the catalyst with the heat source terms. These heat source terms are in turn utilised by the simulation tool for the thermal behaviour to calculate the temperature profile of the catalyst. The calculated temperature profile is again utilised by the flow simulation.

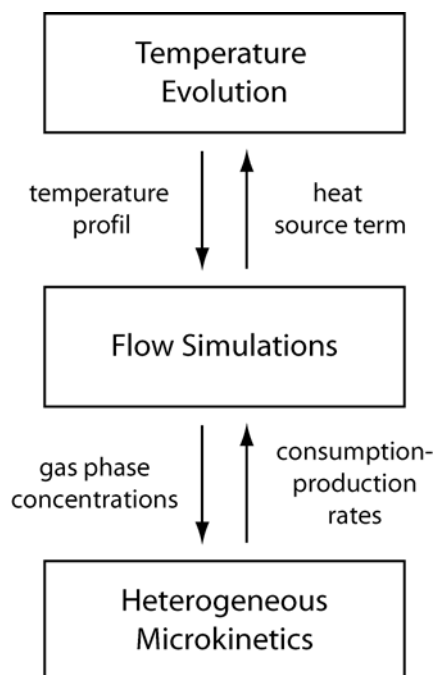


Figure 1.5: Continuous feedback method for hierarchical modelling

The processes are described from the microscopic (heterogeneous reactions) to the macroscopic (thermal behaviour). The temperature and the distribution of the flow field are slow in comparison to chemical processes on the surface and are therefore considered to be steady-state during the microkinetic simulation. The thermal evolution of the monolith is slow in comparison to the flow through the monolith and, therefore, the temperature profile is considered constant during flow simulations.

Nevertheless, the temperature profile and the distribution of the flow field are crucial for the correct calculation of the kinetics. Moreover, temperature as well as production and consumption of species are vital for calculating the distribution of the flow field correct. Hence, it is crucial for this multiscale approach that these information are available for each modelling tool, and that is the reason why this continuous feedback method is chosen. For systems, in which these processes occur on the same time scale, this approach cannot be applied.

1.4 Scope of the Research

Upon evaluation of the assigned task, the modelling of a Nakatsuji-type automotive converter, it was rather instantaneously apparent that the computational tools available were not sufficient to model these type of catalyst. The simulation software developed in our group (DETCHEM, see Chapter 2 and [22]) did not account for variations of the inlet gas composition and surface coverages. Since these variations are crucial for the functioning of the Nakatsuji-type catalyst, see Section 1.2.2, the software had to be expanded for the simulation of transient processes. Furthermore, it was foreseeable after preliminary simulations that the existing quasi-elementary-step reaction mechanism on rhodium was not sufficient to accurately describe the transient behaviour of this catalytic system.

Since it is impossible for the time being to address all these open questions with one computational approach, a multiscale modelling approach was chosen. This is legitimate, because the time scales of the processes are sufficiently diverse to assume the processes to be mainly decoupled. DFT calculations of transition metal surfaces were chosen to study surface processes and their dependencies. A detailed description of the processes on the surface of the catalytic component is vital for the prediction of the overall kinetics of heterogeneous reactions. The understanding of the kinetics of heterogeneous reactions is crucial for production and consumption of species in the catalytically active single channel. The

knowledge of production and consumption of species in the channel is in turn vital for the prediction of outlet gas compositions. Hence, surface processes exhibit a direct influence on the outlet gas composition. In our research group tools to model processes on different length as well as time scales are available. The combination of different approaches is a challenging task. The coupling of microkinetic simulation (DETCHEMS) to flow simulations (DETCHEM^{CHANNEL}) is already well established [21, 23]. So is the coupling of Monte-Carlo simulations to microkinetics [24]. The long-term goal is to combine the tools depicted in Figure 1.6 to model processes from nanometres to meters and from nanoseconds to hours.

The presented work focuses on the investigation of surface reactions and their dependencies on precoverage by means of DFT (Chapters 5 - 8). The influence of coverage dependent reaction parameters on surface overlayers calculated by microkinetic simulations will be discussed and a few examples of the impact of those parameters on transient conversions in catalytically active monoliths will be presented (Chapter 9).

The washcoat diffusion (DETCHEM^{WASHCOAT}) as well as heat balances (DETCHEM^{MONOLITH}) were neglected in the presented work. The resolution of 2-dimensional surface processes (DETCHEM^{MOCART}) and its coupling to simulation on other length and time scales is topic of doctoral thesis prepared parallel to this thesis [25].

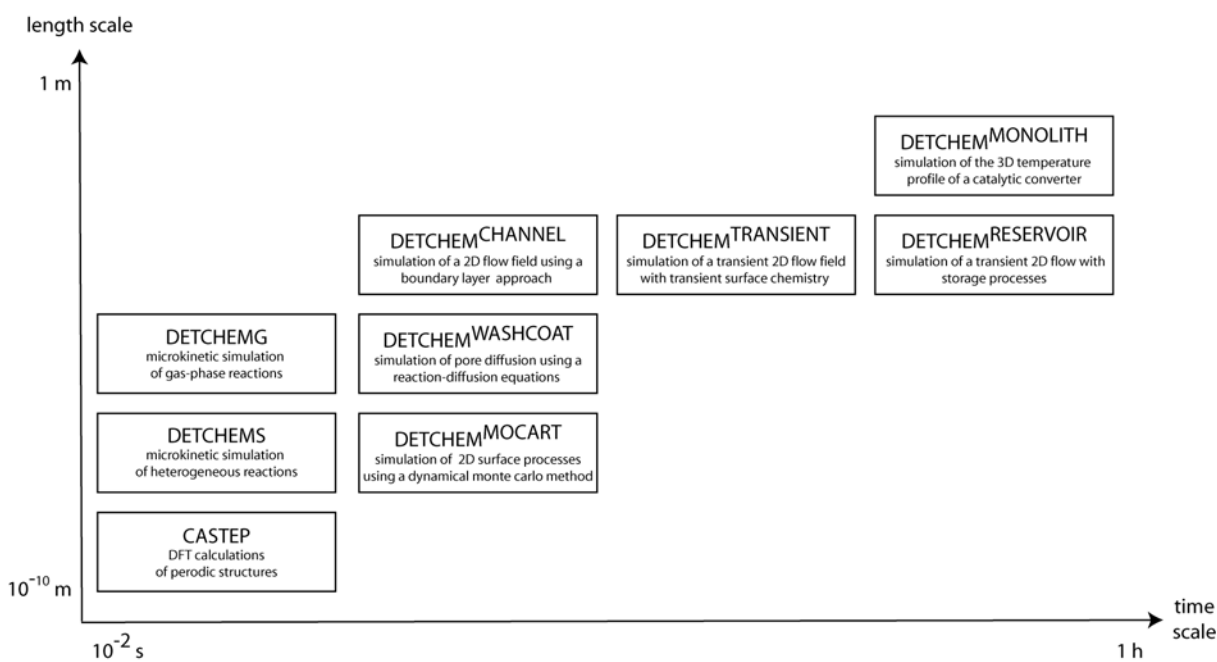


Figure 1.6: Length and time scales for modelling tools used in our research group

Chapter 2: Physical and Chemical Foundation

2.1 Quantum Mechanics

Quantum mechanics in simplistic terms is the study of matter and radiation at an atomic level. In the early 20th century scientists carried out experiments whose results could not be explained by classical physics (Newton's physics). However, it was recognised that classical physics is only inadequate for very fast (close to the speed of light) as well as for very small (atomistic level) systems, while it is accurate in most other cases. Deviations for very fast systems can be explained and brought into a coherent picture by Einstein's theory of relativity [26], while deviations for very small systems can be accounted for by quantum theory initiated by Planck [27].

Among the most important phenomena at small length scales that classical physics fail to describe while quantum mechanics succeeds, are the discreteness of energy, the wave-particle dualism of matter and light, Heisenberg's uncertainty principle, spin of a particle and quantum tunnelling.

For instance, the spectrum of light emitted by electronically excited atoms is composed of individual discrete lines, meaning that the emitted photons are of defined energies and not distributed over the complete spectrum. The photons of discrete energies emitted correspond to discrete electronic transitions in the energetic atom, and hence the electrons must be restricted to discrete energy levels. This restriction is referred to as quantisation of energy, which is eponymous for quantum mechanics.

Another effect that can be explained by the quantum theory, but cannot be explained by classical physics, is the dualism of matter and light proposed by the French physicist Louis de Broglie in 1923. Quantum mechanics can explain the observation that light behaves like a wave (diffraction, interference) as well as a particle (photoelectric effect). Light can indeed be

described as matter, while the probability density of a light particle behaves wave-like; that is the reason why light diffracted at an appropriate grid leads to bright/dark pattern when projected onto a screen (dark and bright = low and high probability density).

A unique quantum effect that will be investigated in this thesis is the magnetic moment of particles. An experiment by the German scientists Stern and Gerlach in the 1920s, the deflexion of an atomic beam in an inhomogeneous magnetic field, demonstrated that some particles have an intrinsic magnetic moment. This magnetic moment of particles is referred to as spin, which is a convenient expression for intrinsic angular momentum. The spin can only adopt certain discrete values, *i.e.*, is quantised. A graphic example for this quantisation would be that the angular momentum – the spin – of the particle can have two different directions, clock- and counter clockwise.

Electronic spin effects can for example be observed in electronic spectra of molecules with an odd number of electrons. A well-known application of spin is magnetic resonance imaging (MRI) applied in medical diagnostics, where the spin of a proton (the nucleus of a hydrogen atom) is utilised to determine the location of water. Since tumour tissue tends to exhibit a water concentration different from that of healthy tissue, tumours can be identified by means of MRI.

2.1.1 Schrödinger's Equation

As already mentioned, probability density of particles behaves wave-like. In the 1920 the Austrian physicist Erwin Schrödinger developed a differential equation which describes such a wave function [27],

$$i\hbar \frac{\partial}{\partial t} \psi(r,t) = -\frac{\hbar^2}{2m} \nabla^2 \psi(r,t) + V(r,t) \psi(r,t) \equiv \hat{H} \psi(r,t). \quad 2.1$$

By separating the variables, the time-independent version of Schrödinger's Equation 2.2 is obtained:

$$-\frac{\hbar^2}{2m} \nabla^2 \psi(r) + V(r) \psi(r) \equiv \hat{H} \psi(r) = E \psi(r). \quad 2.2$$

Hence, the wave function describing a particle and consequently the total energy can be calculated by solving the energy eigenvalue equation. Therefore, the energy of a system of electrons can in principle be determined by means of solving Schrödinger's equation.

A different approach to calculate the energy of a system of electrons was proposed by Hohenberg and Kohn in 1964 [28]. They proved that the ground-state energy is a functional of the overall ground-state electron density. Because this approach is used in the method applied in the presented work, it is explained in more detail in the subsequent paragraphs. Furthermore, it is addressed how these two approaches can be combined to achieve accurate, fast calculations. Prior to this, a crucial approximation for *ab-initio* calculations, the decoupling of nucleic and electronic motion, has to be introduced.

2.1.2 The Born-Oppenheimer Approximation

When considering molecules, the problem of calculating the energy of an interacting many electron system expands to calculating an interacting electron-nuclei system. Such a system has multiple degrees of freedom, and thus computations are much more complex, if not impossible.

An approximation introduced by Born and Oppenheimer in 1927 resolves this problem. The Born-Oppenheimer approximation assumes that, since nuclei are much heavier than electrons³, the electrons will adjust their position instantaneously to any nucleic movement [29]. Thus, nuclear and electronic motions are effectively decoupled. Hence, the nucleic positions can be computed by relaxing the electronic wave function corresponding to a trial nucleic conformation. Subsequently, the forces on the atomic core configuration resulting from these wavefunctions (electrons) are calculated, and the cores are adjusted classically according to the outer force. This is admissible since the masses of the nuclei are sufficiently large to be described classically. The Born-Oppenheimer approximation is a crucial prerequisite for many *ab-initio* quantum-mechanical computations.

³ The weight of an electron is only $5.4 \cdot 10^{-4}$ that of a proton.

2.1.3 Density Functional Theory (DFT)

The central assumption which underlies density functional theory, namely that the ground-state properties of a system are unique functionals of the ground-state electron density $\rho(r)$, was proven by Hohenberg and Kohn in 1964 [28]. According to this theorem, the ground-state energy of an electron system can be written as a functional of its electron density. However, the theorem of Kohn and Hohenberg provides only an existence proof, there is no prescription how to construct this functional. Therefore, efforts have been made to describe the Hohenberg-Kohn functional based on foundations that are partly rigorous and partly empirical. The electron density functional is built up from functionals for various contributions to the total energy (*e.g.*, kinetic, exchange or correlation energies).

2.1.4 Hohenberg-Kohn Theorem

Hohenberg and Kohn proved in their 1964 publication [28] that

- every observable of a stationary quantum-mechanical system can be calculated exactly from the ground-state electron density, *i.e.*, all observables can be written as functionals of the ground-state electron density (1st Hohenberg-Kohn theorem)

and

- the ground-state electron density can be calculated exactly using the variational method for minimisation of the Hohenberg-Kohn functional (2nd Hohenberg-Kohn theorem).

Assembling the Electron Density Functional – 1st Hohenberg-Kohn Theorem

Within the Born-Oppenheimer approximation the electronic wave functions (and thus the ground-state electron density) of a system of electrons solely depend on the actual position of the nuclei. The actual position of the nuclei determines the external potential \hat{V}_{ext} . Since the kinetic energy of the electrons \hat{T}_e as well as the electron-electron interaction \hat{U}_{ee} adjusts to the

external potential \hat{V}_{ext} originating from the nuclei, the external potential \hat{V}_{ext} is the only variable of the system.

Since the electronic Hamiltonian \hat{H}_{el} can be written as

$$\hat{H}_{\text{el}} = \hat{T}_{\text{e}} + \hat{V}_{\text{ext}} + \hat{U}_{\text{ee}}, \quad 2.3$$

the external potential \hat{V}_{ext} is the only degree of freedom. In the reverse, when the ground-state electron density $\rho(r)$ of a system is known, the coordinates and the type of nuclei can be calculated. Therefore, the exact ground-state electron density $\rho(r)$ of a system provides a consistent description of the system. Since the ground-state electron density $\rho(r)$ determines the number of electrons N according to the conservation relation

$$N = \int \rho(r) dr \quad 2.4$$

and is furthermore unique for a certain external potential \hat{V}_{ext} , the electron density contains the same information as the exact wave function Ψ that describes the electronic system. Kohn and Hohenberg proved this via a contradiction, see [28].

Minimising the Energy – 2nd Hohenberg-Kohn Theorem

The 2nd Hohenberg-Kohn theorem applies the variational method to determine the electron density. A trial electron density $\rho_{\text{t}}(r) \geq 0$ which is subject to the Conservation Equation 2.4 is assumed, and the trial energy $E[\rho_{\text{t}}]$ has to be equal or higher to the real ground-state energy E_0 according to the 2nd theorem.

The trial electron density can then be converged to the real ground-state energy E_0 using a constrained minimisation method such as the Lagrange method [30].

Kohn and Sham Method

Since it is not convenient to express the kinetic energy of a system by the electron density, Kohn and Sham proposed a method to combine the wave function approach with the electron density approach [31]. They repartitioned the total energy functional up into the following parts:

$$E[\rho] = T_e[\rho] + \int [V_{\text{ext}}[r] + U_{\text{cl}}[r]] \rho(r) dr + E_{\text{xc}}[\rho], \quad 2.5$$

where $T_e[\rho]$ denotes the kinetic energy of the electrons without any electron-electron interaction, U_{cl} accounts for the classical Coulomb interaction between the electrons and \hat{V}_{ext} for the potential from the nuclei. Expressions of the kinetic energy of the electrons as functionals of the electron density $T_e[\rho]$ are not very accurate, but can easily be calculated from the electronic wavefunction. The last functional $E_{\text{xc}}[\rho]$ includes all energy contributions that have not been taken into account by the previous terms, *i.e.*, electron exchange, electron correlation, and is therefore called exchange-correlation functional.

This system can be described as a linear combination of single-particle wave functions, the so-called Kohn-Sham orbitals $\psi_i^{\text{KS}}(r)$ and the electron density $\rho(r)$ can be expressed as the sum of these Kohn-Sham orbitals according to

$$\rho(r) = \sum_i |\psi_i^{\text{KS}}(r)|^2. \quad 2.6$$

The kinetic energy $T_e[\rho]$ can then be calculated from the wave functions

$$T_e[\rho] = \sum_i -\frac{\hbar^2}{2m_e} \int \psi_i^* \nabla^2 \psi_i d^3r, \quad 2.7$$

while the remaining parts of the total energy functional are expressed in terms of the electron density. A brief description of how these functionals are approximated is given in the subsequent paragraph.

Approximations for the Exchange-Correlation Functional

The first suggestion for the exchange-correlation functional is based on the exchange-correlation energy $\epsilon_{xc}(\rho(r))$ of a homogeneous electron gas with the electron density $\rho(r)$. The functional is described as

$$E_{xc}^{\text{LDA}}[\rho(r)] = \int \epsilon_{xc}(\rho(r))\rho(r)dr, \quad 2.8$$

in which the exchange-correlation energy $\epsilon_{xc}(\rho(r))$ solely depends on the local electron density (local density approximation – LDA) [32]. However, when describing molecular systems, the exchange-correlation energy $\epsilon_{xc}(\rho(r))$ is not exclusively determined by the local density, but also influenced by the gradient of the electron density (*e.g.*, in chemical bonds). The most successful sophistication of the LDA approach therefore is the generalised gradient approximation (GGA) [33]. Here, the functional depends on the local electron density as well as on its first derivative,

$$E_{xc}^{\text{GGA}}[\rho(r)] = \int f(\rho(r), \nabla\rho(r))d^3r. \quad 2.9$$

Since there is no real physical system to which $f(\rho, \nabla\rho)$ can be fitted, a vast amount of GGA functionals have been proposed. A functional that has been very successful in predicting especially chemical surface processes [34–38] was proposed by Perdew and Wang in 1992 [33] and was therefore chosen for this study of rhodium surface chemistry.

2.1.5 Implementation of DFT – The CASTEP Code

In this thesis DFT is applied as implemented in CASTEP (Cambridge Sequential Total Energy Package) developed by Payne and co-workers [39]. CASTEP is based on a supercell approach, *i.e.*, structures to be calculated have to be periodic in 3 dimensions. This approach is especially advantageous when considering surface structures, because upon expansion from

a small metal cluster or metal slab into 3 dimensions a real solid surface is built (see Figure 2.1).

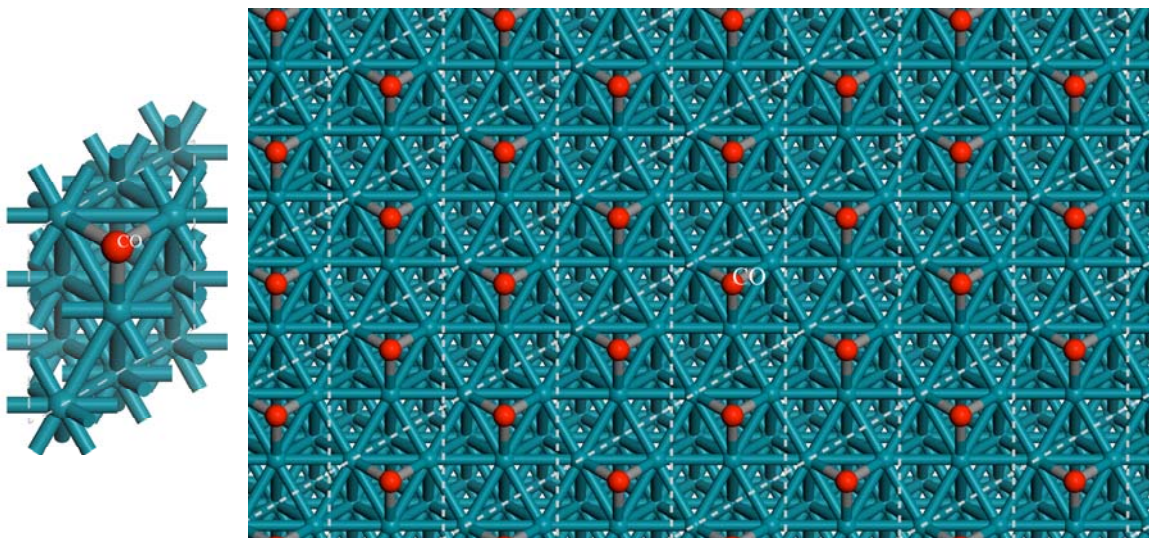


Figure 2.1: Elementary cell and expansion

The electron-core interaction is described by ultrasoft pseudopotentials proposed by Vanderbilt (see Section 2.1.7), while electronic wave functions are represented by a sum of plane waves. For electron density minimisation CASTEP applies a self-consistent field scheme. The most popular approximations for the exchange-correlation energy, *i.e.*, LDA and GGA with several different functionals, are implemented. CASTEP's foundations are briefly explained in the subsequent paragraphs.

2.1.6 Bloch Theorem and Plane Waves

Systems that are periodic in three dimensions have additional symmetry, namely the symmetry of periodicity. This symmetry imposes a constraint on the charge density of the system, *i.e.*, the charge density must be constant under translation by the lattice vector G in reciprocal space according to

$$|\Psi(r)|^2 = |\Psi(r + G)|^2. \quad 2.10$$

This is the basis for the application of Bloch's theorem which states that in every 3-dimensional periodic system an electronic wave function can be written as a product of a part representing the periodicity u as well as a plane wave function $e^{ik \cdot r}$ with a wave vector k ,

$$\psi_i(r) = u_i(r) e^{ik \cdot r}. \quad 2.11$$

The periodic function can again be expressed by a set of plane waves

$$u_i(r) = \sum_G c_{i,G} e^{iG \cdot r}, \quad 2.12$$

leading to an expression for the wave function such as

$$\psi_i(r) = \sum_G c_{i,k+G} e^{i(k+G) \cdot r}. \quad 2.13$$

Bloch's theorem reduces the problem of calculating an infinite number of plane waves to calculating a finite number of plane waves but still over the complete Brillouin zone characterised by the wave vector k .

Since in a periodic structure there is an infinite number of electrons n and hence an infinite number of vectors k , there is an infinite number of solutions for $\psi_{n,k}$. The system can be simplified by assuming that the difference of $\psi_{n,k}$ is negligible for k -points that are close to each other. Therefore only a finite number of k -points is calculated (see Section 2.1.8); this simplification is called k -point sampling. In fact, for each k -point still an infinite number of plane waves are necessary for complete description. However, the coefficients of plane waves with small kinetic energies affect the total energy of the system more than those of plane waves with large kinetic energies. Therefore, the plane wave basis set can be truncated at a certain kinetic energy leading to a finite set of plane waves for finite k -points as an approximation.

The major drawback of the plane wave approach is that the number of plane waves necessary for accurate description is determined by the curvature of the wave function. All

electronic wave functions vary rapidly in core-close regions, and therefore they have strong curvatures that demand large basis sets. This disadvantage can elegantly be overcome by replacing the cores as well as the core electrons by pseudopotentials with a fixed effective potential (see Section 2.1.7).

2.1.7 Pseudopotentials

The pseudopotential is a fictitious potential that is constructed from the nucleus and the core electrons. The nuclear potential is singular and the electronic potential energy decreases proportional to the atomic radius. Owing to the high nuclear potential in the centre of the atom the curvatures of electrons in this regions are large.

As mentioned in the foregoing section, strongly curved wave functions require large plane wave basis sets. Hence the representation of electrons in core-close regions is Gordian. Moreover, since chemical effects are considered here, only valence electrons are of importance. Therefore, a sustainable simplification for these systems is to replace the core potential as well as the electronic potential of the tightly bound electrons with a softer and finite pseudopotential. The pseudopotentials are the result of the combination of the core and the electronic wavefunctions of the core electrons and are therefore softer and spatially finite. This potential of course alters the behaviour of the wavefunction, but this effect can be met by matching the newly generated Coulomb potential to the old Coulomb potential beyond a certain pseudopotential radius r .

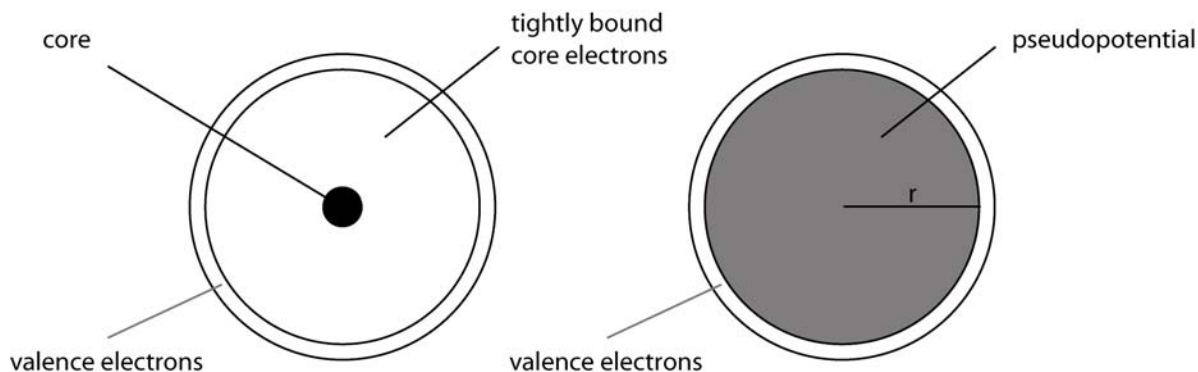


Figure 2.2: Pseudopotentials

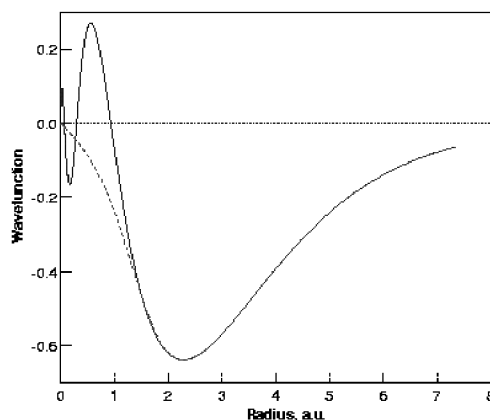


Figure 2.3: The 4s (full) and the pseudo-(dashed) radial wavefunction as function of the Bohr radius of the Nickel atom

Thus, only the (for chemical processes negligible) wavefunctions within the radius r will be affected by the pseudopotential, and the (for chemical processes important) wavefunctions beyond the radius r will stay correct (Figure 2.3), and the number of electronic bands to be calculated has been effectively reduced.

2.1.8 Brillouin-Zone Sampling

Bloch's theorem reduces the necessity of calculating an infinite number of wave functions at an infinite number of k -points to calculating a finite number of wave functions still at an infinite number of k -points. Since the occupied states at every k -point contribute to the electronic potential, in principle, still an infinite number of calculations are necessary. Assuming that the wave functions at k -points close to each other will be identical, the problem can be reduced to an integration over a small number of k -points in the Brillouin zone. The number of k -points necessary to calculate the total energy accurately depends on the system studied. In this study transition metals are examined, and these require a rather dense grid of k -points. There are several methods to generate a grid of k -points such as the Chadi-Cohen and the Gilat-Raubenheimer method. In this study the scheme proposed by Monkhorst and Pack is utilised [40].

The Monkhorst-Pack Scheme

The Monkhorst-Pack scheme generates a uniform grid of k -points in the 3 dimensions of the reciprocal space. The number of k -points along each coordinate is determined by three integer values q_i (i denotes the coordinate). These integers generate a set of numbers according to

$$u_i = \frac{2r_i - q_i - 1}{2q_i} \quad 2.14$$

with r_i varying from 1 to q_i and i denoting the coordinates in reciprocal space x, y, z . The Monkhorst-Pack scheme then generates an equidistant grid with k -points as given by

$$k_{xyz} = u_x b_1 + u_y b_2 + u_z b_3, \quad 2.15$$

where b_i denotes the lattice vectors in reciprocal space. This leads to $\prod q_i$ distinct points in the Brillouin zone. To illustrate this method, the k -points of a two-dimensional Brillouin zone were calculated according to the Monkhorst-Pack scheme with $q_1 = 5$ and $q_2 = 8$. The rectangle in Figure 2.4 represents the 2-dimensional Brillouin zone, and dots represent the k -points as generated by the Monkhorst-Pack scheme. If the Brillouin zone is point-symmetric in the coordinate origin, only the k -points represented by red dots have to be calculated to determine the Brillouin zone. Therefore, applying further symmetry to the periodic structures leads to a significant speed-up of the Brillouin zone integration and hence shortens the time for all energetic calculations.

The combination of the plane wave approach (Section 2.1.6), pseudopotentials (Section 2.1.7) and k -point sampling (Section 2.1.8) leads to time efficient and accurate computations.

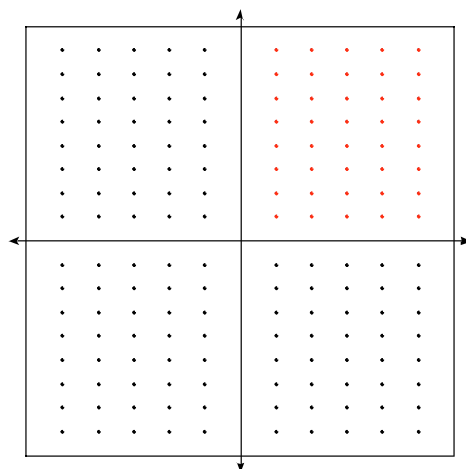


Figure 2.4: Sampling of a 2-dimensional Brillouin zone by applying the MP scheme [41]

2.1.9 Structural Optimisations with CASTEP

Geometry Optimisation

To refine the geometry of a structure in order to obtain the local energy minimum, the most stable local arrangement, CASTEP optimises the energy of a system in an iterative process. It varies atomic coordinates as well as cell parameters until a structure is reached in which the magnitude of stresses and forces is smaller than a defined convergence tolerance. In other words, until a minimum energy conformation is reached and the accuracy of the method is given by the convergence tolerance. Milman *et al.* have shown that structures calculated with CASTEP closely resemble the real structures [42]. This thesis gives further prove of the reliability of the CASTEP geometry optimisation tool, particularly with regard to chemical surface processes (see Chapter 4).

Calculation of Adsorption Energies

To determine the adsorption energies, $\Delta E_{\text{adsorption}}$, the target surface was geometry-optimised with the adsorbant added on the one hand and without the adsorbant molecule on the other hand; the energies of the optimised surfaces were calculated subsequent to the geometry optimisation. The geometry of the adsorbant molecule was optimised within a cell similar to

the cell of the surface, and the energy of this optimised system $E_{\text{adsorbant}}$ was calculated subsequently. Finally the adsorption energies were calculated according to

$$\Delta E_{\text{adsorption}} = E_{\text{surface+adsorbant}} - (E_{\text{surface}} + E_{\text{adsorbant}}). \quad 2.16$$

Transition-State Location

The optimisation processes discussed up to now were concerned with converging the energy of a system to a minimum. A transition state is in contrast an energy maximum in direction of the reaction coordinate, but still an energy minimum in all other directions. The activated complex is located at the saddle point of the minimum energy pathway between reactants and products on the potential energy surface.

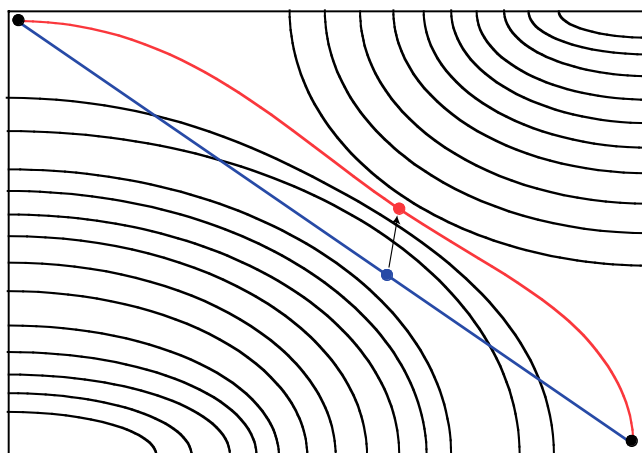


Figure 2.5: Contour plot of the potential energy surface (PES) of a surface reaction⁴, black lines mark areas of constant energy, blue line illustrates a first linear approximation of the reaction trajectory, while the red line stands for the optimised trajectory

⁴ level curves denote equal energies rising from the centre to the borders.

CASTEP utilises a linear transit method combined with a conjugate gradient method to localise the transition state of a reaction. This optimisation method has been used here to determine the energy barriers for surface processes such as decompositions or diffusion.

This numerical procedure starts with a linear interpolation between the geometry optimised structures for reactants and products (Figure 2.5, blue line). The energy maximum of this linear interpolations is a first approximation of the transition state (Figure 2.5, blue dot). A further refinement of this approximated transition state is performed via a conjugate gradient (CG) method. CG methods are widely used in optimisation algorithms. The method makes intelligent use of the gradient information and curvature on the potential energy surface (PES) starting from the approximated transition state (Figure 2.5, black arrow). The CG refinement is applied repeatedly until convergence to a certain tolerance factor, which can be set by the user. This ensures a sound estimation of the saddle point of the minimum energy pathway on the PES is located (Figure 2.5, red dot), and hence a proper approximation of the real reaction trajectory (Figure 2.5, red line) is determined. For a more detailed discussion of this method see [43]. From the energies obtained during the PES calculations, the heats of reaction were calculated according to

$$\Delta E_{\text{reaction}} = E_{\text{products}} - E_{\text{reactants}} \quad 2.17$$

and the activation energy according to

$$E_{\text{a}} = E_{\text{transition state}} - E_{\text{reactants}} \quad 2.18$$

Calculation of Magnetic Moment

For many systems investigated in this thesis, magnetic effects could play a role and have therefore to be taken into account for the accurate calculation of the total energy. The magnetic moment of a molecule originates from an intrinsic magnetic moment associated with the angular momentum of electrons (electron spin). Electronic spin can exhibit two different orientations $+1/2$ and $-1/2$, which are designated as α and β . As described by Pauli's exclusion principle, electrons occupying the same state (the same orbital), have to have different spins. Therefore, the overall spin of a fully occupied molecular orbital is zero, since

the two orientations cancel out each other. As soon as unpaired electrons are present in a molecule (as *e.g.*, in radicals or odd-electron molecules), the overall spin is differs from zero. In order to calculate the magnetic moment in terms of spin density, charge densities for both electronic orientations ($\rho_\alpha(r), \rho_\beta(r)$) are calculated using a spin-restricted version of the GGA functional (GGSA). From these charge densities for different electron polarisations, the spin density is calculated according to

$$\rho_{\text{spin}}(r) = \rho_\alpha(r) - \rho_\beta(r). \quad 2.19$$

The total electron density of the supercell is calculated according to

$$\rho_{\text{spin}}^{\text{total}} = \int \rho_{\text{spin}}(r) dr. \quad 2.20$$

Furthermore, the local electron density is calculated according to

$$\rho_{\text{spin}}^{\text{local}} = \int |\rho_{\text{spin}}(r)| dr. \quad 2.21$$

The local electron spin density is a measure of the spin polarisation inside a certain system. To assume that a system is non-spin-polarised, both the local and the total spin densities have to be zero.

2.2 Reactive Flows

Time and length scales of the surfaces processes considered by *ab-initio* quantum-mechanical simulations (Section 2.1) are considerably smaller than the time and length scales of microkinetic and flow simulations. Hence, these processes can be regarded as effectively decoupled. Therefore, the multiscale modelling approach explained in Chapter 1 can be applied and the results obtained from DFT calculation can be used as input parameters for the simulation of reactive flows. However, idealisations of the DFT studies have to be taken into account.

Transferring DFT Results – Materials, Pressure and Temperature Gap

When transferring results from DFT calculations to simulations of more realistic systems, it has to be considered that the DFT calculations are carried out for absolutely perfect single crystal surfaces, which are not present on any real single crystal and least of all on catalyst particles. This discrepancy is referred to as materials gap. Moreover, only temperature independent processes such as activation energies – which are with few exceptions temperature independent – can be studied by means of DFT, since the general density functional theory is restricted to 0 Kelvin. Therefore, DFT results are even further apart from realistic models than classical surface science studies on single crystals which contain only few defects. Moreover, classical surface science studies suffer from the drawback that they are conducted under high-vacuum conditions at low temperature, while much higher pressures and temperatures are applicable in realistic catalytic systems.

However, the pressure and temperature gap can be closed by recently developed *in-situ* experimental techniques, such as optical sum-frequency generation (SFG) vibrational spectroscopy [44]. This technique has been successfully applied to study surface coverages at high pressures and elevated temperatures [45, 46]. Using such a high-pressure, high-temperature spectroscopic technique, findings of DFT calculations and classical surface science studies can be linked to realistic processes on catalytically active surfaces.

2.2.1 Microkinetic Simulations

Chemical Reactions

A chemical reaction is an inter- or intramolecular rebonding process. In a chemical reaction species can be rearranged, consumed or added to a different species. The mass as well as the number and type of atoms stays constant during the reaction, only the bonding between the atoms changes. A mathematical description of a chemical reaction can be written as



where A_i denotes the species, while ν_i are the stoichiometric coefficients. In case of fast reactions, the Gibbs energy determines the behaviour of a chemical system, in case of slow reactions the kinetics controls it (thermodynamic versus kinetic control). For thermodynamically controlled reactions the scenario is double tracked: If the difference in Gibbs energy $\Delta G_{\text{reaction}}$ of such a thermodynamically controlled forward reaction-reverse reaction system is small, an equilibrium composition is reached. For systems with a large difference in Gibbs Energy $\Delta G_{\text{reaction}}$ the reaction is one way, meaning the energetically more favoured compound is formed while the other is consumed. The speed of a reaction and the composition of a chemical equilibrium depend on the boundary conditions, see following paragraph.

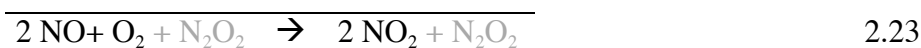
According to collision theory, the rate of a certain reaction is temperature- as well as concentration dependent, because the probability of reaction depends on the number as well as on the energy of collision [47, 48]. A change in concentration leads to a different probability of collision. A change in temperature will also lead to a different probability and moreover to a different energy of collision. Both affect the probability of reaction, because not only a collision but also a collision with a minimal energy, the so-called activation energy E_a , is premised for successful reaction.

Global and Elementary Reactions

Elementary reactions are reactions whose reaction schemes equal the stoichiometry of the concerted process on molecular scale, in contrast to overall or global reactions, where the equation does not describe the process on a molecular level. For example, the global reaction of the oxidation of nitrogen oxide with oxygen is given in Equation 2.23,



The Reaction Equation 2.23 only describes the reactants and the products of a reaction, but does not give information about the reaction pathway. If more detailed information concerning the reaction pathway is required, the global reaction has to be replaced by an elementary-step reaction mechanism such as given by Reaction Equations 2.24 - 2.25.



Adding up reactants and products of all elementary steps (Eq. 2.24 – Eq. 2.25) and subtracting the intermediate leads to the global Reaction Equation 2.23. Global reactions can have non-integer or even negative reaction order⁵ and hence kinetic expressions are complex. However, for elementary-step reactions the reaction order is equivalent to the molecularity of the reaction, and thus the time expression for the first step of the example reaction (Eq. 2.24) can be written as

$$\frac{dc_{\text{NO}}}{dt} = -k_1 c_{\text{NO}}^2 \quad 2.26$$

⁵ The reaction order is the sum of the exponents of the kinetic expression of a reaction (e.g. 2 in Equation 2.26).

A common model for the reaction rate coefficient k_f is the modified Arrhenius expression, which is a function of the temperature T , the pre-exponential factor A , the temperature exponent β as well as the activation energy E_a . The Arrhenius parameters E_a and A are referred to as kinetic data later in this thesis,

$$k_f = AT^\beta \exp\left[\frac{-E_a}{RT}\right]. \quad 2.27$$

The calculated reaction rate coefficient k_f for a species i at a certain temperature can then be used to calculate the rate law for the species,

$$\frac{dc_i}{dt} = v_i k_f \prod_{i=1}^{N_G} c_i^{v_i^n}. \quad 2.28$$

Reactions on Transition Metal Surfaces

In case of reactions on transition metal surfaces the concentrations in Equation 2.28 are given in terms of a surface concentration or coverage θ_i according to

$$\theta_i = \frac{\sigma_i}{\sum_{j=0}^n \sigma_j}, \quad 2.29$$

where σ_i denotes the number of surface sites occupied by species i (with $i = 0$ for unoccupied sites), and n the number of surface species. Since surfaces can exhibit different facets and contain inhomogenities such as defects, steps and kinks, not all adsorption sites are chemically equivalent, and hence approximations have to be made. The approximation applied in the presented work is the mean-field approximation. In the mean-field approximation it is assumed that the adsorbates are randomly distributed over a uniform surface. Uniform surface means that all adsorption sites are treated as an average over the real existing adsorption sites weighted by their proportion. On highly define surface such as for example the (111) facet, the mean field approximation can conveniently be applied, because the surface only one possible adsorption site exists.

Kinetic parameters for surface reactions measured on polycrystalline foil can hence be taken readily, since they are already averaged over all the different facets and defects included in the foil. Kinetic parameters measured on defined surfaces (*e.g.*, (111), (110) and (100)) have to be averaged before they can be used in microkinetic calculations based on the mean-field approximation.

The composition of the surface overlayer (the distribution and composition of adsorbants) can have severe influence onto the surface reaction, as will be pointed out later in this thesis. For those cases, an extended version of the Arrhenius expression

$$k_f = AT^\beta \cdot \exp\left[\frac{-E_a}{RT}\right] \cdot g_f(\theta_i) \quad 2.30$$

with a correction factor g_f

$$g_f(\theta_i) = \prod_{i=0}^n \theta_i^{\mu_i} \exp\left(\frac{\varepsilon_i \theta_i}{RT}\right) \quad 2.31$$

for every elementary-step reaction is applied. The coverage dependence of the reaction rate coefficient is included via two terms. The term μ_i describes the shift in reaction order, while ε_i describes the variance of the activation energy of a certain reaction. A shift in reaction order is not that likely, especially not for the processes discussed in this thesis. However, variances of the activation energies will be addressed later in this thesis, because these can be crucial for the understanding of global processes in automotive emission control.

Not only surface reactions but also adsorption processes depend on the surface coverage as well as on the chemical nature of the surface adsorbants. Adsorptions are also chemical reactions since they include a rearrangement of bonding (*e.g.*, coordination of the free electron pair to the surface upon CO adsorption). For those processes, it is more convenient to express the reaction rate k^{ads} as a function of adsorption probability (sticking coefficient) according to

$$k^{\text{ads}} = \frac{S_i^0}{\Gamma_i^{\text{r}}} \sqrt{\frac{RT}{2\pi M_i}}. \quad 2.32$$

S_i^0 denotes the initial sticking coefficient (the probability of being adsorbed when colliding with a uncovered surface), Γ_i^{r} the surface site density of species i .

Production rates \dot{s}_i of a surface or gas-phase species i by a surface process (either ad- or desorption or surface reaction) can then be calculated according to

$$\dot{s}_i = \sum_{k=1}^{K_s} \nu_{ik} k_{f_k} \prod_{i=1}^{N_G + N_s} c_i^{\nu_{ik}}, \quad 2.33$$

where K_s denotes the number of surface processes.

Transient Surface Chemistry

The surface processes investigated in this thesis do not reach a steady-state, see Chapter 1. Therefore, not only the surface coverage, but also the variation of the surface composition with time is of interest here. Based on Equations 2.29, 2.33 and the definition of the surface site density (Eq. 2.34),

$$\Gamma = \frac{\sigma}{A}, \quad 2.34$$

the time-dependent variation of each surface coverage of a species i can be calculated from these production rates according to the differential equation,

$$\frac{d\theta_i}{dt} = \frac{\dot{s}_i \sigma_i}{\Gamma}. \quad 2.35$$

Herewith, the surface coverages θ_i can be updated by integrating Eq. 2.35. A conservation relation for the solutions of Eq. 2.35 is

$$\sum_{i=1}^{N_s} \theta_i(t) = 1 \quad 2.36$$

for any given t .

2.2.2 Simulation of the Flow in Monolithic Reactors

Automotive catalysts are monolithic reactors with numerous passageways (see Figure 2.6, left) in which the catalytic active component is dispersed in a support material such as an oxidic washcoat or a zeolitic structure [49]. Dispersing metal particles in a support material, *e.g.*, alumina, has advantages such as a high surface-to-volume ratio and a high surface-to-weight ratio of the metal component. This high surface-to-weight ratio of the metal maximises the active surface, hence minimises the amount of expensive precious metal spread in the catalyst and herewith optimises the costs of the catalyst. The support material deposits preferably in the corners of the monolithic channels (see Figure 2.6, right), and thus they exhibit an almost rod-like geometry.

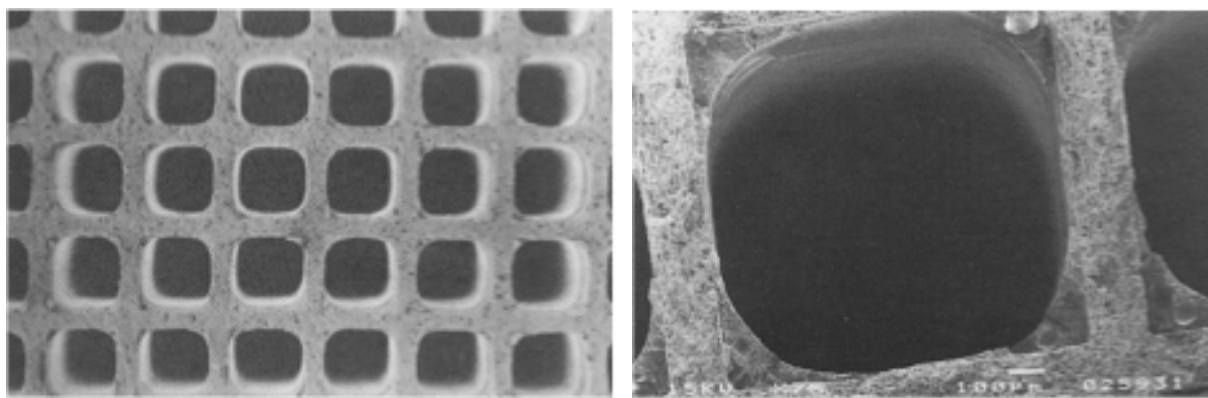


Figure 2.6: Catalytic monolith [50] and a TEM (transition electron microscopy) enlargement of a single channel coated with alumina washcoat [51].

Therefore, a common assumption made for modelling is that the monolithic channels as well as the distribution of the flow field are perfectly cylindrical. Since the diameter of these monolithic channels is in the range of a millimetre and the Reynold's number of the flow inside is beneath 2000 ($Re < 2000$). Owing to the mainly⁶ laminar flow field inside a tubular surrounding, the two-dimensional axi-symmetric Navier-Stokes equations can be utilised to

⁶ at the channel entrance the flow field might be locally turbulent

describe the fluid dynamics. A general introduction of how to describe fluid dynamics mathematically is given in the subsequent sections.

Fluid Dynamics

Fluid dynamics of a defined amount of matter is described by a set of coupled differential equations. This set consist of a partial differential equation for each extensive property of the given matter (energy, mass and momentum). Alternatively, the dynamics of fluids can be described by considering the flow within a defined volume, the so-called control-volume approach. The advantage of this approach is that upon transforming the governing equations into the control-volume form, the fundamental values are intensive properties (such as density or velocity). Intensive properties are – in contrast to extensive properties – conveniently accessible by standard laboratory measurements. Comparison of simulation results to these measurements is fruitful in terms of model verification.

In case of reacting fluids the mathematical description is subject to further constraints, namely the species mass conservation and the conservation of enthalpy, as will be explained in more detail later in this section. As already mentioned, the flow field in automotive catalytic converters is laminar and the flow geometry can be assumed rod-like. Therefore, the following paragraphs will focus on fluid dynamics of two-dimensional flows inside tubular geometries, and the interested reader is referred to textbooks on fluid dynamics for a more detailed description [52-56].

Tubular Flow Fields

Owing to the axisymmetry of tubes and the laminar flow field of the flows discussed in this work, the flow field inside the tubular reactor can as well be regarded axisymmetric. Therefore, simplifications to the governing equations mentioned earlier in this section can be made. Two approaches, the stationary 2D Navier-Stokes equations [52] and the boundary layer approximation [57] to those equations, will be explained.

Two-Dimensional Axisymmetric Navier-Stokes Equations

The stationary 2-dimensional Navier-Stokes equations (Eqs. 2.37- 2.42) describe an axisymmetric flow in two dimensions and are simplified versions of the general governing

equations mentioned earlier (for details see [21, 23]). The independent variables are given in cylindrical coordinates, z denotes the axial position while r denotes the radial position. Fluid velocities are given separately for both coordinates directions; u as the axial velocity and v as the radial velocity.

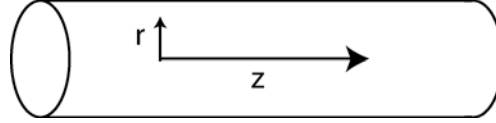


Figure 2.7: Cylindrical coordinates r for radial position and z for axial position

Effects from gravity are not included in these equations, as they do not affect the behaviour of the catalytic systems investigated in this thesis.

Apart from assuming perfect-gas behaviour, the stationary 2D Navier-Stokes equations (Eqs. 2.37- 2.42) for laminar reacting multi-component systems have few assumptions. In this interacting nonlinear elliptical set of partial differential equations, species may not only travel downstream, but also upstream via diffusion. For this type of equation system the numerical solution CPU time-consuming:

Mass continuity

$$\frac{\partial(\rho u)}{\partial z} + \frac{1}{r} \frac{\partial(r \rho v)}{\partial r} = 0 \quad 2.37$$

Axial momentum

$$\rho u \frac{\partial u}{\partial z} + \rho v \frac{\partial u}{\partial r} = -\frac{\partial p}{\partial z} + \frac{\partial}{\partial z} \left(2\mu \frac{\partial u}{\partial z} - \frac{2}{3} u \nabla \cdot \mathbf{V} \right) + \frac{1}{r} \frac{\partial}{\partial r} \left(\mu r \left(\frac{\partial v}{\partial z} + \frac{\partial u}{\partial r} \right) \right) \quad 2.38$$

$$\text{with } \nabla \cdot \mathbf{V} = \frac{1}{r} \frac{\partial(r \rho v)}{\partial r} + \frac{\partial u}{\partial z}$$

Radial momentum

$$\rho u \frac{\partial v}{\partial z} + \rho v \frac{\partial v}{\partial r} = -\frac{\partial p}{\partial r} + \frac{\partial}{\partial r} \left(\mu \left(\frac{\partial v}{\partial z} - \frac{\partial u}{\partial r} \right) \right) + \frac{\partial}{\partial r} \left(\left(2\mu \frac{\partial v}{\partial r} - \frac{2}{3} \mu \nabla \cdot \mathbf{V} \right) \right) + \frac{2\mu}{r} \left(\frac{\partial v}{\partial r} - \frac{v}{r} \right) \quad 2.39$$

Species continuity

$$\rho u \frac{\partial Y_i}{\partial z} + \rho v \frac{\partial Y_i}{\partial r} = -\frac{\partial j_{i,z}}{\partial z} - \frac{1}{r} \frac{\partial (r j_{i,r})}{\partial r} \quad (i = 1, \dots, N_G) \quad 2.40$$

Enthalpy

$$\begin{aligned} \rho u \frac{\partial h}{\partial z} + \rho v \frac{\partial h}{\partial r} = & \frac{\partial}{\partial z} \left(\lambda \frac{\partial T}{\partial z} \right) + \frac{1}{r} \frac{\partial}{\partial r} \left(r \lambda \frac{\partial T}{\partial r} \right) + u \frac{\partial p}{\partial z} + v \frac{\partial p}{\partial r} \\ & - \sum_{i=1}^{N_G} \left(\frac{\partial (h_i j_{i,z})}{\partial z} + \frac{1}{r} \frac{\partial (r h_i j_{i,r})}{\partial r} \right) \end{aligned} \quad 2.41$$

Equation of state

$$p = \frac{\rho RT}{M} \quad 2.42$$

Boundary Layer Approximation to the 2D Navier-Stokes Equations

An approximation to the Navier-Stokes equations was made by Prandtl [57]. He suggested that as the Reynolds numbers (the ratio of inertial forces to viscous forces) of a current increase, *i.e.*, at high velocities, the axial diffusion is negligible in comparison to the convective transport. Therefore, the Equation 2.45 for the radial momentum states that the pressure is constrained with regard to r . Hence, the second order derivatives with respect to z in the Navier-Stokes equation system are eliminated, and they convert to the equation system (Eqs. 2.43-2.47).

Mass continuity

$$\frac{\partial \rho u}{\partial z} + \frac{1}{r} \frac{\partial (r \rho v)}{\partial r} = 0 \quad 2.43$$

Axial momentum

$$\rho u \frac{\partial u}{\partial z} + \rho v \frac{\partial u}{\partial r} = -\frac{\partial p}{\partial z} + \frac{1}{r} \frac{\partial}{\partial r} \left(\mu r \frac{\partial u}{\partial r} \right) \quad 2.44$$

Radial momentum

$$\frac{\partial p}{\partial r} = 0 \quad 2.45$$

Species continuity

$$\rho u \frac{\partial Y_i}{\partial z} + \rho v \frac{\partial Y_i}{\partial r} = -\frac{1}{r} \frac{\partial (r j_{i,r})}{\partial r} \quad (i = 1, \dots, N_G) \quad 2.46$$

Enthalpy

$$\rho u \frac{\partial h}{\partial z} + \rho v \frac{\partial h}{\partial r} = \frac{1}{r} \frac{\partial}{\partial r} \left(r \lambda \frac{\partial T}{\partial r} \right) + u \frac{\partial p}{\partial z} - \sum_{i=1}^{N_G} \frac{1}{r} \frac{\partial (r h_i j_{i,r})}{\partial r} \quad 2.47$$

The resulting equation system (Eqs. 2.43-2.47) is parabolic; this is mathematically a significant simplification compared to the elliptic Navier-Stokes equation system (Eqs. 2.37-2.42). Species can only travel downstream and hence the axial coordinate is time-like. Hence, the boundary layer approximation is only valid as long as the flow is laminar.

Simulation of Transient Fluid Dynamics

In the catalytic aftertreatment systems inlet gas composition varies on time scales in the order of seconds. The residence time of molecules inside the channel lies on times scales in the order of 10 ms. As discussed in Chapter 1, different time scales permit to treat the processes as independent, because changes of the inlet conditions occurs only very rarely in time scales of the fluid dynamics. The flow field can be considered steady state during the calculation time step of the flow field. Therefore, the stationary BL approach can be also utilised for calculating time-dependent flow processes, see 2.2.4 Implementation.

2.2.3 Coupling of Microkinetic Simulations to CFD

Balance equations at the interface of gas phase and surface are used to couple microkinetic simulations of heterogeneous reactions to a gas flow field. The mass fraction Y_i of a certain species i is determined by the mass balances of the gas-phase species N_G , including their diffusive \vec{j}_i and convective \vec{v}_{Stefan} mass transport in either direction at the interface.

Furthermore, the production/consumption of species by heterogeneous surface reactions (R_i^{het}) is included, giving finally

$$\int \rho \frac{\partial Y_i}{\partial t} dV_{\text{gas}} = - \int (\vec{j}_i + \rho \vec{v}_{\text{Stefan}} Y_i) \vec{n} dA + \int R_i^{\text{het}} dA \quad (i = 1, \dots, N_G). \quad 2.48$$

V_{gas} is the gas-phase control volume above the surface unit A with the heights of the absolute value of vector $|\vec{n}|$, which is normal to the surface vectors of A . Consumption/production of a species i is given as R_i^{het} which is a function of the reaction rate \dot{s}_i (Eq. 2.49).

$$R_i^{\text{het}} = \dot{s}_i M_i \frac{A_{\text{cat}}}{A_{\text{geom}}}. \quad 2.49$$

At steady-state conditions the control volume dV_{gas} can be reduced to 0 and by insertion of Eq. 2.49, Eq. 2.48 converts to the boundary condition at the gas-surface interface:

$$\bar{n}(\bar{j}_i + \rho \bar{v}_{\text{Stefan}} Y_i) = \dot{s}_i M_i \frac{A_{\text{cat}}}{A_{\text{geom}}} \quad (i = 1, \dots, N_G) \quad 2.50$$

The Stefan velocity is a measure for the mass flux at the solid-gas phase interface. For steady-state processes, the Stefan velocity \bar{v}_{Stefan} vanishes. In case of transient processes, the Stefan velocity \bar{v}_{Stefan} can reach considerable values,

$$\bar{n} \bar{v}_{\text{Stefan}} = \frac{1}{\rho} \sum_{i=1}^{N_G} R_i^{\text{het}}. \quad 2.51$$

The rate of overall reaction also depends on the size of catalytically active surface to which the gas is exposed. This dependence is accounted for by the ratio between catalytically active surface (A_{cat}) and surface area of the inner wall (A_{geom}). The active surface area is determined by common analytical procedures such as hydrogen or carbon monoxide chemisorption.

2.2.4 Implementation – The DETCHEM Package

Deutschmann and co-workers developed a library of FORTRAN routines to simulate the kinetics of complex chemically reacting systems using detailed chemistry (DETCHEM). Detailed chemistry refers to the detailed description of a chemical reacting system using exclusively elementary-step reaction mechanisms (see Section 2.2.1).

Reactions are separated in two categories in DETCHEM, gas-phase reactions – reactions in the flow field – as well as surface reactions – heterogeneous reactions on a catalytically active component.

Tischer developed a CFD module for the DETCHEM package – DETCHEM^{CHANNEL}. DETCHEM^{CHANNEL} simulates annular flows such as the flow inside tubular reactor, *e.g.*, the channels in a honeycomb monolith [23]. Tischer and Fechtenkötter developed DETCHEM^{MONOLITH}, a code that utilises DETCHEM^{CHANNEL} to simulate the transient thermal

behaviour of a 3-dimensional catalytic monolith [23, 58]. In the presented work, a code that utilises DETCHEM^{CHANNEL} to simulate the transient behaviour of a catalyst operated under altering fuel-lean/-rich conditions was developed (DETCHEM^{TRANSIENT}). In automotive catalytic converters, only reactions on precious metal surfaces are of importance and therefore only the implementation of surface chemistry in DETCHEM is discussed in detail here.

Surface Chemistry - DETCHEMS

A pre-processor for DETCHEM reads a list of species as well as reactions provided by the user. The corresponding thermodynamic and molar data are derived from databases. The reaction mechanism is given by elementary-step reactions with corresponding, coverage-dependent kinetic parameters as required by Equations 2.30 and 2.31. Adsorption is described in terms of sticking coefficients (Eq. 2.32).

Time integration of the equations of the surface coverages is carried out according to Equation 2.35. The resulting differential algebraic equation (DAE) system (Eq. 2.35) is solved using LIMEX, a semi-implicit extrapolation solver [59]. An expression for the analytic Jacobian matrix of this differential equation system is precomputed to accelerate later computations. The software applies the theoretical foundation explained in Sections 2.2.1-2.2.3.

Annular Flow - DETCHEM^{CHANNEL}

As explained in Section 2.2.2, for annular flow fields with a convective transport in axial direction fast enough to neglect the diffusive transport in axial direction, the boundary layer approximation to the Navier-Stokes equations can be applied. Heterogeneous reactions can be coupled to this flow field calculation by introducing the boundary condition (Eq. 2.48).

The equation system (Eqs. 2.43 - 2.47) is discretised using a finite-volume procedure [60] resulting in a system of first order differential equations in terms of the axial coordinate z . In combination with the boundary conditions, a parabolic differential equation system is generated. This DAE system is as well solved using the mentioned semi-implicit extrapolation solver LIMEX [59].

DETCHEM^{CHANNEL} calculates axial and radial velocities, mass fraction of the chemical gas-phase species and the temperature for every position in the annular reactor. Surface

coverages are computed as function of the axial coordinate z . As input, the reactor has to be characterised by giving its geometry (diameter and length), the inlet gas composition, temperature, velocity, operating pressure and the catalyst wall temperature profile. Alternatively, adiabatic conditions can be chosen. For details of the boundary layer approach and its implementation in DETCHEM, see [23].

Altering Inlet Conditions and Transient Surface Chemistry – DETCHEM^{TRANSIENT}

Even though transient processes in heterogeneous catalysis can be simulated by commercially available Navier-Stokes based codes like FLUENT [61], these models are not applicable owing to the stiffness of the mathematical description and the consequent high CPU costs [62].

However, based on the idea of time scale decoupling according to the hierarchical approach (see Chapter 1), the transient inlet gas composition (time scale of seconds) can be regarded as decoupled from the residence time of the gas inside the reactor (time scale of milliseconds). Furthermore, the flow field in the catalyst can be assumed quasi-steady-state during the time step necessary for the accurate resolution of the surface chemistry. Surface chemistry is treated transiently using Equation 2.35.

DETCHEM^{TRANSIENT} a control unit for DETCHEM^{CHANNEL} that was developed in the scope of this research provides the CFD code with the current inlet gas composition, temperature and the surface coverages inside the reactor. The variance in surface coverages is then calculated by DETCHEM^{TRANSIENT} utilising DETCHEMS according to Equation 2.35, and the absolute surface coverages θ_i for all surface species i is then calculated by integration of Equation 2.35. The accuracy of the model can be determined by adjusting the time step Δt . The shorter the time step Δt , the more precise the model and the longer the computational time necessary.

Mode of Operation

A schematic overview on the interplay of the different DETCHEM modules for transient simulation is given in

Figure 2.8. The different steps are explained in detail in the text; the step numbers are given in

Figure 2.8 beside the head of the arrow corresponding to the calculation step.

DETCHEM^{TRANSIENT} initialises DETCHEM^{CHANNEL} with the initial temperature and inlet gas composition at t_0 provided by the user (step 1). Subsequently, DETCHEM^{CHANNEL} calculates the flow within the tubular reactor, based on the initial temperature and inlet gas composition. The gas-phase species concentrations calculated by DETCHEM^{CHANNEL} provides DETCHEMS with basis for the calculation of surface reaction rates (step 2, see also Section 2.2.3). The production/consumption of species \dot{s}_i is then coupled to the flow field in terms of R_i^{het} according to Equation 2.48. (step 3). DETCHEMS provides DETCHEM^{TRANSIENT} with the variance of the surface coverages (Eq. 2.35, step 4), which is integrated by DETCHEM^{TRANSIENT}. The absolute surface coverage is then passed back to DETCHEMS as initial value for the next time step (step 5) and furthermore filed. The calculated outlet gas composition is finally provided to DETCHEM^{TRANSIENT} by DETCHEM^{CHANNEL} (step 6). Both surface coverage and outlet gas composition at each time step is filed by DETCHEM^{TRANSIENT}. The inlet gas composition is then adjusted for the subsequent time step according to the input data provided by the user.

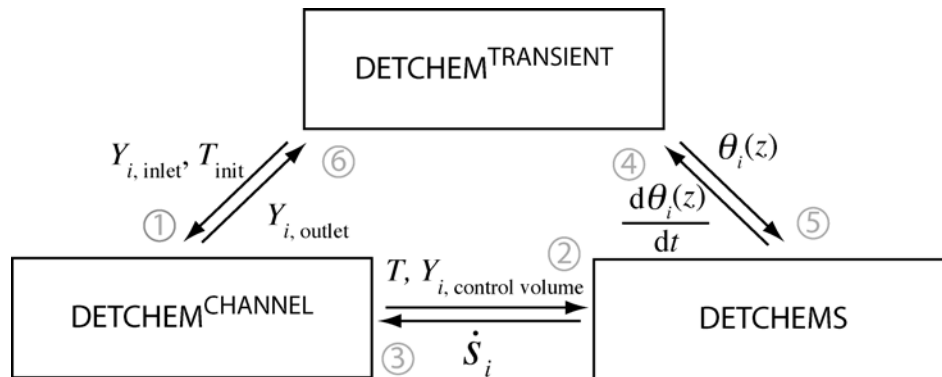


Figure 2.8: Schematic overview over the implementation of transient reacting flow simulation by DETCHEM

The described iteration is carried out for each time step. For the time resolution it is referred Figure 2.9. It will be shown that this approach provides results in agreement with experimental investigations (Chapter 9). In case of catalytic combustion, it was already shown by Raja *et al.* [62] that the accuracy of the boundary layer approach does not differ much from that of the Navier-Stokes approach, while calculations based on the former approach consume considerable less computational time.

Next to the input data for DETCHEMS and DETCHEM^{CHANNEL}, the user has to provide DETCHEM^{TRANSIENT} with the different species concentrations of the inlet gas ($Y_{i, \text{inlet}}(t)$), the duration of both phases, the time step Δt and the initial surface coverage $\theta_i(t_0)$. As output, DETCHEM^{TRANSIENT} creates files with the species concentrations in the outlet gas as a function of time $Y_{i, \text{outlet}}(t)$ and the surface coverages as a function of time and axial position $\theta_i(z, t)$. This output is given in two formats, one compatible for visualisation with TecPlot (UNIX, LINUX and MS Windows) and one for visualisation with Kaleida Graph (Apple Macintosh).

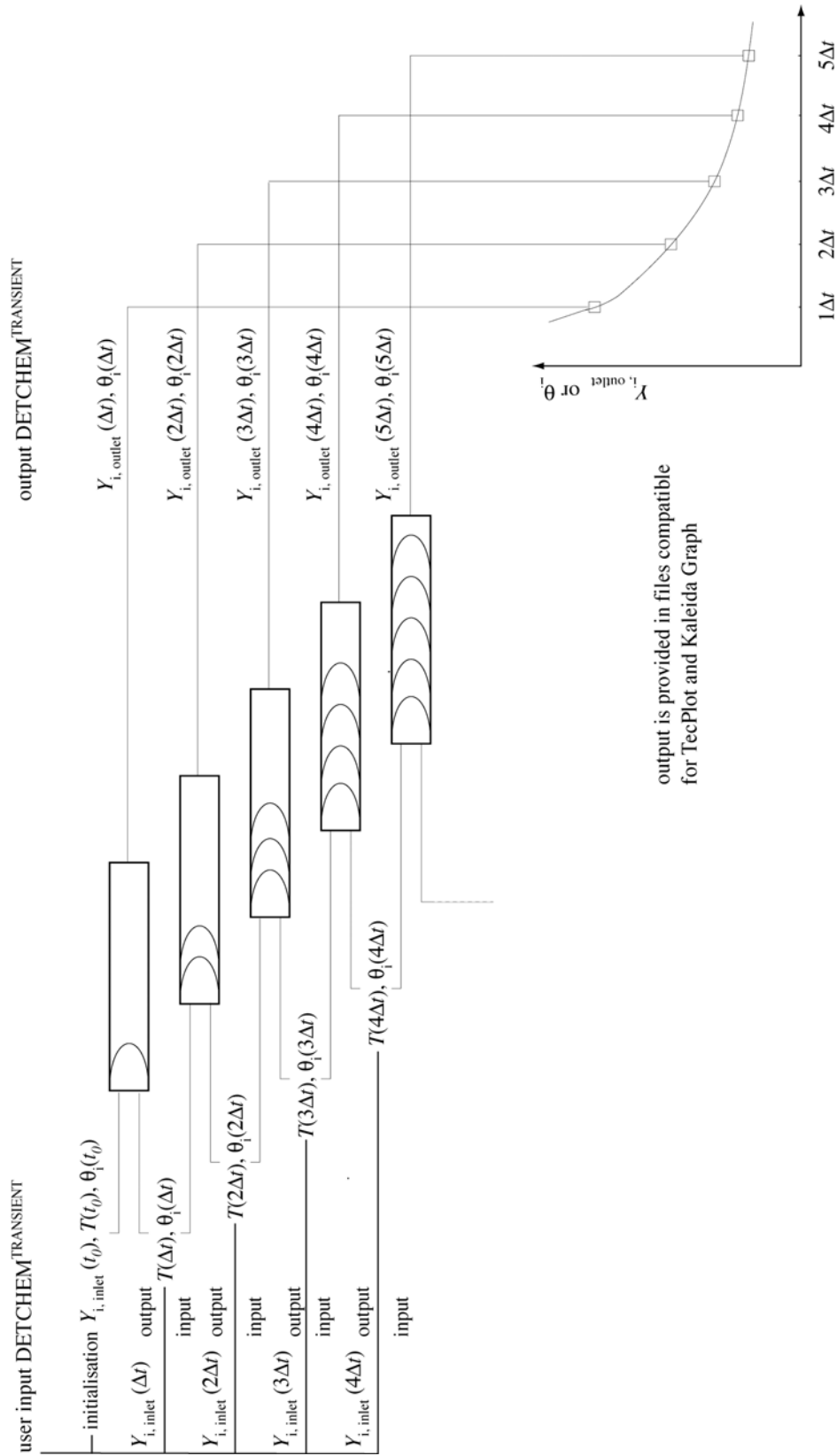


Figure 2.9: Schematic illustration of the transient modelling of a catalytically active monolith channel using DETCHEM^{TRANSIENT}

Chapter 3: Simulation of the Transient Behaviour of a Single Monolithic Channel

3.1 Motivation

In order to verify if the newly developed DETCHEM module TRANSIENT can indeed predict the transient behaviour of a monolithic catalyst, especially the behaviour of the catalytic system proposed by Nakatsuji [15, 16, 63, 64], a comparative study between measurements of transient conversions in a monolithic catalyst loaded with rhodium and transient simulation of such a system was conducted.

If this rhodium-based catalyst is operated alternately under short lean (oxidising) (time scale of the order of seconds) and very short rich (reducing) (time scale of the order of 0.1 s) conditions, it is highly active towards NO_x decomposition. In addition, the catalyst appears to be sulphur-resistant, an issue that is highly desired as well.

The mechanism suggested by Nakatsuji is as follows: NO_x decomposes on clean rhodium, forming N₂ and an oxidised rhodium surface, which is inactive towards further NO_x decomposition. During rich phases, adsorbed oxygen is removed from the rhodium surface by reductants, and herewith a clean rhodium surface, which is again active towards NO_x decomposition, is generated.

The reaction mechanisms for carbon monoxide and hydrogen oxidation, NO decomposition and nitrogen formation are already established; kinetic data have been gathered from different experimental techniques, see Appendix A and [11]. To verify if these mechanistic data are sufficient to describe this transient operated catalytic system, models based on these elementary steps were compared to experimental data.

The starting point of this study was to use the simplest possible model exhaust for DeNO_x catalysis, nitrogen monoxide and hydrogen or carbon monoxide as reducing agent. The chemistry model was based on reactions for hydrogen decomposition/recombination, water formation, NO decomposition, oxygen decomposition/recombination and nitrogen

recombination (for details it is referred to Appendix A). Characterisation of the catalyst and a description of the experimental techniques are given in Appendix C. More realistic model exhaust gases are currently under investigation [65].

3.2 Results and Discussion

3.2.1 Operation with Altering Feed Composition

The conversion of pulses of 2.5 % V/V CO into a stream of 10 % V/V oxygen in argon was simulated for different temperatures. The light-off temperature of the CO oxidation over rhodium is approximately 330°C. 30°C below the light-off temperature, the 1-second carbon monoxide pulses pass through the monolith completely unaffected (Figure 3.1, top left). 20°C above the light-off temperature of the carbon monoxide, the pulses leave the catalyst as carbon dioxide (Figure 3.1, bottom).

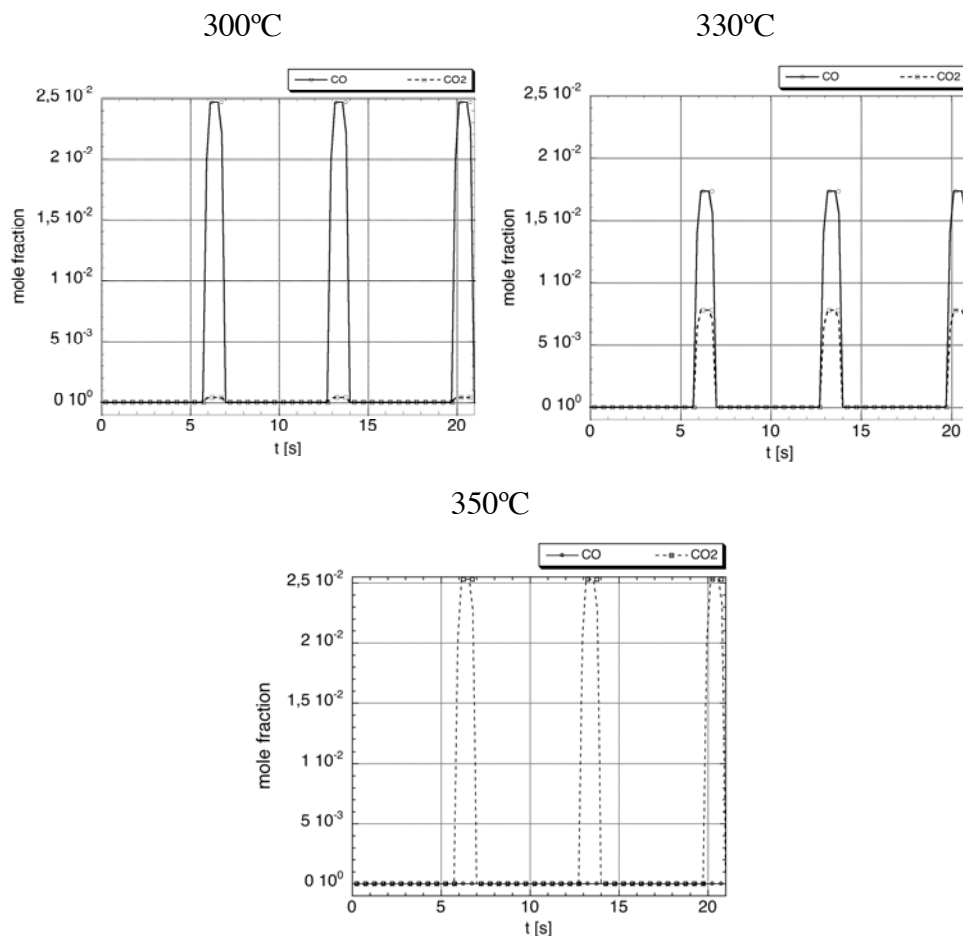


Figure 3.1: Calculated conversion of carbon monoxide pulsed to mixture of 10 % V/V of oxygen in argon as a function of time for three temperatures

For these calculations it was assumed that the rhodium surface is clean at $t = 0$. However, since this is definitely not the case in a real catalytic converter, different overlays were chosen as starting point. Conversions in a catalyst at 350°C with the rhodium surface fully oxidised ($\theta_0 = 1$) as well as oxidised to 50% ($\theta_0 = 0.5$) are shown in Figure 3.2.

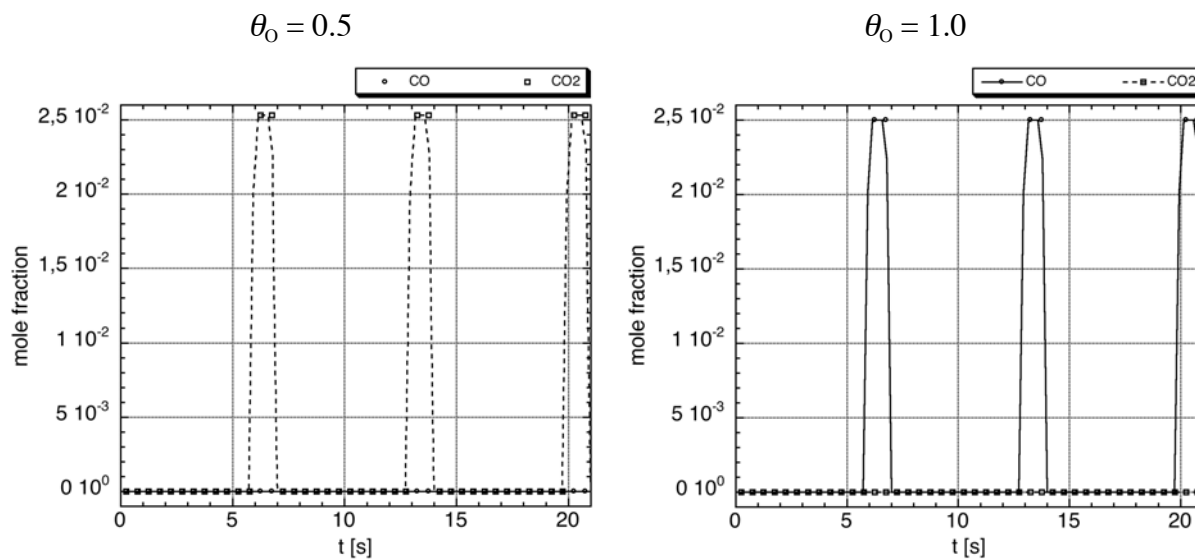


Figure 3.2: Comparison of CO conversion as a function of time with different surface coverages at t_0 ($\theta(t_0)$)

As can be seen in the left graph (Figure 3.2), a partially oxidised rhodium surface does not affect the conversion of CO, while the catalyst is absolutely inactive in case of the fully oxidised surface (right graph, Figure 3.2). This is in agreement with experimental observations [66]. Fully oxidised rhodium surfaces are inactive, because the desorption temperature of oxygen is rather high and, hence, no vacant adsorption sites are accessible for CO at 350°C. Hence, even though the oxidation light-off temperature is reached, CO passes the catalyst unaffected. However, this is not a realistic scenario, since a fully oxidised rhodium surface is rather unlikely, see Chapter 5.

3.2.2 Comparison of the Outlet Gas Composition with Experimental Data

Investigating the reduction of NO_x and the amount of nitrogen formed is difficult, because CO and N_2 have the same molecular mass. Hence, to monitor the formation nitrogen by

means of mass spectrometry, either a reductant with isotopically labelled carbon or a carbon free reductant has to be utilised, otherwise the mass peaks of CO and N₂ overlap. Since labelled carbon compounds are very expensive and therefore not applicable for transient flow measurement, a carbon-free reductant such as hydrogen has to be used. Owing to these reasons, the first comparative study of simulations with DETCHEM^{TRANSIENT} and transient measurement of conversions in a rhodium-based monolithic catalyst were carried out using this reductant [67, 68].

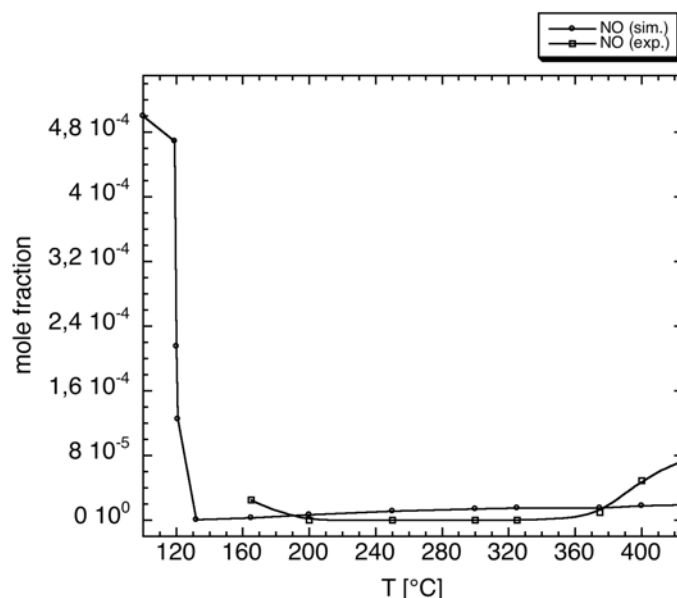


Figure 3.3: Comparison between measured and calculated mean NO outlet gas concentration over periodic lean-rich cycles [65]

A stream of 500 ppm NO with 2 % V/V hydrogen in argon, in turn with 12 % V/V oxygen (lean) and without oxygen (rich) was led through a monolith coated with a rhodium-based catalyst. A 6-second lean phase was followed by a 1-second rich phase. The conversions were measured according to the standard lab procedure used by hte AG⁷ between 150 and 450°C. As can be seen from Figure 3.3, almost all NO is reduced within the relevant temperature range.

A comparison of the average outlet gas compositions to values calculated by DETCHEM^{TRANSIENT} shows a good agreement (Figure 3.3). Only for higher temperatures the

⁷ Industrial partner of the ConNeCat project

DeNO_x activity is slightly overestimated. For more detailed studies and comparison of N₂ selectivity of the catalyst it is referred to forthcoming publications [65, 69].

3.2.3 Time Resolution of the Surface Coverage

Looking at the coverage of the rhodium surface as a function of time (Figure 3.4) for the system described in Section 3.2.2 shows that during the lean periods the surface is 90% covered with oxygen and about 10% with nitrogen.

During the subsequent rich periods, the surface is reduced (see square-marked line) and nitrogen accumulates on the surface (see diamond-marked lines). During the reducing periods vacant surface sites (see circle-marked lines) are generated. This is a crucial issue for NO decomposition, since a vacant site is required for this process (see Reaction Equation 3.52).

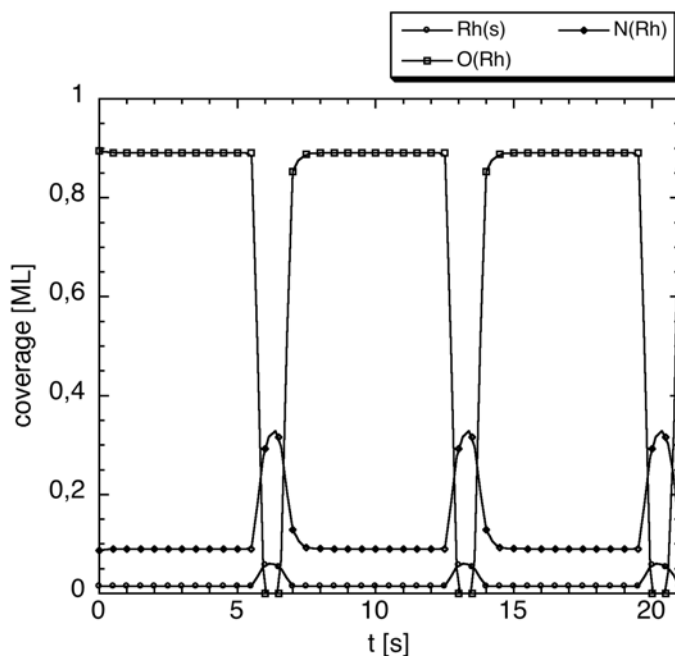


Figure 3.4: Rhodium surface coverage during periodic operation, every second calculated value is marked in the graph

The observed accumulation of atomic nitrogen on the rhodium surface during the reducing phases points towards a preferred nitrogen (N₂) formation during this period. Comparing the

N_2 formation and the nitrogen surface coverage as a function of time (Figure 3.5) shows that the nitrogen production indeed increases by 25 % during the reducing phases. When the operation conditions are switched back to oxidising, the nitrogen surface coverage and the nitrogen production decrease.

However, a comparison of the simulated nitrogen surface coverage of a catalyst operated without oxygen-depleted phases and one with the periodic operation as explained above, leads to the conclusion that the difference in N_2 production is only owing to the decreased λ_{ox} -value during the oxygen-depleted phase and not to an activation process.

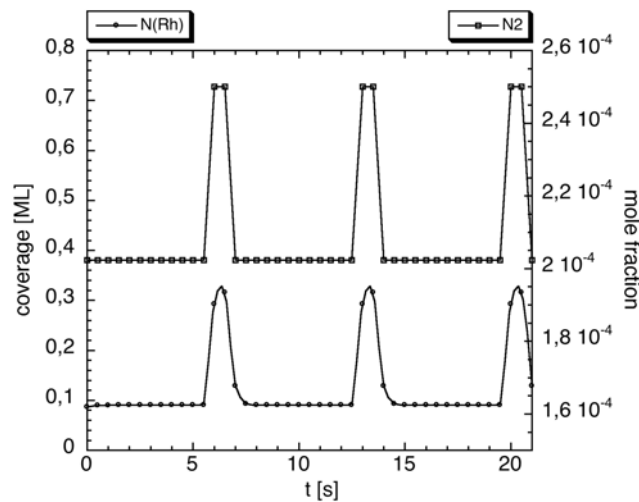


Figure 3.5: Comparison of calculated nitrogen surface coverage and nitrogen formation

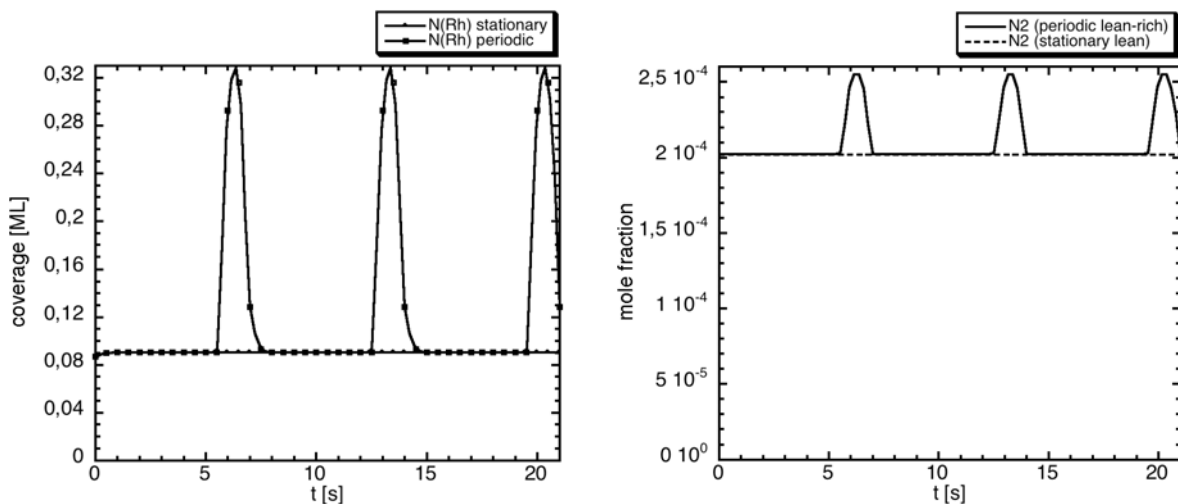


Figure 3.6: Comparison of the calculated nitrogen surface coverage (left) and calculated nitrogen production (right) of a catalyst operated under steady-state lean and periodic lean-rich conditions

This result is in contrast to the mechanism proposed by Nakatsuji. He suggests that the nitrogen is mainly formed during the lean phase after reduction of the surface, while simulations support that during the rich phases the nitrogen formation is dominant. Nonetheless, our simulations support that the surface is indeed reduced during the rich phase.

In order to verify if the calculated nitrogen production in this model is an artefact of the periodic operation, the simulations were compared to simulations with steady-state lean conditions. This time the λ_{ox} -value was chosen such that the mean λ -value of the periodic operations equals the λ_{ox} -value of the steady-state operation.

The mean N_2 production over three lean-rich cycles compared to the N_2 production under steady-state lean conditions ($\bar{\lambda}_{\text{ox}}^{\text{periodic}} = \lambda_{\text{ox}}^{\text{stationary}}$) shows that the enhancement by periodic operation is minor (Figure 3.7).

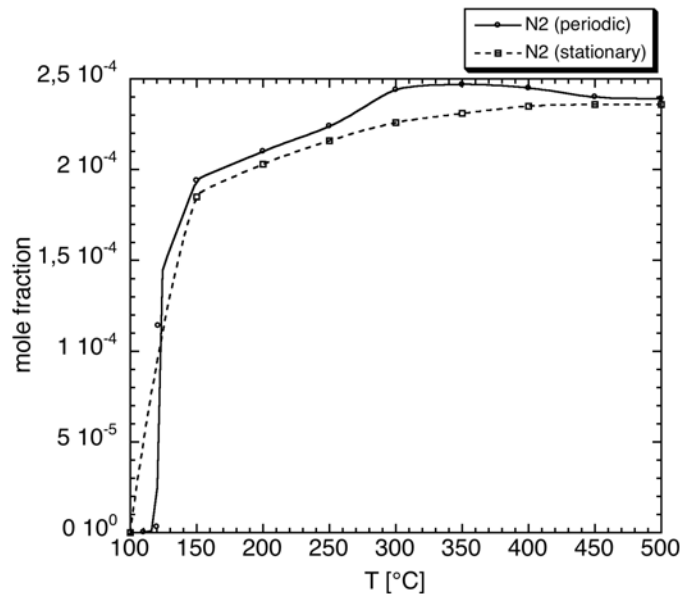


Figure 3.7: Comparison of the N_2 production under periodic and steady-state operation

Between 300°C and 350°C, the discrepancy in the simulated N_2 production is most distinct. The periodic operation leads to a maximal increase of only 7.9 % in this region, and for the remaining temperature range the difference is negligible. This leads to the conclusion that, based on the mechanism used, the gain in N_2 production is only due to the lower overall λ_{ox} -value and not to the periodic operation.

Since measurements carried out within the ConNeCat research consortium support the enhancement of this rhodium-based catalyst by periodic lean-rich operation, it seems that the mechanism used is not sufficient to describe the benefits of the periodic operation. Nonetheless, the mechanism of NO and H₂ decomposition, N₂ and water formation and the corresponding kinetic data were already carefully benchmarked to experiments [11, 70-72]. This leads to the assumption that the discrepancy between experiment and simulation of the catalytic system is owing to the dynamic behaviour of the composition of the surface overlayer. A possible source of error could lie in the rather high oxygen coverages calculated for rather low temperatures. Therefore, a system of 500 ppm NO in argon with a pulse of 2% V/V hydrogen without oxygen was investigated.

3.2.4 Nitrogen Monoxide Reduction by Hydrogen Pulsing

In absence of oxygen, the clean rhodium surface (starting point of the simulation) is very fast oxidised by NO decomposition and nitrogen formation (see $t = 0-1$ s of the graphs in Figure 3.8). The amount of nitrogen formed in this period is so minor that it is within the numerical error of our simulations. Nitrogen monoxide passes the oxygen-poisoned catalyst without being affected. When hydrogen is pulsed to the system ($t = 1-2$) the surface is reduced, $O_{(Rh)}$ decreases to almost 0 ML. At the same time, the amount of atomic nitrogen on the surface ($N_{(Rh)}$) increases up to 0.3 ML. Simultaneously with this rearrangement of the surface overlayer, the NO conversion lights off and nitrogen formation sets in (see Figure 3.8, left graph).

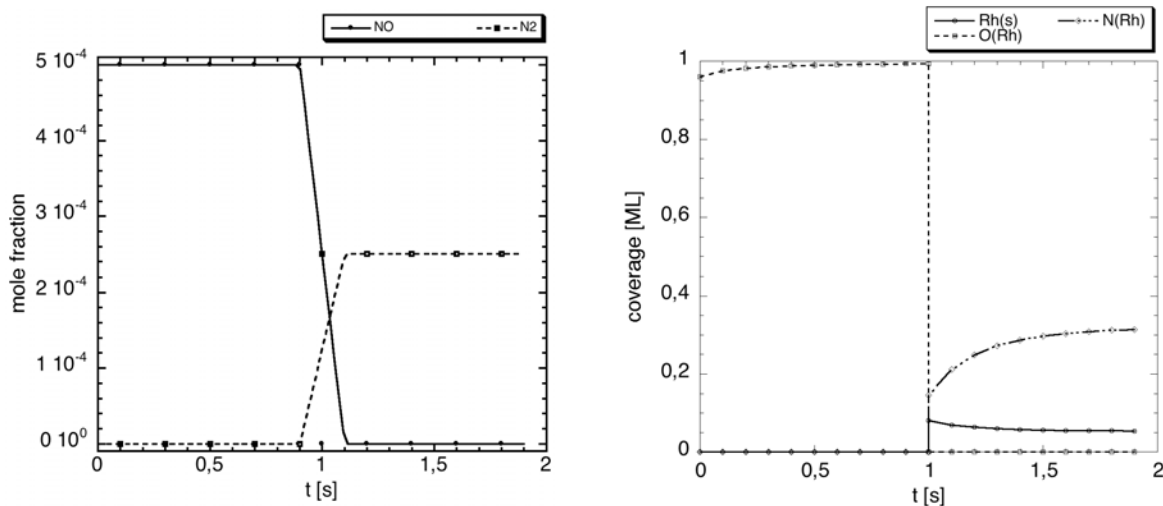


Figure 3.8: 500 ppm NO in argon lead through a rhodium-based catalyst with a pulse of 2% V/V hydrogen at $t = 1$ s

An examination of the system over a longer period, shows that hydrogen pulses of 1 s can reduce the surface very fast, however, after the hydrogen is withdrawn from the feed, the surface is poisoned by oxygen instantaneously (Figure 3.9). This is not in agreement with Nakatsuji's proposal, since nitrogen is not formed during the lean operation.

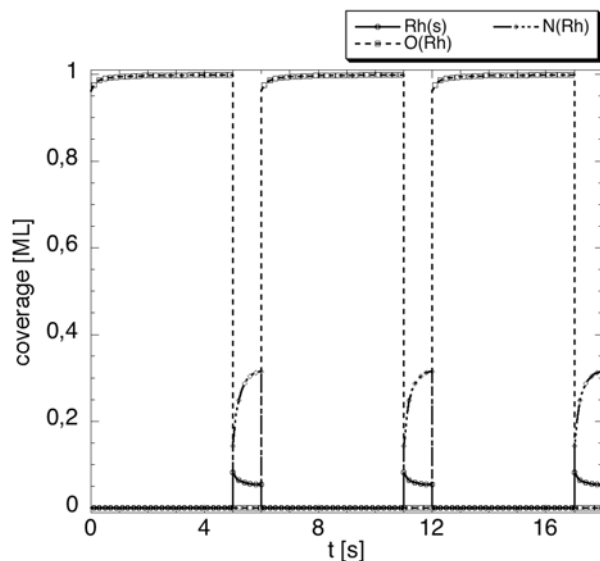


Figure 3.9: 500 ppm NO in Ar with three pulses hydrogen of 1 s

Addition of 14.5 % V/V of oxygen to the feed⁸ illustrates the influence oxygen exhibits on the surface chemistry. Surface oxygen atoms originating from NO decomposition are marked with an asterisk, unmarked O refers to oxygen atoms generated by O₂ decomposition (Figure 3.10).

⁸ Condition recommended by the ConNeCat project executing organisation

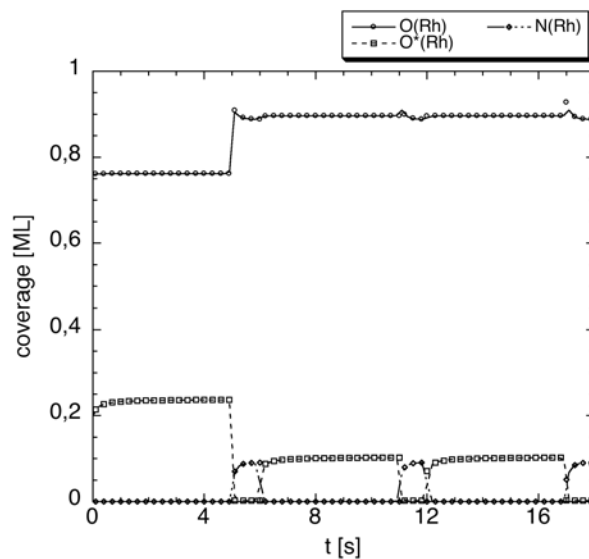


Figure 3.10: Main adsorbants on the rhodium surface during periodic operation; oxygen originating from NO decomposition is marked with an asterisk

According to our calculations, it appears that the metal surface under the conditions given by the project-executing organisation is immediately poisoned with oxygen mainly originating from O_2 decomposition,

A review of the surface science literature lead to the conclusion that the differences of experiment and simulation may be explained after understanding the details of the nature of oxygen and its reactions on rhodium, see subsequent paragraph.

Oxygen Coverage

Calculations predict that the rhodium surface is immediately completely covered with atomic oxygen when exposed to 2 % V/V of oxygen in argon at room temperature. In contrast, surface science investigations support that a complete oxygen overlayer on rhodium is difficult to achieve even at elevated temperature and with strong oxidising agents such as NO_2 . This discrepancy is possibly the source of error in the misprediction of the conversions. Since kinetic simulations based on the Arrhenius parameters used in the presented work could be successfully compared to experimental data of steady-state processes [11, 70, 71], they cannot be completely inaccurate. A possible specification missing in the mechanism is the dependence of the kinetics on the oxygen coverage of the surface. This may explain why in

steady-state processes with low partial oxygen coverage⁹ the kinetic parameters are sufficient to describe the behaviour observed experimentally, while they are not in case of high partial oxygen coverage.

3.3 Conclusions

In this chapter it was shown that the developed code DETCHEM^{TRANSIENT} is in principle able to describe the transient behaviour of monolithic catalyst. Moreover, a comparison of the mean outlet gas composition of a periodic lean-rich operated catalytic monolith to simulation results showed that the results of the simulations are fairly accurate (Figure 3.3).

However, the predicted span of time in which nitrogen is formed is not in agreement with the mechanism proposed by Nakatsuji (Figure 3.5). Furthermore, simulation results indicate that the benefits of periodic operation are minor (Figure 3.7).

According to surface science investigations, the calculated partial oxygen coverages are by far too high (Figure 3.10), which could be a possible source of error. Based on this knowledge, a conclusion drawn was that the kinetics of oxygen and nitrogen oxide decomposition on rhodium might be coverage-dependent. These dependencies can be investigated by surface DFT investigations, see Chapters 5 - 6.

Investigation of the Surface Chemistry

The close-packed (111) facet is generally the dominant face in real fcc metal catalyst particles [73]. Monatomic steps are possibly the most common defects on these closed packed surfaces. To investigate the chemistry of nitrogen oxide and oxygen on real metal catalyst particles, surface chemistry on the (111) facet as well as on steps has to be considered. A possible model for steps is vicinal surfaces such as the (311) surface, in which the (111) plane is interrupted by (100) monatomic steps.

Based on these considerations, the surface chemistry of nitrogen oxide and oxygen on rhodium was investigated by means of DFT calculations using the plane, close packed (111) facet (Chapters 4-7) as well as stepped rhodium surfaces, *i.e.*, the (311) and (211) facet (Chapter 8).

⁹ The rhodium mechanism was originally developed for high-temperature processes with low partial oxygen coverage.

Chapter 4: Carbon-Monoxide-Adsorption and -Coadsorption on Rhodium(111)

4.1 Motivation

A comparative study of calculation results with experimental data was carried out in order to verify if the DFT-GGA geometry optimisations of adsorbants on metal surfaces are accurate. In order to ensure that accordance is not an artefact of doubtful measurement, a system, which is experimentally thoroughly investigated, namely carbon monoxide on rhodium(111), was chosen for this verification.

Additionally, in contrast to oxygen and nitrogen oxides, CO does not contain unpaired electrons. Hence, spin effects do not affect the energy of this system, thus excluding a possible source of error. Furthermore, the calculation times are shorter when spin effects are negligible, since only one electron density is calculated instead of two (see Chapter 2). Different CO coverages on Rh(111) were examined and the influence of atomic oxygen as coadsorbant was studied.

4.2 Results and Discussion

4.2.1 Carbon Monoxide on Rhodium(111)

A rhodium(111) surface with a carbon monoxide overlayer of $1/3$ in a $(\sqrt{3} \times \sqrt{3})\text{-R}30^\circ$ elementary cell was optimised as described in Chapter 2. The calculations are in good agreement with LEED studies carried out by Gierer *et al.* [74].

The surface occupation found by DFT calculations perfectly resembles that found by low energy electron diffraction (LEED) analysis. Furthermore, the DFT study predicts bond lengths within the experimental error limits.

The CO was found to occupy on-top sites on the rhodium(111) surface by LEED analysis as well as DFT calculations (Figure 4.1). The carbon-oxygen distance of the adsorbed carbon monoxide was calculated to be 122 pm compared to $120 \text{ pm} \pm 5 \text{ pm}$ determined by LEED. The rhodium carbon distance was calculated to be 183 pm compared to the experimentally determined $187 \text{ pm} \pm 4 \text{ pm}$. The calculated rhodium interlayer spacing of 226 pm also lies within the experimental error limits (LEED: $222 \text{ pm} \pm 5 \text{ pm}$ [74]). A lateral as well as an on top view is shown in Figure 4.1, and a comparison of calculated and measured distances is given in Table 4.1.

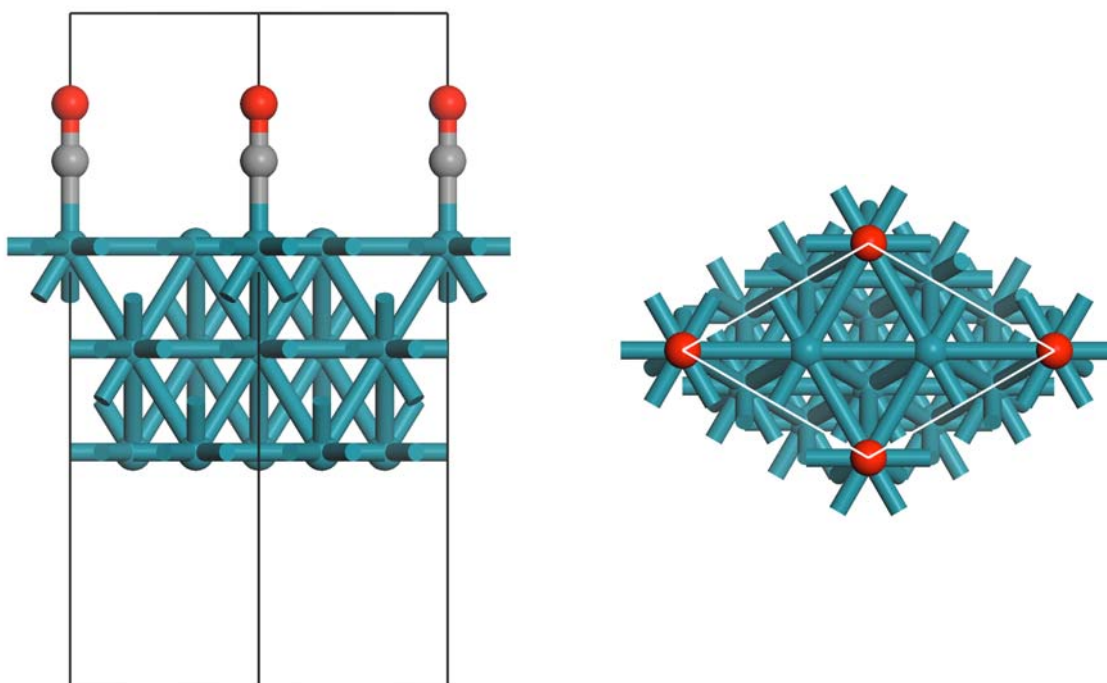


Figure 4.1: $(\sqrt{3} \times \sqrt{3})$ -Rh(111)-CO, lateral and on-top view

distance (pm)	LEED	DFT-GGA
on-top		
C-O	120 ± 5	122
Rh-C	187 ± 4	183
Surface interlayer spacing	222 ± 5	226

Table 4.1: Comparison of the DFT-GGA computations with LEED results [74]

An analogue optimisation was carried out for a rhodium(111) surface with an carbon monoxide overlayer of 0.75. An optimum geometry of (2×2) -3 CO in the same elementary cell as reported by Somorjai and co-workers was found [74]. Two carbon monoxide molecules were found to reside in 3-fold positions (fcc and hcp) perpendicular to the surface while one was found to reside in on-top position, again in conformance with the symmetry found by LEED studies. This configuration is the only one found in which CO occupies highly symmetrical adsorption sites and forms a hexagonal overlayer.

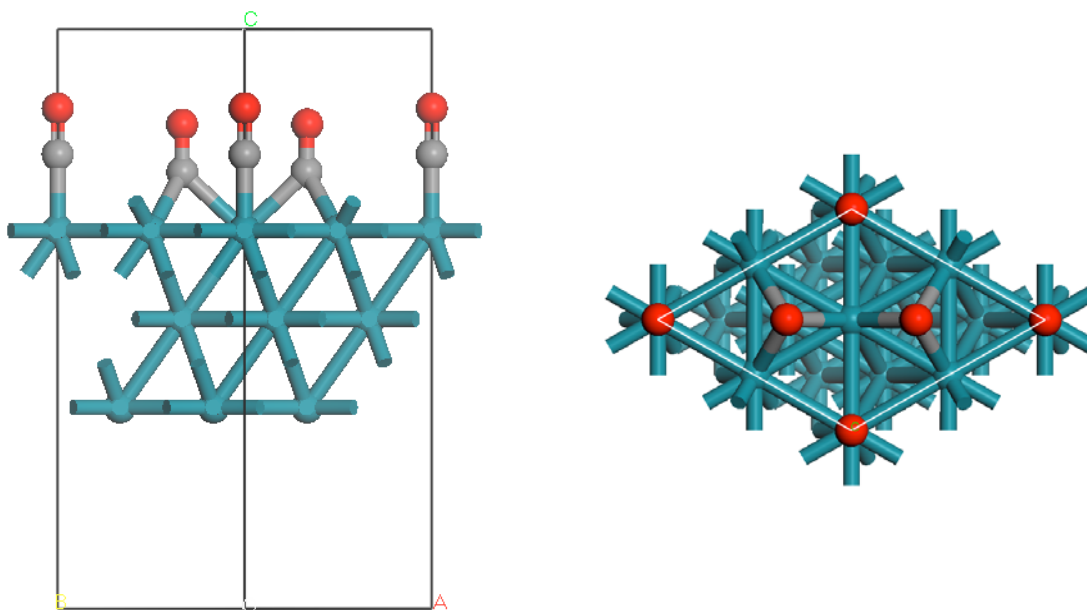


Figure 4.2: On-top and lateral view of the super cell of (2×2) -Rh(111)-3 CO

The carbon atoms of the 3-fold COs reside 144 pm above the rhodium(111) surface according to DFT calculations (LEED: $147 \text{ pm} \pm 4 \text{ pm}$ [74]). The calculated C-O bond length of 118 pm perfectly resembles the experimentally observed distance of 118 pm [74].

The carbon atom of the on-top adsorbed carbon monoxide resides 189 pm over the rhodium(111) surface according to DFT calculations. The position of the carbon is confirmed by the experimental results of $195 \text{ pm} \pm 6 \text{ pm}$ [74]. The rhodium interlayer spacing was calculated to be 226 pm in accordance with the LEED result of $226 \text{ pm} \pm 4 \text{ pm}$ [74]. An overview of LEED and DFT results is given in Table 4.2.

distance (pm)	LEED	DFT-GGA
on-top		
C-O	120 ± 5	122
Rh-C	195 ± 6	189
3-fold (fcc & hcp)		
C-O	115 ± 7	118
C-surface	147 ± 4	144
surface interlayer spacing	226 ± 4	226

Table 4.2: Comparison of the DFT-GGA computations with LEED results [2]

4.2.2 Carbon Monoxide and Atomic Oxygen on Rhodium(111)

A rhodium(111) surface with carbon monoxide as well as atomic oxygen coadsorbed ($\theta = 0.5$, $\theta_{\text{O}} = 0.25$, $\theta_{\text{CO}} = 0.25$) was optimised using DFT calculations as described for carbon monoxide. The calculations resemble LEED studies by Schwegmann *et al.* [75], precisely within the experimental error limits. In our model, atomic oxygen occupies a 3-fold-fcc position while CO occupies an on-top position (see Figure 4.3), a geometry that has also been determined using LEED [76].

The CO molecule is adsorbed end-on to the surface in a perpendicular fashion. The rhodium(111)-C distance is calculated to be 187 pm and is in very good accordance with the experimentally determined value of 183 pm ± 5 pm. The calculated C-O distance (115 pm) is also in very good accordance with the LEED result (119 pm ± 4 pm). Atomic oxygen resides according to the calculations in an 3-fold-fcc position 131 pm over the rhodium(111) surface (LEED, 128 pm ± 4 pm) with a Rh-O distance of 204 pm (LEED: 206 pm ± 6 pm [76]). An overview of LEED and DFT results is given in Table 4.3.

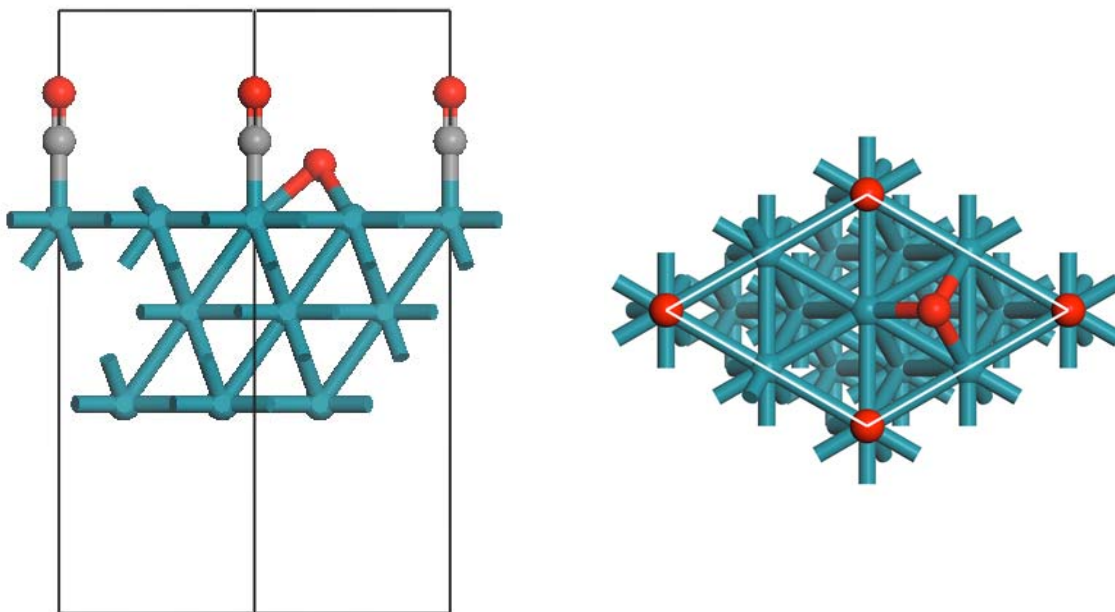


Figure 4.3: Lateral and on-top view of O and CO coadsorbed on rhodium(111)

Furthermore, the calculated interlayer spacing of 227 pm compared to $227 \text{ pm} \pm 3 \text{ pm}$ (LEED) is in very good agreement.

distance (pm)	LEED	DFT-GGA
on-top CO		
Rh-C	183 ± 5	187
C-O	119 ± 5	115
fcc hollow O		
Rh-O	128 ± 4	131
O-surface	206 ± 6	204
surface interlayer spacing	227 ± 3	227

Table 4.3: Comparison of the DFT-GGA computations with LEED results [76]

4.2.3 Electron Donation from the Surface to the Adsorbant

An effect, which directly influences any surface process is the electron transfer of the rhodium surface to the adsorbant. Therefore, it is essential to be able to measure the amount of negative charge transferred to the adsorbant upon adsorption or to the transition state of a surface reaction. A method to measure this charge transfer implemented in CASTEP is Mulliken charge analysis [77]. These Mulliken charges were calculated according to a formalism described by Segall *et al.* [78]. Siegel *et al.* applied this method successfully to measure charge transfer and bonding on aluminium surfaces [79].

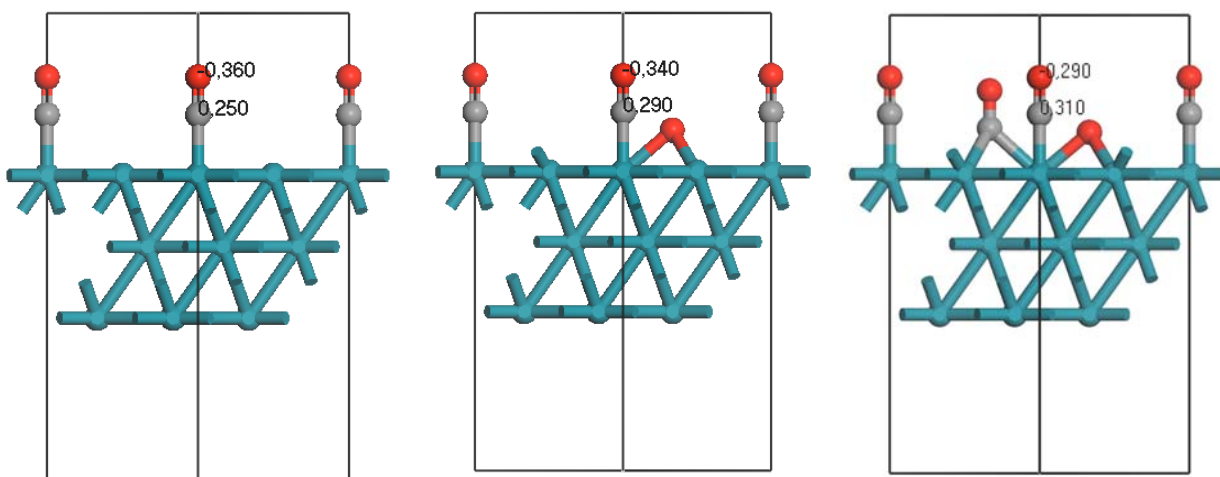


Figure 4.4: Mulliken charges of CO adsorbed and coadsorbed with O on (2 x 2)-Rh(111)

Since all adsorbants compete for charge density offered by the rhodium surface, the charge transfer will depend on the coverage as well as on the chemical nature of the adsorbants. As an example, the adsorption of CO as well as its coadsorption with atomic oxygen was studied using this charge analysis. Carbon monoxide and oxygen compete for electron density in different ways. Carbon monoxide donates electron density to the surface via the coordination of the free electron pair localised on the carbon atom (σ -donation), but at the same time accepts electron density via donation to its antibonding π -orbital. Oxygen on the other hand withdraws electron density from the surface because of the large difference in electronegativity (inductive effect).

Therefore, the electron transfer to either adsorbant changes, when they are coadsorbed. This dependence was measured for on-top adsorbed carbon monoxide (i) on a (2x2) elementary cell and on the same elementary cell with (ii) atomic oxygen and (iii) atomic oxygen and a further CO coadsorbed. It will be shown that Mulliken charge analysis can monitor the reduced electron transfer, see following paragraph.

Rh(111)-(2 x 2) (on-top CO)	-CO	-CO-O	-2CO-O
Mulliken bond order (C-O)	1.34	1.37	1.41
Mulliken charge			
C	0.25	0.29	0.31
O	-0.36	-0.34	-0.29
CO distance (pm)	116	115	115
C-Rh distance (pm)	187	188	188

Table 4.4: Comparison of CO adsorbed and coadsorbed with O on (2 x 2)-Rh(111)

As can be seen from Table 4.4, neither the intermolecular CO bond length nor the carbon-rhodium distances changes significantly when further adsorbants are added to the (2x2) elementary cell of Rh(111). However, looking at the Mulliken charges and the Mulliken bond order, it is apparent that owing to the coadsorption and competition for offered electron density the charge transfer to the adsorbant changes.

Especially in the case of on-top CO, it can be seen from Mulliken bond order analysis that the back donation into the antibonding π -orbital of the CO decreases, because the bond order increases with increasing surface occupation (Table 4.4)

4.3 Conclusions

In this Chapter it was shown that DFT-GGA calculations predict adsorption geometries, which are well established in literature, accurately. Not only the adsorption geometries, but

also the interlayer spacing of the metal surface, the bond length of the adsorbants and the distances of the adsorbants to the surface can be predicted accurately using CASTEP geometry optimisation based on a GGA functional. Furthermore, Mulliken charge analysis can be used to monitor the electron transfer from the surface to the adsorbant.

These preliminary studies are important with respect to the calculation of kinetic parameters and thermochemical data, since the correct reactant and product geometries are essential for the accurate determination of the reaction trajectory and location of the transition state.

Chapter 5: Coverage Dependence of the Oxygen Decomposition

5.1 Motivation

In Chapter 3 it was observed that according to kinetic simulations, rhodium is instantaneously covered by atomic oxygen. This oxidised rhodium surface is inactive (poisoned) towards CO adsorption and oxidation.

However, as already mentioned, surface coverages on the close packed (111) facet of rhodium – the predominant facet in real fcc metal catalyst particles – are difficult to achieve. Considering these aspects leads to the assumption that these kinetic simulations do not determine the transient rhodium overlayer accurately.

Since the presented work deals with rhodium exposed to high concentrations of oxygen and with pulses of reducing feed gas at elevated temperature, the oxygen coverage might vary over a wide range during operation.

Owing to these reasons it is crucial to understand the thermochemistry as well as the kinetics of the oxygen decomposition on rhodium for the coverages relevant. Therefore, the thermochemistry as well as activation barriers for the oxygen decomposition on Rh(111) were studied by means of DFT-GGA calculations.

5.2 Results and Discussions

Prior to investigating the decomposition of oxygen on the (111) facet, the adsorption geometries of atomic and molecular oxygen were studied and, if possible, verified with experimental data.

5.2.1 Clean Rhodium and Molecular Oxygen

In a preliminary calculation the geometry of bulk rhodium was optimised. A lattice constant of 380.4 pm was detected which is in good agreement with the experimentally determined value of 380.3 pm [80, 81]. Furthermore, this result is similar to former DFT-GGA calculations [82, 83].

Molecular oxygen was optimised using the DFT-GGSA functional. The bond length of free triplet ground-state O₂ was calculated to be 121 pm (exp.: 121 pm [84]). When oxygen is placed in a supercell corresponding to that used in the subsequent chapter, the bond length increases to 123 pm. Both lengths indicate an oxygen-oxygen double bond.

5.2.2 Molecular Oxygen on Rh(111)

A situation with oxygen adsorbed perpendicularly to the metal surface (end-on) in a 3-fold (fcc) position on top of a Rh(111) with (2x2) periodicity (Figure 5.1) was the starting point of our study.

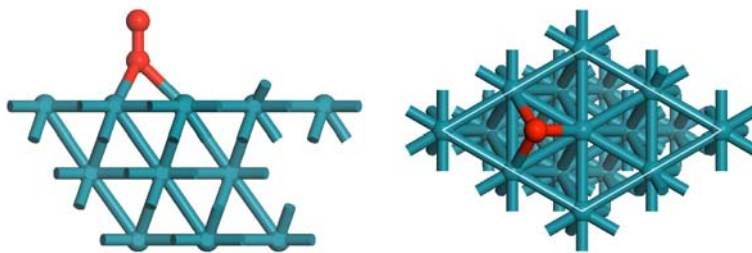


Figure 5.1: Dioxygen adsorbed in a 3-fold fcc position on Rh(111)

Walter *et al.* [85] showed that there is indeed a stable molecular oxygen species adsorbed on rhodium(111) which is non-paramagnetic in high coordination sites (hcp- as well as fcc-3-fold position). Our structure optimisations and energetic calculations confirm that there is a stable, non-paramagnetic end-on adsorbed molecular oxygen state on a fcc 3-fold site as well [86]. The oxygen atom pointing towards the surface is located 151 pm above it. Rhodium-oxygen distances are calculated to be 217 pm; the oxygen-oxygen distance is 133 pm according to our calculation.

In a first step, the dependence of the strength of the oxygen bonding on the oxygen coverage of the rhodium (2x4) surface was studied by calculating the heat of adsorption according to $\Delta E_{\text{ads}} = E_{\text{slab+O}_2} - (E_{\text{slab}} + E_{\text{O}_2})$. It could be shown that the bonding of molecular oxygen to the rhodium surface becomes weak at high oxygen coverages, these results are in accordance with a study carried out by Ganduglia-Pirovano *et al.* [83] for atomic oxygen. The heat of adsorption as a function of the initial surface coverage is depicted in Figure 5.2. It indicates that a minor initial oxygen coverage of the rhodium surface enhances the adsorption of further oxygen molecules while the process is inhibited at higher coverages and even blocked at coverages close to 1 monolayer. This effect might be electronically induced. The electronegative oxygen withdraws electrons from the metal surface and, hence, lowers the back-donation effect of the metal into the antibonding π -orbital of the adsorbed molecular oxygen species. This effect is hindered when further oxygen withdraws electrons from the metal atom.

The suggested weaker backdonation effect is supported by bond-length analysis: The O-O bond length of the adsorbed molecular oxygen decreases with increasing oxygen coverage from 131 pm ($\theta = 0.125$) to 126 pm ($\theta = 1$), indicating a higher bond order of the oxygen molecule. To determine whether the origin of this effect is indeed electrical, charge analysis of the end-on adsorbed species was carried out.

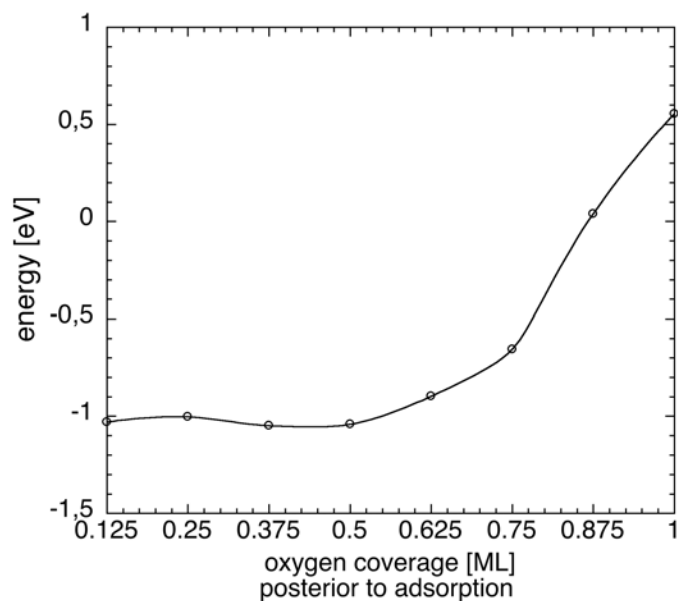


Figure 5.2: Heat of adsorption as a function of the initial oxygen coverage

a Mulliken Charge Analysis of the End-On Adsorbed Oxygen Molecule

Mulliken charge analysis of the end-on adsorbed O_2 molecule with different oxygen preoccupations was performed. The results show that the electronic donation from the rhodium surface to the adsorbed molecular species decreases with increasing oxygen preoccupation. As can be seen in Figure 5.3, the partial charges on the upper as well as the lower oxygen atom of the end-on adsorbed species decrease with increasing oxygen preoccupation. The weaker electron donation from the rhodium surface to the adsorbed molecule supports the decrease in adsorption energy calculated. Moreover, the charge analysis results are in agreement with the calculated bond length of the end-on adsorbed oxygen molecule. The contraction of the oxygen-oxygen bond with increasing oxygen preoccupation indicates a higher bond order, which is due to decreasing electron donation into the anti-bonding orbital as supported by Mulliken charge analysis.

Moreover, it has to be pointed out that the shapes of the coverage functions of the partial charges are similar to the shape of the coverage function of the adsorption energy, indicating that this effect is indeed electronically induced.

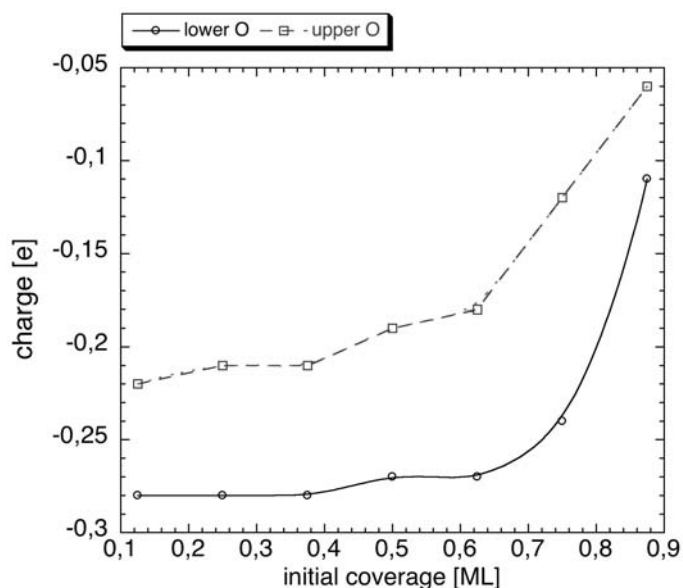


Figure 5.3: Mulliken charges of oxygen atoms of the end-on adsorbed oxygen molecule as function of the initial oxygen coverage. Lower oxygen refers to the oxygen atom bonded to the rhodium surface

To conclude, the decreasing adsorption energy calculated could support the mechanism proposed by Nakatsuji (see Chapter 1), because the oxygen coverage would possibly stagnate at a certain coverage. The effect may favour the adsorption and decomposition of nitrogen oxides and hence provide further insight into the functioning of the NO_x decomposition catalyst.

Atomic Oxygen on Rhodium(111)

The optimal geometry of atomic oxygen adsorbed in a 3-fold-fcc position on Rh(111) has been studied. In accordance with LEED studies [76, 83] and previous DFT calculations [85], geometry optimisations allow the conclusion that atomic oxygen preferably resides in 3-fold positions on the rhodium surface.

At a surface coverage of $\theta = 0.25$ (2 O-(2x2)/Rh(111)) the optimal distance for an atomic oxygen in fcc position was calculated to be 129 pm above the rhodium surface, well in agreement with LEED studies (124 pm \pm 6 pm) [76] as well as DFT calculations carried out by Ganduglia-Pirovano *et al.* [83]. The rhodium oxygen distance was calculated to be 202 pm (LEED: 200 pm \pm 8 pm) and the Rh-Rh interlayer spacing was calculated to be 223 pm again very well in accordance with experimental data (LEED: 224 pm \pm 4 pm) [76] and former DFT studies [83]. For atomic oxygen in a 3-fold-hcp position distances are only slightly different, the oxygen is located 129 pm above the rhodium surface in this model and the Rh-O distance was calculated to be 201 pm.

5.2.3 Decomposition Process

It is known that end-on adsorbed diatomic molecules preferably decompose with the breaking bond coordinated over a single metal atom rather than coordinated over a surface metal-metal bond [87]. Furthermore, they decompose in a fashion that after decomposition the surface adatoms share the smallest number of surface metal atoms possible (principle of least atom sharing) [88]. Based on this knowledge, a preferred final conformation of the dissociated molecule was assumed as depicted in Figure 5.4 (right).

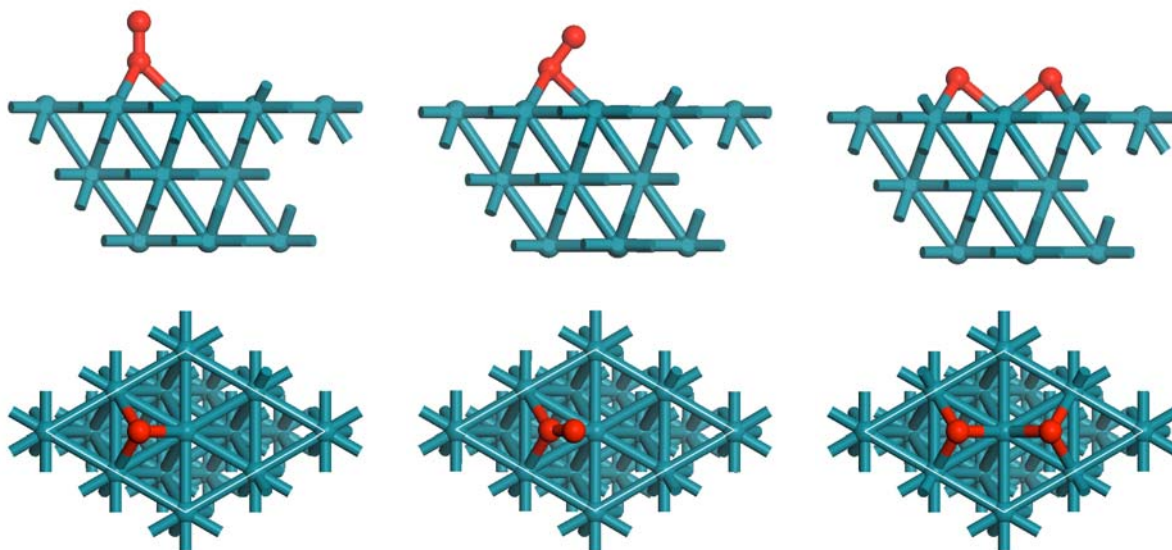


Figure 5.4: Adsorbed oxygen molecule, decomposition transition state and decomposed oxygen on (2 x 2)-rhodium(111)

Since atomic species are much more sensitive towards changes in surface configuration than molecular species (see the adsorption energies versus surface coordination number in Table 5.1), the energy of reaction strongly depends on the topology of the decomposed molecule rather than on the topology of the adsorbed molecule.

coordination number	O ₂	O
1	-0.06 eV	0.01 eV
2	-0.38 eV	-0.99 eV
3	-0.50 eV	-1.12 eV

Table 5.1: Influence of the surface coordination numbers onto the heat of adsorption of end-on adsorbed molecular oxygen and atomic oxygen

Figure 5.4 shows the computed optimal topologies for end-on adsorbed oxygen as well as its decomposition products. The computed transition state for the decomposition is also depicted, and it can be seen that first the oxygen-oxygen bond has to bend into the direction of the decomposing metal atom and in the transition state the oxygen atoms are still bonded to each other, while both are bonded to the decomposing rhodium atom. From the transition state (maximum energy point along the reaction coordinate), the oxygen atom simply ‘drops’ into

its preferred adsorption site, meaning that the process is going energetically strictly downhill as expected.

After placing additional atomic oxygen atoms (initial coverage (θ_{INIT}) = 0.5) on top of the rhodium surface, and recalculating the optimal geometries (starting materials/ products), a determination of the transition state as described in the Section 2.1.9 shows that the additional oxygen inhibits further decomposition of oxygen molecules, even though the decomposition is sterically still unhindered.

To investigate this effect in more detail, a surface with a (2 x 4) elementary cell consisting of 8 surface rhodium atoms was modelled in order to vary the initial oxygen coverage over a broader range. The atomic coordinates of the metal atoms have been constrained so that the (111) facet is conserved, while the adsorbates were assumed to be mobile. Only for high coverages ($\theta \geq 0.75$) constraints were imposed on the adsorbates, so that a vacant surface site adjacent to the oxygen molecule is available to ensure geometrically unhindered decomposition. The geometries for the oxygen molecule as well as its decomposition products were calculated for different oxygen coverages. The transition state of the reaction of the molecule to its decomposition products was determined for different initial oxygen coverages. As an example, the transition state of the oxygen decomposition at an initial oxygen coverage of $\theta_{\text{INIT}} = 0.625$ is shown in Figure 5.5. The activation energies as well as the reaction energies have been calculated according to Equations 2.17 and 2.18.

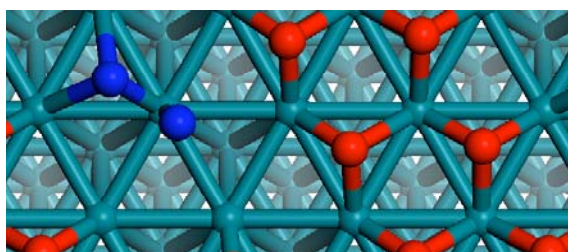


Figure 5.5: The transition state of the oxygen decomposition (left, marked by colour/shade) at an initial oxygen coverage of 0.625 ML

It could be shown that for increasing oxygen coverage, the activation energy of the oxygen decomposition increases (Figure 5.6) while the reaction gets less exothermic (Figure 5.7). Only for small initial oxygen coverages the activation energy decreases, suggesting a doping effect. For surface coverages above $\theta_{\text{INIT}} = 0.25$ the activation energy of the decomposition process increases almost exponentially.

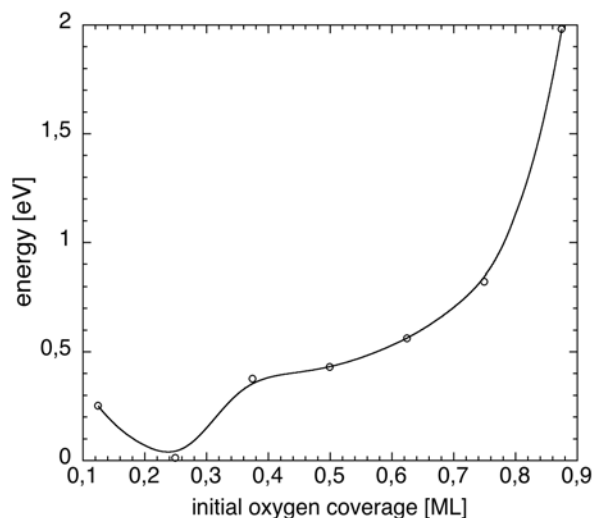


Figure 5.6: Activation energy of the oxygen decomposition as a function of the initial oxygen surface coverage

Furthermore, the heat of reaction of oxygen decomposition decreases with increasing initial coverage. At coverages close to a monolayer the reaction is even endothermic, see Figure 5.6*. This observation as well points towards a strong inhibition of the oxygen decomposition at medium initial oxygen coverages as already observed by TPD experiments [89].

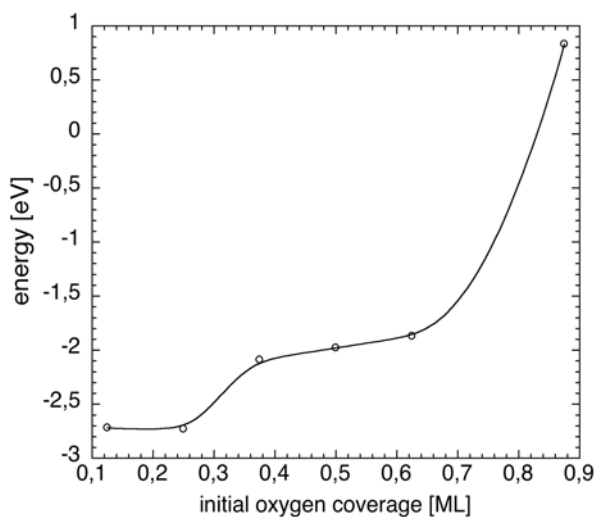


Figure 5.7: Coverage dependence of the reaction energies of the oxygen decomposition

* Preliminary calculations of the decomposition at high oxygen coverages using a 5-layer rhodium slab, support the results (E_a and $\Delta E_{\text{reaction}}$) found with the 3-layer rhodium slab. This indicates that the results are not an artifact of the model used.

To determine the origin of this effect, charge and geometry analysis of the transition states were carried out.

Analysis of the Transition State Geometries

Analysis of the geometry of the calculated transition states for the oxygen decomposition on Rh(111) surfaces shows that the position of the transition state depends on the oxygen preoccupation. The location of the transition state shifts in the reaction coordinate towards the product geometry. For clarity the transition states of the oxygen decomposition on (2 x 4)-Rh(111) without oxygen preoccupation ($\theta_{\text{INIT}} = 0.125$) and with different amounts of oxygen preoccupation ($\theta_{\text{INIT}} = 0.25 - 0.875$) are depicted in Figure 5.8.

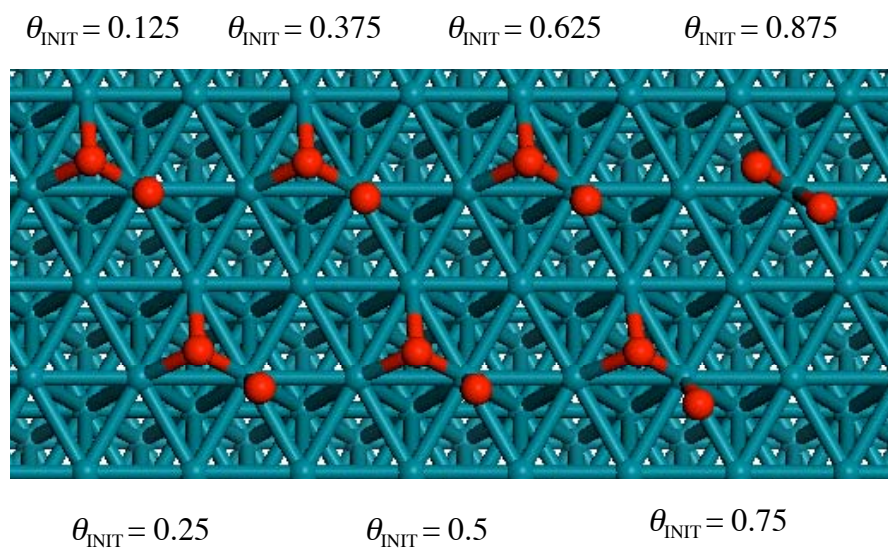


Figure 5.8: Transition states of the oxygen decomposition with increasing oxygen preoccupation. For the sake of clarity, the oxygen preoccupation is not shown.

The oxygen atoms in the transition state of the oxygen decomposition get closer to their positions in the product structures with increasing oxygen preoccupation. In the transition state for the oxygen decomposition leading to a complete monolayer of oxygen (see Figure 5.8, top right) the oxygen atoms are 192 pm apart, while they are rather close to their positions in the product structure (3-fold fcc as well as hcp). Thus, the transition states

calculated and heats of reactions obtained from these calculations are in good accordance with Hammond's postulate.

θ_{init}	lower O				upper O			$\epsilon(^{\circ})$	$\alpha(^{\circ})$ (O-Rh-O)
	distance to (pm)			$\epsilon(^{\circ})$	distance to (pm)				
	Rh ¹	Rh ²	Rh ³		Rh ³	Rh ⁴	Rh ⁵		
0.125	215	215	199	0.00	197	317	318	-0.58	51.6
0.250	217	213	199	0.97	193	308	300	2.48	56.3
0.375	218	212	197	1.57	193	315	307	2.83	53.4
0.500	220	213	197	1.66	192	301	299	3.54	55.2
0.625	220	222	197	-0.29	193	308	277	1.12	54.2
0.750	219	219	197	-0.23	200	296	259	11.91	52.9
0.875	249	253	199	-0.87	213	281	277	1.12	55.4

Table 5.2: Exact geometries of the different transition state structures. For atom numbering please see Figure 5.9. ϵ denotes the angle by which the oxygen atoms is tilted out of the surface normal plane (depicted in Figure 5.9, left), positive angle denotes tilting towards Rh² and Rh⁵, negative angle towards Rh¹ and Rh⁴; α denotes the angle between lower O, Rh³ and upper O (see Figure 5.9, right)

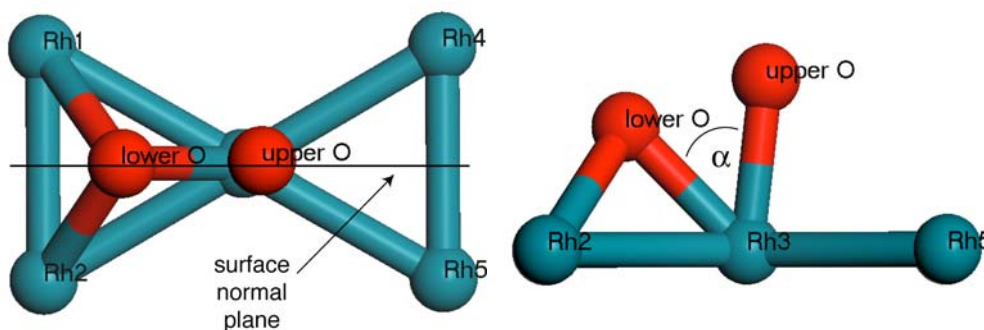


Figure 5.9: Example transition state with atom numbering, surface normal plane and oxygen-rhodium-oxygen angle α

Hammond's postulate states that the transition state of an exothermic reaction occurs early in the reaction coordinate (reactant-like transition state), while it occurs late in the reaction

coordinate for endothermic reactions (product-like transition state) [90]. The geometries of the different transition states are given in Table 5.2.

Mulliken Charge Analysis of the Transition State of the Oxygen Decomposition

Charge analysis of the transition states showed that at low oxygen coverage (0.25 ML) electron donation from the surface to the oxygen atoms is more pronounced than without oxygen preoccupation. This indicates a stabilisation of the transition state for 0.25 ML oxygen coverage and hence can explain the lowered activation barrier for the decomposition. For higher coverages the partial charges of the oxygen atoms decrease which indicates a destabilisation of the transition state. This leads to an increase of the activation energies calculated for surface coverages higher than 0.3 monolayers. As in the case of oxygen adsorption, also here, the shape of the graphs of the partial charges of the oxygen atoms and the graph of the activation energy are similar, indicating a direct correlation.

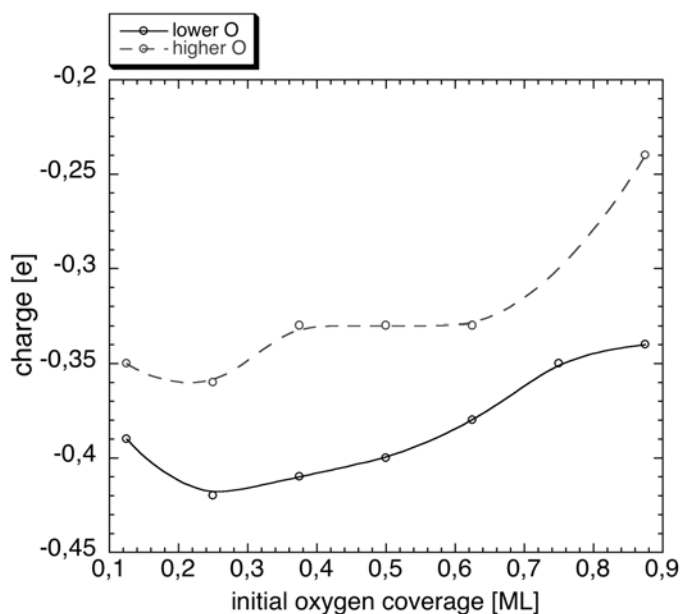


Figure 5.10: Mulliken charges of the oxygen atoms in the transition state of the oxygen decomposition. Lower oxygen refers to the oxygen atom bonded to the rhodium surface in the reactant structure.

5.3 Conclusions

DFT calculations show that oxygen coverage of the rhodium(111) surface weakens the bonding of the oxygen molecule to the rhodium surface. This surmises that with increasing oxygen coverage the adsorption probability of O₂ decreases. Oxygen decomposition therefore gets statistically more unlikely and, hence, the oxygen coverage stagnates. Moreover, the study shows that there is a stable end-on adsorbed molecular oxygen species on rhodium(111). However, the calculated energy barrier towards the decomposed oxygen is rather low, pointing towards a rather fast decomposition.

A minor extent of oxygen preoccupation on a rhodium surface even enhances the ability of rhodium to decompose molecular oxygen. However, at higher initial oxygen coverages, this ability is obstructed, supporting the suggestion that oxygen coverage stagnates. As can be seen in Figure 5.6, on the right hand side of the minimum for the activation energy at $\theta = 0.25$ the activation energy increases almost exponentially. Since the decomposition process is sterically unhindered (an unoccupied surface site next to the adsorbed oxygen molecule is kept vacant), this increase in activation energy is most likely due to the electron withdrawing effect of the oxygen. This hypothesis is supported by Mulliken charge analysis.

Moreover, the energy of reaction of the oxygen decomposition becomes smaller with increasing surface coverage. At high surface coverages ($\theta_{\text{INT}} = 0.875$) the decomposition reaction is even endothermic, which again points towards a stagnation of the oxygen decomposition at medium oxygen coverages. Transition state analysis supports the calculated decrease in exothermicity, because this decrease is in agreement with Hammond's postulate. All these theoretical results are in accordance with TPD experiments [89].

A comparison of the thermochemistry of the desorption and decomposition of the end-on adsorbed dioxygen species shows that the decomposition at medium coverage is thermochemically favoured. This indicates that the stagnation is kinetically controlled.

The conclusions drawn from this study support the surface mechanism proposed by Nakatsuji and co-workers [16]. The decrease in oxygen decomposition activity of rhodium surface with increasing oxygen coverage up to a stagnation of the process could explain the NO decomposition activity at high oxygen concentrations. Nitrogen oxide in a vast excess of oxygen could still decompose over rhodium even though the initial kinetics support the contrary, since the activation energies are coverage dependent. The oxygen decomposition is very likely at low coverages, while it becomes improbable for higher oxygen coverages.

Therefore, the NO_x decomposition activity of rhodium could be attributed to partially oxidised rhodium surfaces.

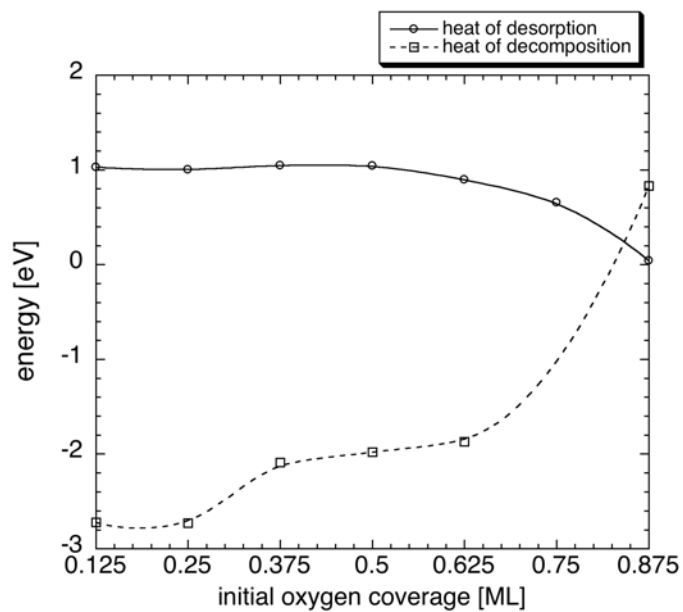


Figure 5.11: Comparison of the thermochemistry of dioxygen desorption and decomposition

To verify this assumption an analogue study for the NO decomposition on Rh(111) was carried out, see subsequent chapter.

Chapter 6: Coverage Dependence of the Nitrogen Oxide Decomposition

6.1 Motivation

In this chapter, DFT calculations performed in order to investigate the influence of oxygen preoccupation on the nitrogen oxide decomposition on rhodium, analogue to the study of the oxygen decomposition, are described. Besides investigating the coverage dependence of the adsorption energy of NO on the rhodium(111) facet, the influence of the initial oxygen coverage on the kinetics and thermodynamics of the nitrogen oxide decomposition reaction has to be studied. Furthermore, since NO is an odd electron molecule and, hence, possesses magnetic moment, the influence of spin effects on the absolute energy of the system was investigated.

If the coverage dependence found in case of the oxygen decomposition is inverted in case of nitrogen monoxide, this could possibly explain the mechanistic functioning of the catalytic system proposed by Nakatsuji. Deactivation of the oxygen decomposition with increasing oxygen coverage in combination with an activation of the nitrogen monoxide decomposition could be the causality for the DeNO_x activity of the studied exhaust-gas aftertreatment system.

6.2 Results and Discussion

6.2.1 Nitrogen Oxide on Rhodium(111)

A c(2x2) unit cell of a Rh(111) surface covered with 3 NO molecules ($\theta = 0.75$) was optimised using DFT-GGA calculations as explained before. LEED studies of a Rh(111) surface covered with 0.75 monolayers NO by Zasada *et al.* [75] found NO to form an ideal hexagonal overlayer with the two NOs arranged in 3-fold-position (fcc and hcp) and one in on-

top position. The results of the DFT optimisation of this $c(2 \times 2)$ -Rh(111) cell with 3 NO molecules adsorbed leads to exactly the same surface geometry as found by LEED. The calculated surface geometry is depicted in Figure 6.1.

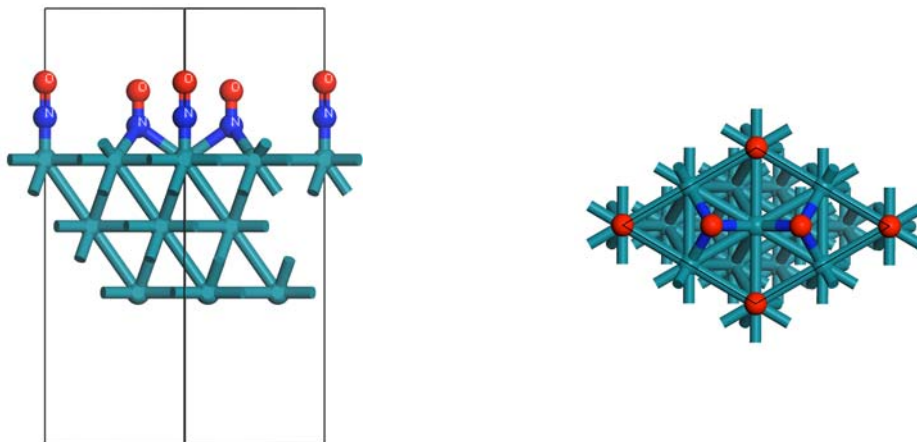


Figure 6.1: Front and top view of a $c(2 \times 2)$ -3NO on Rh(111)

All NO molecules are adsorbed perpendicular to the surface with the nitrogen atom pointing towards the surface. A comparison of distances and bond lengths between the DFT-GGA geometry optimisation and the LEED analysis (see Table 6.1) shows that the calculated values are well within the experimental error limits.

Even though the calculated values lie within the experimental error limits, it seems that the DFT calculations slightly overestimate the real values. To verify if this might be due to neglecting spin effects (NO is an odd electron molecule with a doublet ground-state), the calculations have been carried out spin-polarised. The spin-polarised DFT-GGSA calculation gave exactly the same distances as the regular unpolarised (DFT-GGA) calculation, implying that spin effects do not affect the geometry at all. For a direct comparison it is referred to Table 6.1. In a study performed by Loffreda *et al.* this spin-independence is proposed [91], but no explanation is given. Here this effect was investigated in more detail.

Distance (pm)	LEED	DFT-GGA	DFT-GGSA
3-fold			
N-surface	131 ± 7 (fcc)	136 (fcc)	136 (fcc)
	1.29 ± 0.07 (hcp)	1.35 (hcp)	1.35 (hcp)
N-O	115 ± 7	118	118
on-top			
N-O	113 ± 7	118	118
Rh-N	194 ± 8	184	184
surface interlayer spacing	228 ± 4	227	227

Table 6.1: Comparison between LEED data [75] and spin-polarised and unpolarised DFT-GGA-PW91 calculation

Magnetic Moment of NO Adsorbed on Rhodium(111)

In case of free NO, spin effects slightly affect the bonds length (123 pm without spin effect, 124 pm with spin effects). Therefore, the spin densities for both NO adsorbed on a rhodium(111) surface and NO located remotely (to debar electronic interaction) over a rhodium(111) surface were calculated. These calculations showed that as soon as the NO interacts with the surface, the electronic spin is diluted over the electron gas and hence the effect of the magnetic moment is so minor, that it does not affect the geometry at all.

In case of free NO, spin-polarised calculations have determined $\rho_{\text{spin}}^{\text{total}}$ and $\rho_{\text{spin}}^{\text{local}}$ to be 1, predicting the expected doublet state of NO. Upon adsorption of NO on the Rh (111) surface, the calculated total spin density $\rho_{\text{spin}}^{\text{total}}$ can be considered zero, while the local spin electron density $\rho_{\text{spin}}^{\text{local}}$ is 0.15. This indicates a weak anti-ferromagnetic state of the system.

A comparison of the spin density plot of the Rh(111) surface with the interacting and the non-interacting NO showed, that in case of remote NO a high spin density is located on the NO. The spin density exhibits the symmetry of the antibonding 2π orbital of NO in which the unpaired electron resides. The spin density plot of the interacting analogue showed that these high α -spin densities are not present here (no dark areas), while the regions with high β -spin densities (bright areas, third metal layer) vanish as well. This dilution of electronic spin over the electron gas structure leads to the same spin density as in the vacuum region above and

beneath the metal layer. Energies calculated utilising the spin-restricted and unrestricted GGA functional showed that the difference in calculated absolute energy is negligible (0.019 eV). The adsorption energies of NO were calculated to be 1.63 eV, unaffected by spin effects. Hence, there is no necessity to take spin effect into account in these calculations. The analogue plot of the electron density showed that the delocalisation of the unpaired electron does not affect the over-all electron density.

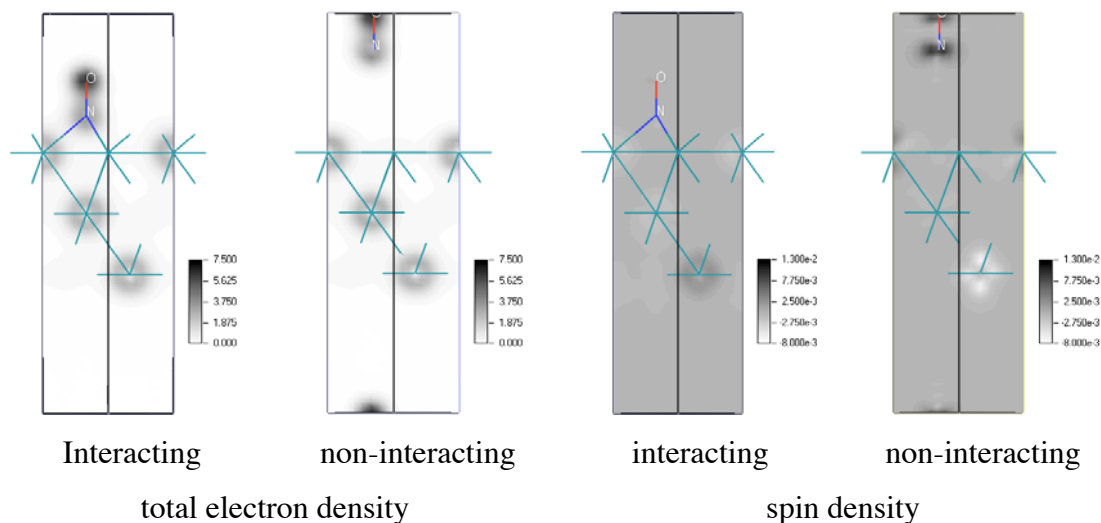


Figure 6.2: Spin density plots for nitrogen monoxide adsorbed and NO located remotely over a rhodium(111) surface

6.2.2 Oxygen Coverage Dependence of the NO Adsorption on Rhodium(111)

The dependence of the strength of the nitrogen monoxide bonding on the initial oxygen coverage of the rhodium surface has been studied by calculating the heat of adsorption as explained in Chapter 2. It could be shown that the bonding of nitrogen monoxide to the rhodium surface becomes weaker at high oxygen coverage, but remains energetically favourable. The heat of adsorption as a function of the initial surface coverage is depicted in Figure 6.3. It indicates that an oxygen preoccupation of the rhodium surface thermodynamically inhibits the adsorption of further nitrogen monoxide molecules on the surface. However, compared to the oxygen coverage dependence of the adsorption energy of oxygen, which is endothermic at high oxygen coverage (see Chapter 5), the nitrogen monoxide adsorption is still thermodynamically favoured over oxygen adsorption at any oxygen preoccupation. This result could support the mechanism proposed by Nakatsuji,

because the oxygen coverage would possibly remain constant at a certain value, while NO can still adsorb.

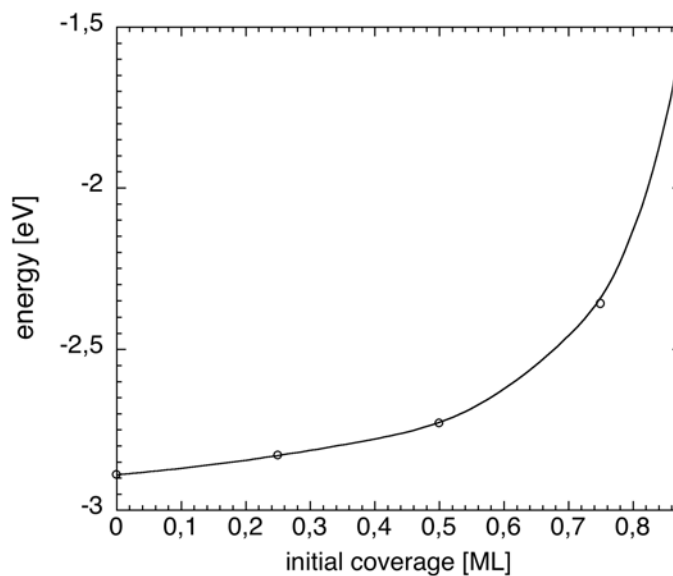


Figure 6.3: Heat of adsorption of NO as a function of the oxygen coverage

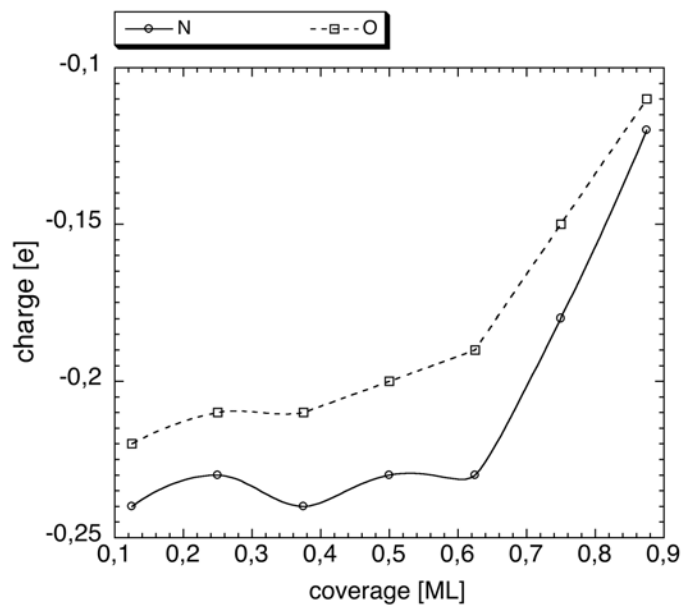


Figure 6.4: Mulliken charges as function of the surface coverage

Mulliken charge analysis of the end-on adsorbed NO species with different amounts of oxygen on the surface have been carried out. These analyses showed that the charge

transferred from the rhodium surface to the NO molecule decreases with increasing oxygen coverage (Figure 6.4), probably due to the electron-withdrawing effect of oxygen. The charges on the nitrogen and oxygen atom decrease strongly above 0.5 ML, analogously to the adsorption energy (Figure 6.4). These results support the assumption that the origin of this effect is electronic.

6.2.3 NO Decomposition over Rhodium(111) and Oxygen Influence

At a coverage of 0.25 monolayers NO on rhodium(111), the nitrogen monoxide molecule preferably resides in fcc three-fold position according to DFT-GGA structure optimisations (Figure 6.5, left). Moreover, as already explained, the presumption that end-on adsorbed diatomic molecules preferably decompose with the breaking bond coordinated over a single metal atom rather than coordinated over a surface metal-metal bond is well established [87]. Thus, owing to this and the principle of least atom sharing [88], a preferred final conformation of the dissociated molecule was assumed as depicted in Figure 6.5, right. The computed transition state for the decomposition is also depicted, and it can be seen that first the nitrogen-oxygen bond has to bend into the direction of the decomposing metal atom. In the transition state the nitrogen-oxygen bond is broken, while both atoms are bonded to the decomposing rhodium surface atom.

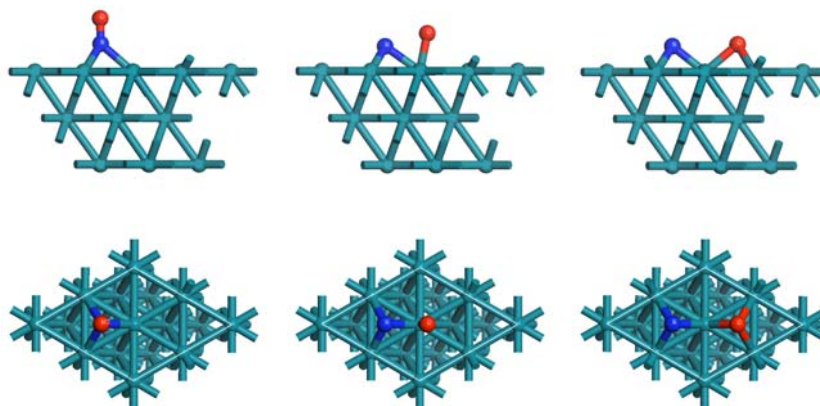


Figure 6.5: Adsorbed nitrogen oxide, decomposition transition state and decomposed nitrogen oxide on (2 x 2)-rhodium(111)

From the transition state the oxygen atom simply ‘drops’ into its preferred adsorption site. The activation energy for this surface reaction was calculated to be 2.24 eV with an energy of reaction of 0.32 eV.

After placing an additional oxygen atom (initial coverage $\theta = 0.5$, $\theta_{\text{O}} = 0.25$) on top of the rhodium surface, and recalculating the optimal geometries for starting material as well as the products, a determination of the transition state as described Chapter 2 showed that the additional oxygen inhibits further decomposition of NO molecules, even though the decomposition is still sterically unhindered. The activation energy increases to 2.41 eV with an energy of reaction of 0.46 eV.

To investigate this effect in more detail, a surface with a $c(2 \times 4)$ elementary cell consisting of 8 surface rhodium atoms has been modelled in order to vary the initial oxygen coverage over a broader range, analogue to the study carried out for oxygen (Chapter 5). The atomic coordinates of the metal atoms were constrained to conserve the (111) facet, while the adsorbates were assumed to be mobile. Only for high coverage ($\theta \geq 0.75$), constraints were imposed on the adsorbates, so that a vacant surface site adjacent to the nitrogen oxide molecule is available to ensure geometrically unhindered decomposition. The geometries for the nitrogen oxide molecule as well as its decomposition products have been calculated for different oxygen coverage. The transition state of the reaction of the molecule to its decomposition products was determined for different initial oxygen coverage. As an example, the transition state of the nitrogen oxide decomposition at an initial oxygen coverage of $\theta_{\text{O,INIT}} = 0.5$ is shown in Figure 6.6. The activation energies as well as the reaction energies have been calculated as explained in Chapter 2.

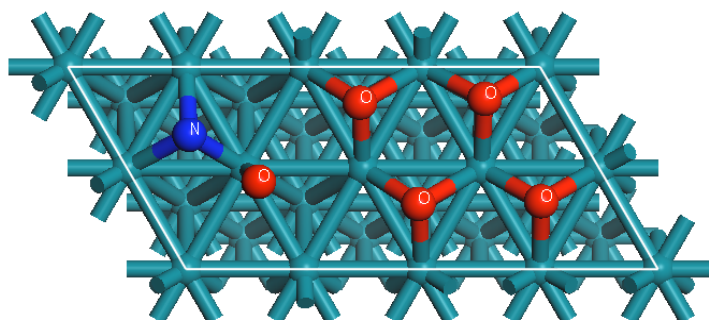


Figure 6.6: The transition state of the NO decomposition at an initial oxygen coverage of 0.5 ML

It was observed that for increasing oxygen coverage, the activation energy of the nitrogen oxide decomposition increases (Figure 6.7), while the reaction gets more endothermic (Figure 6.8). For surface coverages below an initial oxygen coverage of 0.5 monolayers, the activation energy increases linearly, while it increases almost exponentially above $\theta_o = 0.5$. The calculated over-all reaction* energy of 2.47 eV at 0.25 ML is in close agreement with the value calculated by Loffreda *et al.* (2.5 eV) [91]. However, the endothermicity of the dissociation step is clearly in contrast to calculations carried out before [92]. A recalculation of the optimal adsorption geometries and the corresponding energies for NO and its dissociation products on a (2 x 2) elementary cell with the uppermost metal layer allowed to relax, leads as well to an endothermicity of the reaction. An analogue study utilising the spin-restricted functional also calculated the reaction to be endothermic.

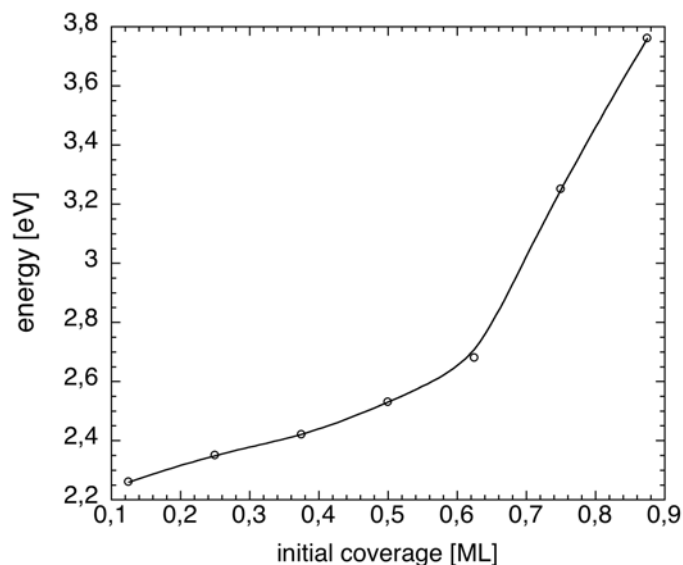


Figure 6.7: Activation energy of the NO decomposition as a function of the initial surface coverage:

This inhibition might be due to the electron withdrawing effect of the adsorbed oxygen. The electronegative oxygen withdraws electrons from the metal surface and hence lowers the back-donation effect of the metal into the antibonding orbital of the end-on adsorbed nitrogen monoxide. This effect is hindered when oxygen withdraws electrons from the metal atom. The weaker backdonation effect can also be observed in the N-O bond length of the adsorbed NO. It decreases from 123 pm ($\theta = 0.125$) to 119 pm ($\theta = 1$), indicating a higher bond order of the adsorbed molecule.

* Reaction of gas-phase NO to N and O co-adsorbed on Rh(111)

To verify if electronic effects are also responsible for the increase in activation energy (destabilisation of the transition state), Mulliken charge analysis was carried out for the calculated transition states. In Figure 6.9, the Mulliken charges are presented as a function of the initial surface coverage. It can be seen that the amount of electronic charge transferred to the transition state structure decreases with increasing surface coverage. This indicates a destabilisation of the transition state, which would explain the increase of the activation energy observed.

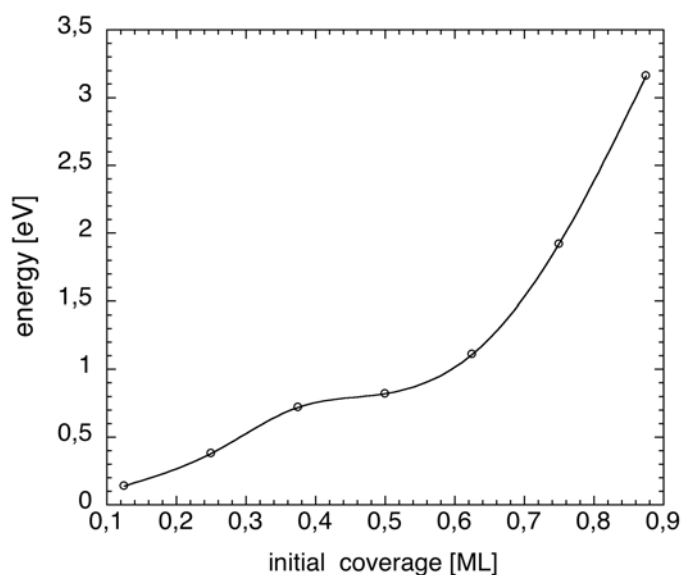


Figure 6.8: Coverage dependence of the reaction energies of the NO decomposition

As in case of oxygen, this inhibition might be due to the electron-withdrawing effect of the adsorbed oxygen. The electronegative oxygen withdraws electrons from the metal surface and, hence, lowers the back-donation effect of the metal into the antibonding π -orbital of the end-on adsorbed nitrogen monoxide. This effect is hindered when oxygen withdraws electrons from the metal atom. The weaker backdonation effect can also be observed in the N-O bond length of the adsorbed NO. It decreases from 123 pm ($\theta = 0.125$) to 119 pm ($\theta = 1$), indicating a higher bond order.

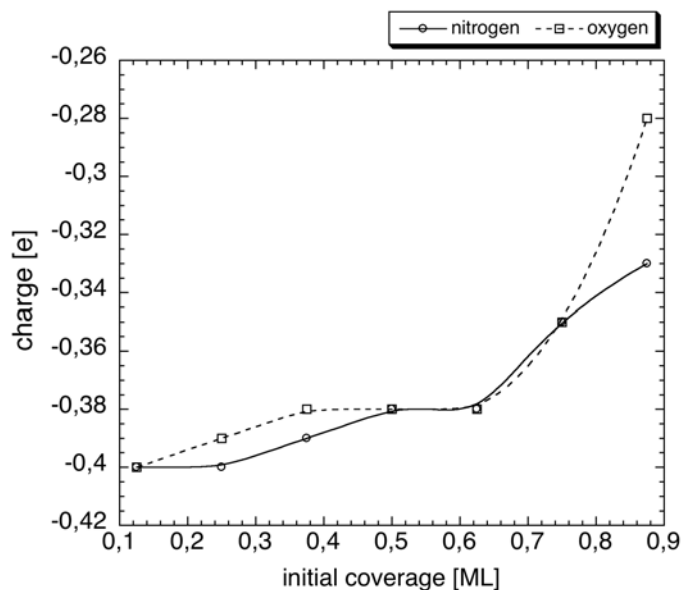


Figure 6.9: Mulliken charges of the transition state of the NO decomposition as function of the initial surface coverage

Furthermore, the heat of formation of the atomic nitrogen and oxygen species decreases with increasing initial coverage. This observation suggests that the capability of rhodium to decompose nitrogen oxide in a vast excess of oxygen is not due to an acceleration by oxygen adsorbed prior to NO decomposition.

θ_{init}	$d_{\text{N-Rh}}[\text{pm}]$			N $\varepsilon(^{\circ})$	$d_{\text{O-Rh}}[\text{pm}]$			O $\varepsilon(^{\circ})$	$d_{\text{N-O}}[\text{pm}]$	N-O $\alpha(^{\circ})$
	Rh ¹	Rh ²	Rh ³		Rh ³	Rh ⁴	Rh ⁵			
0.125	198	211	199	2.90	200	299	316	5.70	199	59.9
0.250	201	199	201	-2.30	196	303	298	-1.60	206	62.4
0.375	201	197	202	0.77	242	355	345	2.80	211	55.9
0.500	207	195	203	1.10	242	355	345	-3.30	212	56.0
0.625	198	202	192	0.80	195	306	295	-3.50	203	63.4
0.750	190	204	198	2.90	196	299	320	7.30	203	59.8
0.875	203	209	194	1.40	197	308	296	-3.50	198	61.0

Table 6.2: Exact geometries of the different transition state structures. ε denotes the angle by which the atoms are tilted out of the surface normal plane, positive angle denotes tilting towards Rh² and Rh⁵, negative angle towards Rh¹ and Rh⁴; α denotes the angle between nitrogen, Rh³ and oxygen. For atom numbering please see Figure 6.10.

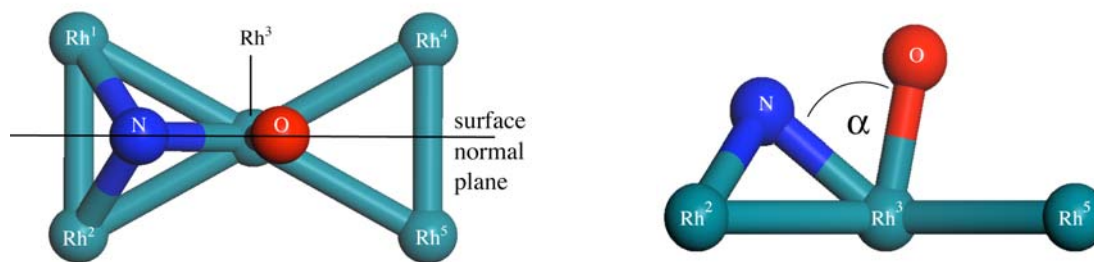


Figure 6.10: Example transition state with atom numbering, surface normal plane and nitrogen-rhodium-oxygen angle α

6.3 Conclusions

DFT-GGA structure optimisations carried out in this study are able to predict the geometry of adsorbants on Rh(111) accurately. These *ab-initio* calculations support the assumption that spin effects do not affect the optimal geometry and energy of NO adsorbed on rhodium(111). Spin-restricted calculations show that, upon adsorption, NO loses its spin density, while it induces a negligible magnetic moment onto the rhodium(111) surface. Hence, further calculations could be carried out with a spin unrestricted GGA functional, leading to a significant acceleration, especially for the calculations of potential energy hypersurfaces.

These spin-unrestricted calculations show that initial oxygen coverage of the rhodium(111) surface weakens the bonding of nitrogen oxide to the rhodium surface. This surmises that with increasing oxygen coverage the adsorption probability of NO decreases, because it becomes thermodynamically more unfavourable. However, the thermodynamic inhibition of the oxygen adsorption is more distinct [93].

Oxygen preoccupation on a rhodium surface abates the ability of rhodium to decompose nitrogen oxide. Since the decomposition process is sterically unhindered (an unoccupied surface site next to the adsorbed oxygen molecule is kept vacant), this increase in activation energy must be due to the electron withdrawing effect of the oxygen. The heat of formation of the atomic species is slightly endothermic (0.15 eV) when NO decomposes on a rhodium(111) surface without oxygen preoccupation (corresponding to 0.125 ML). However, with increasing oxygen preoccupation the reaction becomes even more endothermic. These

results are in contrast to previous calculations that calculate the decomposition to be exothermic [92].

A comparison of the thermochemistry of desorption and decomposition shows that the decomposition is energetically favoured up to 0.75 ML, Figure 6.11.

Root *et al.* observed that from 0.3 ML pure NO coverage on, not all NO decomposes but preferably desorbs during heating [94]. Considering the fact that, owing to the decomposition, the surface coverage increases, this is well in agreement with the results found here.

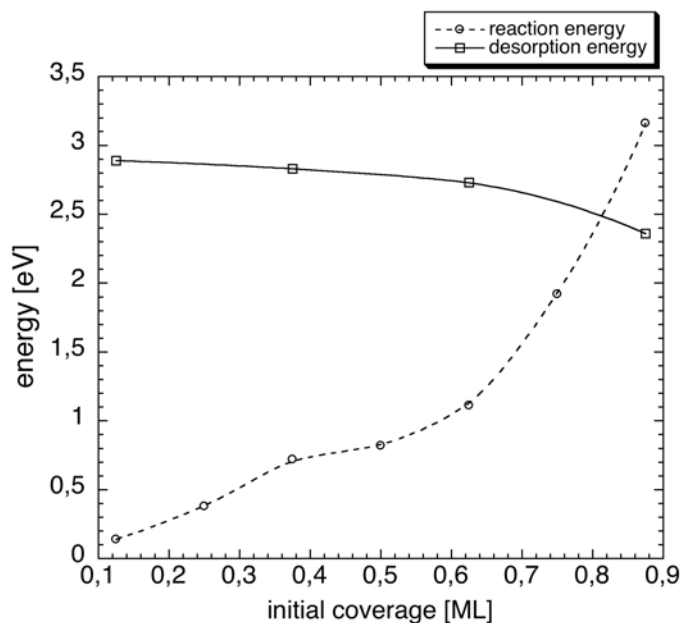


Figure 6.11: Thermochemistry of NO desorption and decomposition (as function of the initial coverage,

The overall conclusions drawn from this study do not support the surface mechanism proposed by Nakatsuji and co-workers [16]. The decrease in NO decomposition activity of the rhodium surface with increasing oxygen coverage points towards a stagnation. The activation energy for the NO decomposition is higher than the activation energy of the oxygen dissociation at any initial oxygen preoccupation and, hence, the oxygen dissociation will be more likely at any oxygen preoccupation, see Figure 6.12. Although oxygen can decompose in more than one way on Rh(111), *e.g.*, direct dissociative decomposition, the activation barrier for this process will be even lower than that of the end-on O₂.

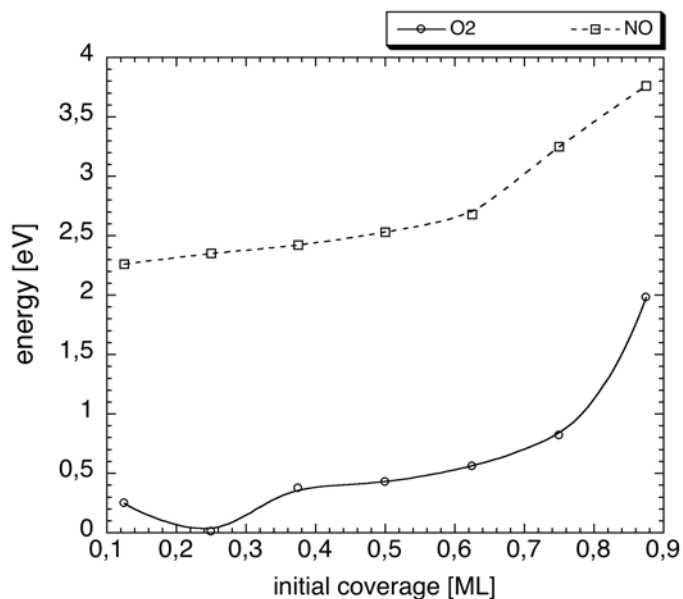


Figure 6.12: Activation energies of the oxygen and nitrogen monoxide decomposition as function of the initial coverage.

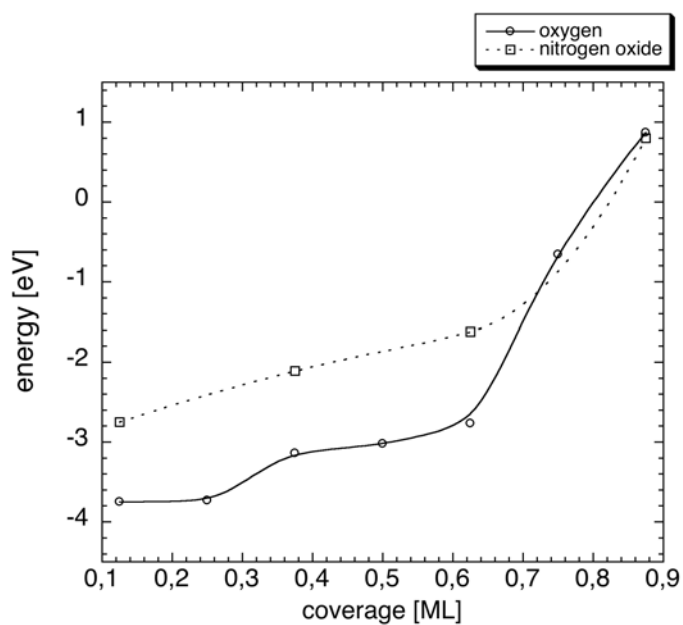


Figure 6.13: Comparison of the thermochemistry of the dissociation of free NO and free O₂ on rhodium(111)

A comparison of the thermochemistry of oxygen and nitrogen oxide dissociation from the free molecules (Figure 6.13) shows that also thermochemically the oxygen dissociation is more favourable than the nitrogen oxide dissociation. Only at high initial coverages the

decomposition reactions are energetically equivalent. This also indicates that oxygen preoccupation does not direct the surface chemistry towards the decomposition of nitrogen oxides. Hence, the surface chemistry of the catalytic system proposed by Nakatsuji remains unclear.

Nevertheless, it is known that many surface reactions preferably occur on surface defects such as steps. In order to verify if the nitrogen oxide dissociation is more likely at these sites and possibly enhanced by coadsorbants, this process was studied at the (311) facet of rhodium (Chapter 9).

Chapter 7: Surface Diffusion on Rhodium(111)

7.1 Motivation

As discussed in the previous chapters, the decomposition probabilities of nitrogen oxide and oxygen have to be understood to predict the over-all conversions of pollutants in the automotive catalytic converter. Additionally, the mobility of all species on the rhodium surface have to be clarified. Since a minor amount of NO in a vast excess of oxygen is decomposing over rhodium, it is statistically highly unlikely that two nitrogen atoms adjoin each other. Hence, molecular nitrogen can only be formed via the Burch mechanism [95] when atomic nitrogen species diffuse towards each other.

In order to achieve a detailed insight into the surface diffusion, the process was simulated by means of DFT calculations. The surface diffusion was simulated by determining the potential energy surface for a single-site jump between two 3-fold positions, fcc to hcp, and the converse. A rhodium surface was modelled by generating a two layer metal slab with infinite expansion.

7.2 Results and Discussion

7.2.1 Diffusion of Atomic Species

a Nitrogen

For a pure atomic nitrogen layer on rhodium(111), LEED studies report only diffuse patterns [96]. Therefore, no exact comparison to experimentally determined structures can be given here. According to our calculations, atomic nitrogen preferably resides in 3-fold fcc position,

117 pm above the surface plane with a Rh-N bond lengths of 198 pm and 190 pm. The difference in bond length to the surface rhodium atoms is due to the different rhodium atoms in the (2 x 1) overlayer. The elementary cell consists of 2 surface rhodium atoms, which are chemically different. One of them is shared by the successive nitrogen overlayer (it is coordinated to 2 adsorbed nitrogen atoms), the other is only coordinated to one nitrogen atom. This can most conveniently be seen when the elementary cell is expanded to a (4 x 4) unit cell with an analogous overlayer (Figure 7.1). Surface metal atoms that are coordinated to more than one adsorbant are hereafter referred to as shared rhodium. The nitrogen adsorption properties for the hcp position are analogue; the bonds to shared surface atoms are slightly longer (198 pm) in comparison to the non-shared (190 pm).

Calculation of the PES for the single-site jump of atomic nitrogen from the fcc position to an adjacent hcp position determined the transition state to be located at the bridged position between the two 3-fold positions. The activation energy for the single-site jump was calculated to be 1.02 eV with an energy of transformation of 0.01 eV. The back-transformation, the single-site jump from the hcp to the fcc position, requires an activation energy of 1.01 eV and is slightly endothermic with -0.01 eV.

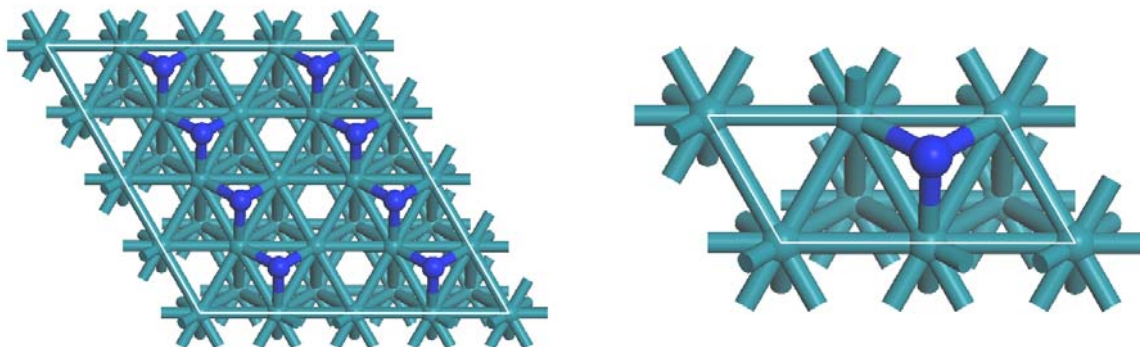


Figure 7.1: Rh(111)-(4 x 4) and (2 x 1) covered with 0.5 ML atomic nitrogen

b Oxygen

In Chapter 4, it was shown that the results of DFT-GGA geometry optimisations of atomic oxygen accurately resemble the structures determined by LEED analysis. Rhodium-oxygen bond length as well as the oxygen surface distance of the (2 x 1) oxygen overlayer on rhodium(111) are only slightly different from those of oxygen in the (2 x 2) overlayer (in both

cases $\theta = 0.5$: (2 x 2) O-Rh: 197 pm, 201 pm (shared); (2 x 1) O-Rh 202 pm (all shared)). The oxygen atom is located 124 pm above the surface plane in both cases, in accordance with results published by Nørskov and co-workers (123 pm). Therefore, the optimised structures for the (2 x 1) oxygen overlayer on rhodium(111) were assumed to be correct as well.

Calculation of the potential energy surface of the transition between the different 3-fold positions located the transition state to be in the bridged position, analogously to atomic nitrogen. The activation energy of the single-site jump from the fcc- to the hcp-3-fold position was calculated to be 0.58 eV with an energy of transition of -0.3 eV. The back-transformation (hcp- to fcc-3-fold position) in turn requires an activation energy of 0.87 eV with an energy of transition of 0.3 eV.

c Carbon

Adsorption of atomic carbon is most likely to occur in 3-fold hollow sites with preference to the fcc site, which is 0.18 eV more stable than the hcp site. The carbon atom is located 114 pm above the surface, with Rh-C distances of 186 pm and 195 pm (shared). The calculated potential energy surface for the transition to the less stable hcp position determines the activation energy to be 0.82 eV. The back-transformation is activated by 0.65 eV. These results are in agreement with other DFT calculations [92]. Experimental data for this system are not available.

d Sulphur

Atomic sulphur was calculated to be most stable in a 3-fold fcc position in agreement with normal incidence x-ray standing wave field (NIXSW) absorption and surface-extended X-ray absorption fine structure (SEXAFS) results [97]. The optimal position for atomic sulphur was calculated to be 167 pm above the rhodium(111) plane, in accordance with the experimental value of $173 \text{ pm} \pm 5 \text{ pm}$. Also the calculated rhodium-sulphur bond length of 223 pm is in good agreement with the experimentally determined value $225 \text{ pm} \pm 4 \text{ pm}$. These distances do not seem to change with the surface coverage according to our simulations. Again, as soon as sulphur atoms are coordinated to shared rhodium atoms, they are displaced from the optimal 3-fold position, an observation that is supported by LEED analysis [98]. The rhodium-sulphur bond of the rhodium atom that is bonded to more than one sulphur atoms prolongs to 229 pm

[98]. If the sulphur atom is placed, in a 3-fold hcp position, the bond length increases slightly to 225 pm compared to 229 pm for shared Rhodium atoms.

Calculation of the potential energy surface of the transition between the different 3-fold positions located the transition state to be in the bridged position, analogously to the other atomic species. The activation energy for the transformation to the less stable hcp-3-fold position was calculated to be 0.74 eV with an energy of transition of 0.13 eV. The back-transformation requires an activation energy of 0.6 eV with an energy of transition of -0.13 eV.

e Hydrogen

The preferential adsorption site for atomic hydrogen on Rh(111) according to DFT-GGA calculations is the fcc-3-fold position. The fcc position is 0.06 eV more stable according to the calculations. This is in agreement with high-resolution electron-energy-loss spectroscopy (HREELS) measurements [99] and with other theoretical studies [92]. The single-site jump activation energy from the preferred fcc- to the adjacent hcp-3-fold position was calculated to be 0.07 eV. The back transformation to the energetically favourable fcc position was calculated to be 0.13 eV. This is in close agreement with laser-induced thermal desorption (LITD) measurements that indicate a diffusion barrier of 0.14 eV [99] as well as prior theoretical studies, which calculated it to be 0.1 eV using different functionals (PW91, PRBE) [92].

The structure of the different threefold adsorption sites of the atomic species and the transition state of the transformation into one another are depicted in Figure 7.2.

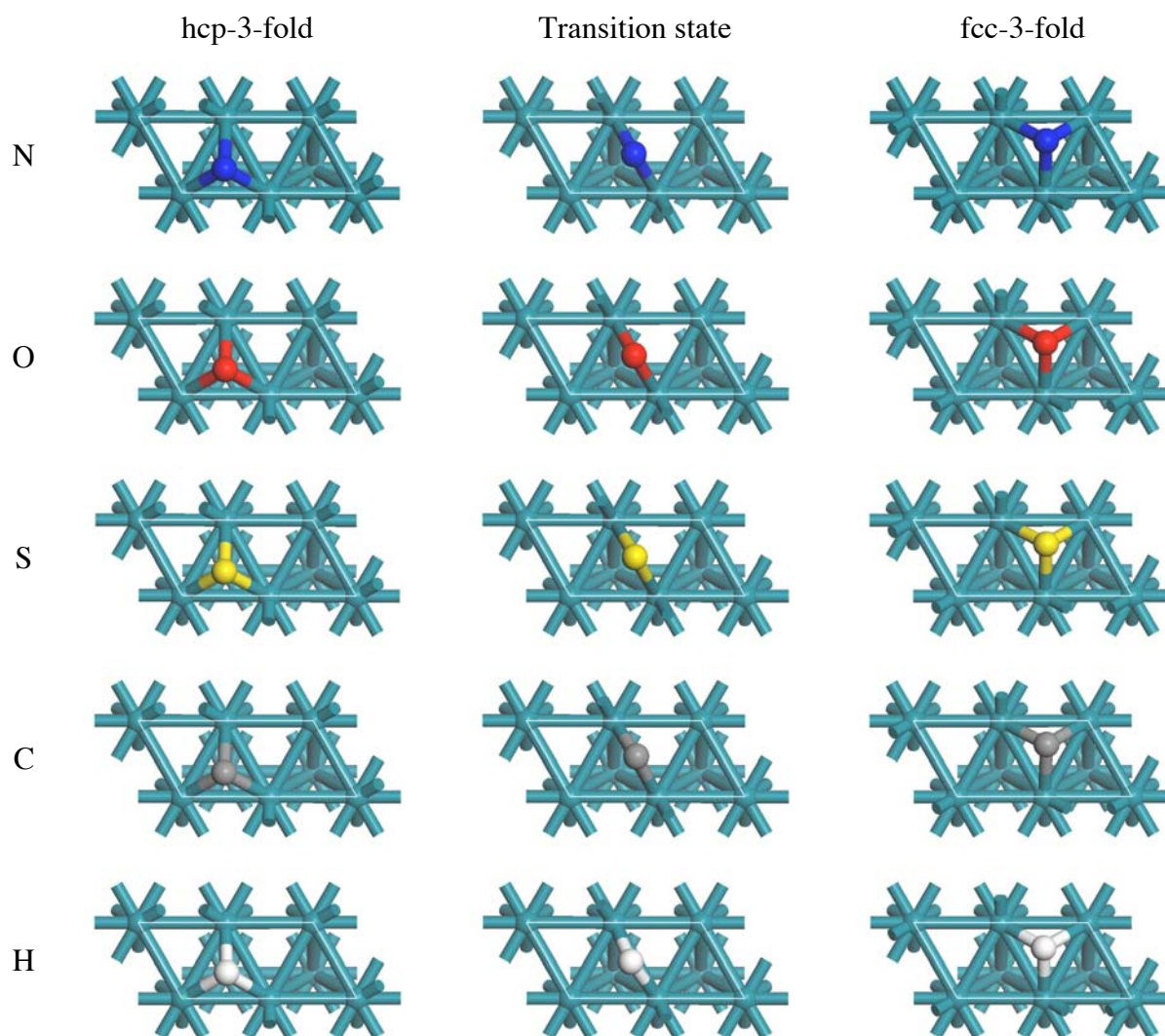


Figure 7.2: Single-site jump of atomic species on Rh(111)

7.2.2 Diffusion of Molecular Species

a Carbon Monoxide

As shown in Chapter 3, DFT-GGA calculations predict the optimal geometry of carbon monoxide on rhodium(111) very well. In case of the (2 x 1) overlayer the optimal geometry does not differ much from the optimal geometry calculated for the (2 x 2) overlayer (distances (pm): Rh-C: 212 (2x2) - 210 (2x1), C-O: 118 (2x2)- 118 (2x1)). Therefore, the geometrical prediction of the overlayer studied here can be assumed to be correct as well.

The activation energy of the single-site jump from fcc-3-fold position to the adjacent hcp-3-fold position was calculated to be 0.02 eV. The transition was found to be slightly exothermic with an energy of transition of -0.04 eV. The energy required to enable this transformation was calculated to be 0.06 eV. As assumed, the molecular surface species appears to be much more mobile than the atomic surface species discussed before.

b Nitrogen Monoxide

The optimal geometry of NO on the (111) facet of rhodium can be predicted well using DFT-GGA optimisation as shown in Chapter 6. As in the (2 x 2) overlayer, nitrous oxide prefers the fcc-3-fold position. The bond length of NO in a (2 x 1) overlayer differs only slightly from those on the (2 x 2) overlayer ((2 x 1): Rh-N 203 pm (205 pm, shared), N-O; (2 x 2): Rh-N 207 pm, N-O 122 pm). Hence, it can be assumed that the found optimal geometries for the (2 x 1) overlayer are also accurate. Determining the position of the transition state of the surface transformation from the fcc- to the hcp-3-fold position leads again to a bridged species. Calculating the reaction energies of the surface transformation determine the activation energy from fcc to hcp-3-fold position to be 0.34 eV and the energy of transition to be 0.01 eV. The back-transformation requires an activation energy of 0.34 eV and is slightly endothermic (-0.01 eV). Again, the molecular species appears to be more mobile on the (111) rhodium facet than atomic species.

The structure of the different threefold adsorption sites of the molecular species and the transition state of the transformation into one another are depicted in Figure 7.3.

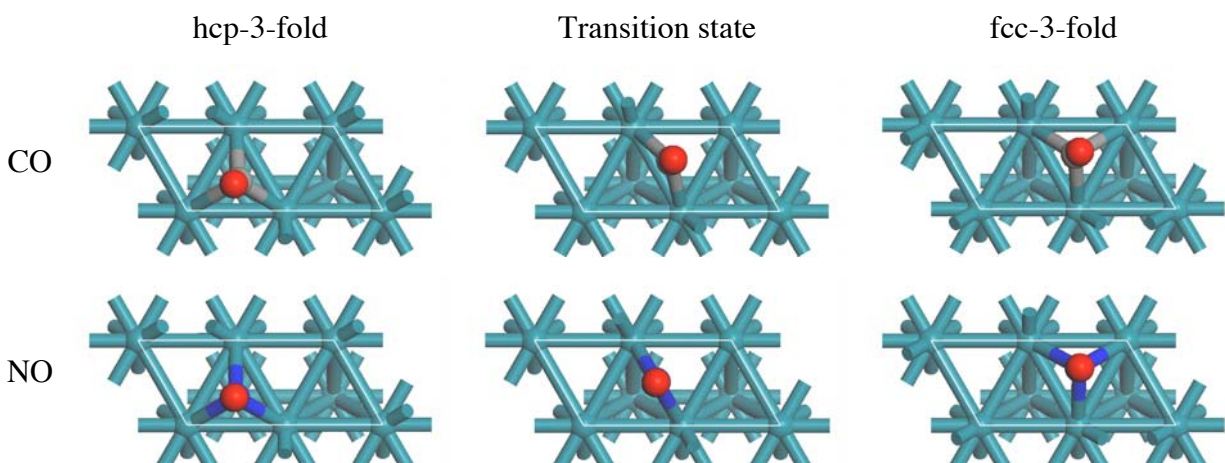


Figure 7.3: Single-site jump of molecular species on Rh(111)

7.2.3 Overview

As an overview, the reaction energies of the single-site jump of the different atomic and molecular species are given in Table 7.1.

Single-site Jumps		E_a	energy	E_a	energy
		hcp \rightarrow fcc	of transition	fcc \rightarrow hcp	of transition
atomic species	N	1.01 eV	-0.1 eV	1.02 eV	0.01 eV
	O	0.87 eV	0.30 eV	0.58 eV	-0.30 eV
	S	0.60 eV	-0.13 eV	0.73 eV	0.13 eV
	C	0.65 eV	-0.18 eV	0.83 eV	0.18 eV
	H	0.07 eV	-0.06 eV	0.13 eV	0.06 eV
molecular species	CO	0.06 eV	0.04 eV	0.02 eV	-0.04 eV
	NO	0.35 eV	0.01 eV	0.34 eV	-0.01 eV

Table 7.1: Activation energies and energies of transition for single-site jumps of atomic and molecular species on Rh(111)

7.2.4 Coverage Dependence of the Oxygen Single-site Jump

In order to learn more about the microscopic details of the behaviour of oxygen on rhodium(111), the single-site jump of oxygen was recalculated for different coverages. The potential energy surface of the single-site jump was determined for oxygen coverages of 0.5 ML (O-(1x2)-Rh(111)) as well as 0.25 ML (O-(2x2)-Rh(111)). As in case of the decomposition (see Chapters 5 and 6) reactions, the surface diffusion seems to be coverage-dependent.

The activation energy of the surface jump process is calculated to be 0.47 eV at 0.25 ML, while 0.57 eV at 0.5 ML. In both cases it is endothermic, with an energy change of 0.08 eV and 0.1 eV for 0.25 ML and 0.5 ML respectively. The results for the diffusion of oxygen on

the 3-layer (2x2)-Rh(111) at 0.25 ML coverage are close to previous calculations carried out by Mavrikakis *et al.* ($E_a=0.45$ eV, $E_{\text{trans}}=0.03$ eV).

Analysis of the transition state geometry shows that the calculated thermodynamic and kinetic data are in accordance with Hammond's postulate [90] (see Chapters 5 & 6), since the transition state of the stronger endothermic reaction (Figure 7.4, dark grey atom) is located later along the reaction coordinate (Figure 7.4, white arrow) than the more exothermic (Figure 7.4, light grey atom).

Furthermore, Mulliken charge analysis of the transition states was carried out to verify if the origin of the increase of the activation barrier is electronic. The partial charge of the oxygen atom in the transition state is -0.51 e in case of 0.25 ML, while it is only -0.47 e in case of 0.5 ML. This indicates a stronger stabilisation of the transition state in the case of the lower coverage and, hence, supports the assumption that the origin of the investigated effect is indeed electronic.

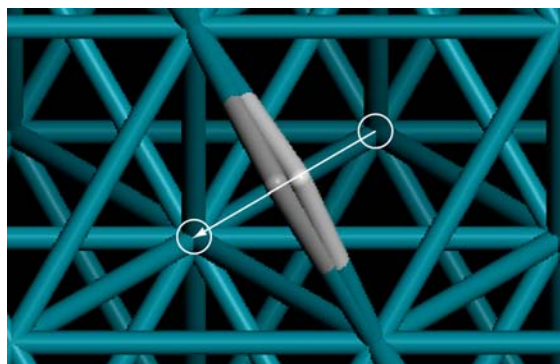


Figure 7.4: Top view of the transition states of an oxygen single-site jump at different coverages on rhodium(111) from a fcc- to a hcp-3-fold position (white circles) along the reaction coordinate (white arrow). Transition states of this process for coverages of 0.25 ML (light grey) and 0.5 ML (dark grey) are depicted.

7.3 Conclusions

The calculated energies for the surface transition processes indicate that atomic species exhibit a much lower surface mobility than molecular species. These results do not support the mechanism proposed by Nakatsuji [15, 16], which suggests that NO decomposes simultaneously with oxygen on the rhodium surface. As a minor amount of NO in a vast excess of oxygen is considered and kinetic measurements find oxygen to decompose much

faster than NO, it is statistically very unlikely that two nitrogen atoms adjoin each other. This in turn means that atomic nitrogen would have to diffuse on the surface to combine with another nitrogen to form N₂. Based on the knowledge gained from this study, this is very unlikely either, since atomic nitrogen is rather immobile on rhodium(111), owing to the rather high activation energy for a single-site jump. Furthermore, in the real catalytic system it would have to diffuse through other adsorbant, mainly oxygen. First calculations indicate that oxygen is even more immobile at higher coverage, making this recombination process even more unlikely.

These results are of course specific for the low-index (111) plane. To investigate if this is different at steps, the studies were extended to stepped surfaces. Furthermore, alternative pathways, such as a direct reaction between CO and NO or reaction via a dimeric NO species, have to be considered.

Chapter 8: Nitrogen Monoxide Dissociation on Stepped Surfaces

8.1 Motivation

According to DFT calculations of the NO dissociation on the (111) low-index plane of rhodium, the process has a rather high activation barrier and is endothermic. Nevertheless, experimental data state that clean rhodium – also low index planes as the investigated (111) facet – is initially able to decompose NO. For various metal surfaces and surface reactions it is known that they preferably occur at steps or defects of surfaces. To decide if the discrepancy between our calculations and experimental results might be due to imperfections of the surfaces used in experimental studies, the NO dissociation at a stepped surfaces (Rh(311)) was investigated. Furthermore, the influence of co-adsorbants at an adjacent surface site was investigated, in order to examine the dependence of the activation barrier on the co-adsorbant.

8.2 Results and Discussion

8.2.1 Rhodium(311) Plane

The Rh(311) plane is a vicinal hybrid of a (100) and a (111) facet. The (311) surface can also be described as 2(100) x (111). This means the surface plane cuts two atom layers in the (100) direction and then one atom layer in the direction of the (111) plane¹⁰. Owing to the steps the

¹⁰ Nota bene: The 2(100) x (111) surface could also be described as 2(111) x (100) if the turning point layer (see Figure 8.1) is considered to be part of the (111) facet.

metal atoms in the top layer are undercoordinated. Hence, the chemical behaviour of these atoms will differ strongly from those incorporated in the bulk. Therefore, the slab thickness for these calculations was chosen to be 6 metal atom layers, and the 2 uppermost layers were relaxed in an optimisation prior to subsequent investigations. This ensures that the surface is not in a chemically activated state.

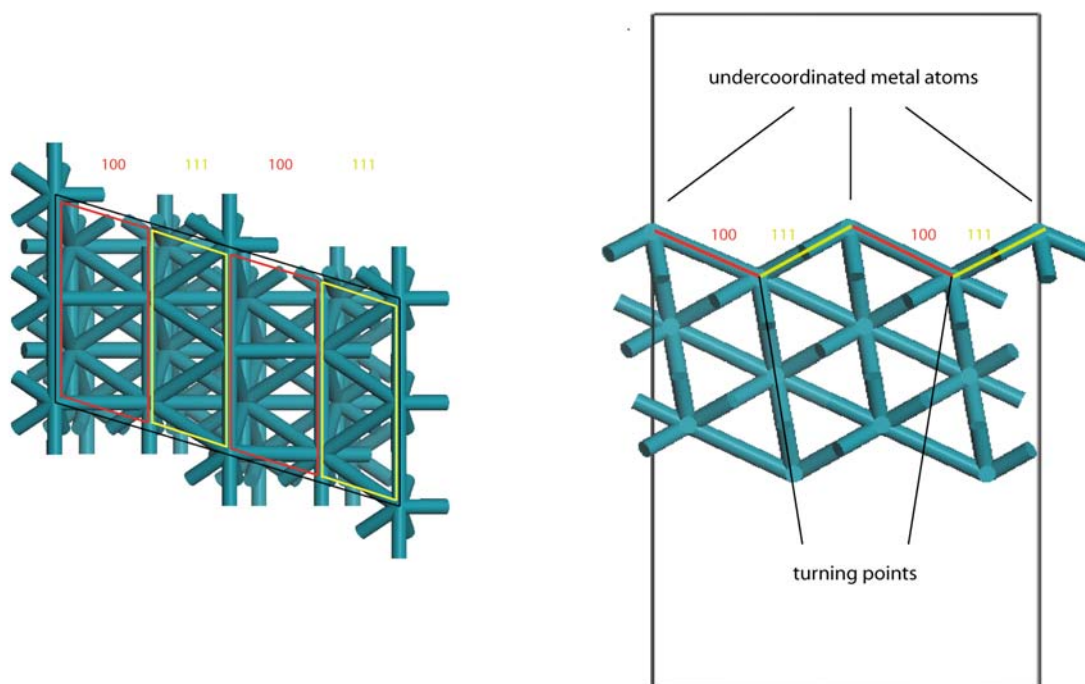


Figure 8.1: Front and top view of a Rh(311) surface

8.2.2 NO Dissociation on Rhodium(311)

Calculations found the NO to be most stable on the step coordinated in a 3-fold position of the (111) plane perpendicular to it. The most likely adsorption geometry of atomic oxygen after decomposition was determined to be in bridged position of the (100) plane (see Figure 8.2), while atomic nitrogen stays in the 3-fold position of the (111) plane. The nitrogen in the product is slightly closer to the (111) plane, indicating that it is stronger bound to the surface. Furthermore, it is known that atomic oxygen on Rh(100) is most strongly bound in the bridged position.

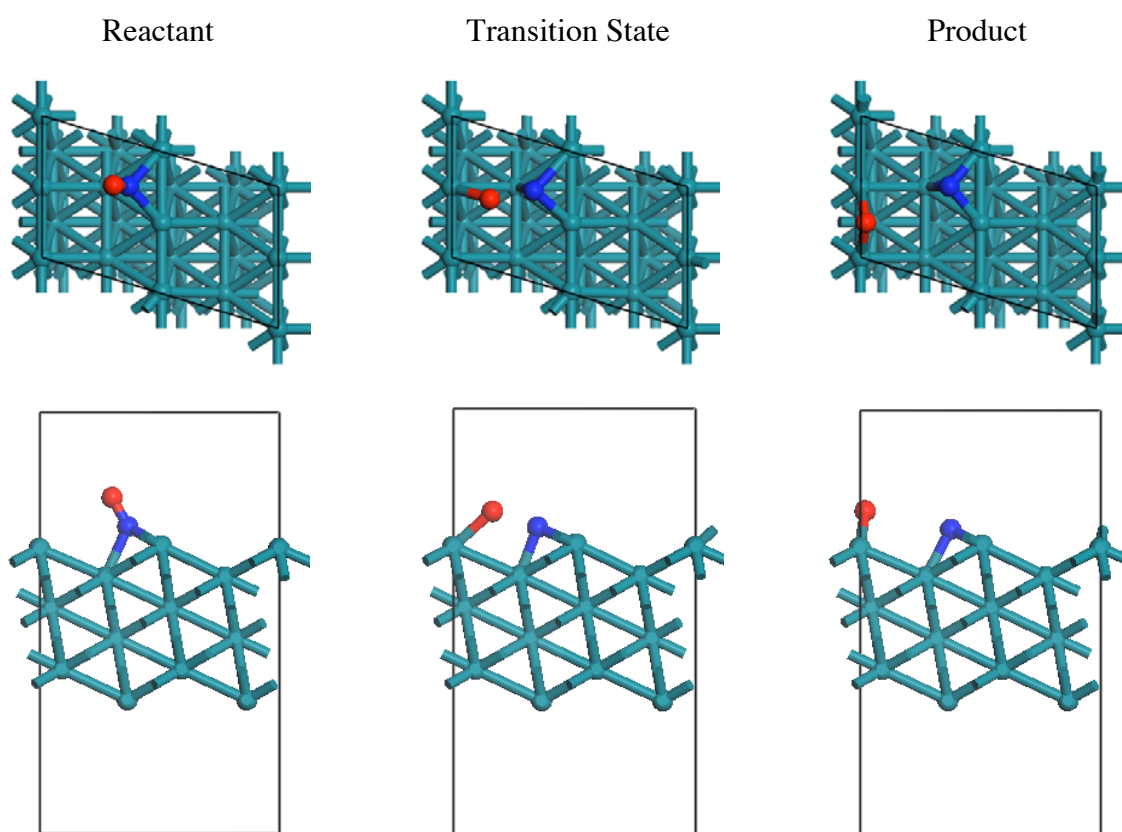


Figure 8.2: Nitrogen monoxide dissociation on rhodium(311)

A calculation of the potential energy surface for this dissociation supports this assumption. The reaction is calculated to be exothermic with a reaction energy of -0.52 eV.

The transition state is located to be at 0.49 of the reaction coordinate in which zero denotes the reactant and unity the product geometry. The oxygen is bound to the closer rhodium atom of the bridged species in the transition state, see Figure 8.2 middle. From the transition state, the maximum energy point on the reaction coordinate, the oxygen moves directly into the bridged position, energetically downhill. The activation energy is calculated to be 1.50 eV, considerably lower than the activation energy on the low-index (111) plane at an analogue surface coverage (2.2 eV, $\theta = 0.125$). The electron donation from the rhodium surface to the NO on the stepped surface (Mulliken charges: N: -0.23 e; O: -0.26 e) is not much different from that on the low-index (111) surface (Mulliken charges: N: -0.24 e, O: -0.22 e). This suggests that the higher activity of the stepped surface is more likely due to steric than to electronic effects.

To visualise the surface more realistically, the NO decompositions on Rh(311) and Rh(111) are depicted in CPK style. In both cases the nitrogen atom hardly adjusts its position, therefore only the different positions of oxygen in the reactant structure (O(r)) the transition state (O(ts)) and the product structure (O(p)) are marked. It can be seen that in case of the stepped surface the oxygen atom in the reactant structure is close to its position in the transition state. The oxygen position in the transition state is again close to its position in the product geometry.

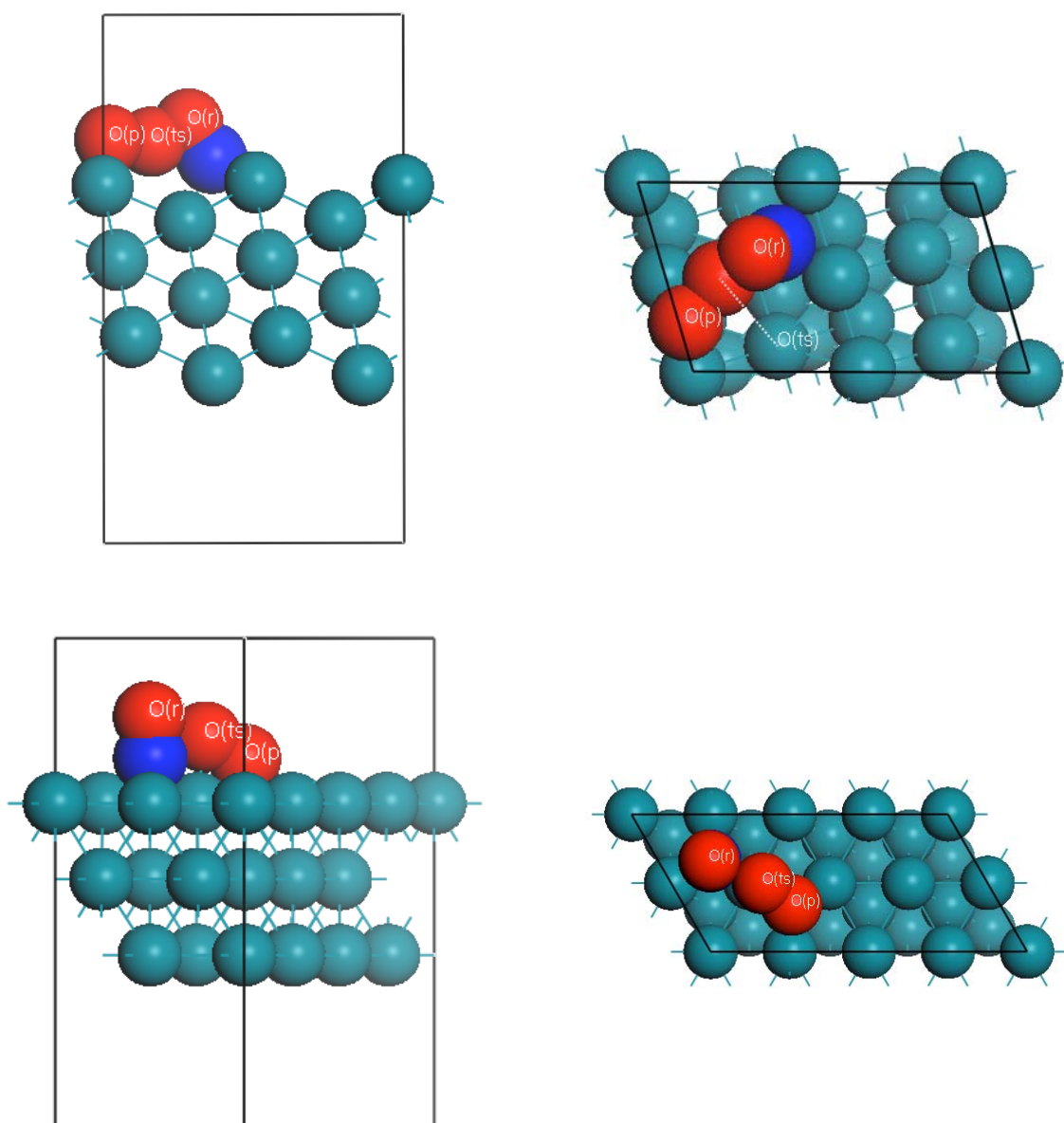


Figure 8.3: Corey-Pauling-Koltum (CPK) style visualisation of the NO dissociation on Rh(311) (upper row) and Rh(111) (lower row)

In case of the NO decomposition on Rh(111), the distances the oxygen atom has to cover in the dissociation process are longer, as can best be seen in the Corey-Pauling-Koltum (CPK) style visualisation (Figure 8.3, lower row). The radii of the atoms in CPK style are proportional to their van der Waals radii and are therefore more realistic than the usual visualisation. It can be seen that on the stepped surface the position of the oxygen in reactant and transition state structure overlap (upper row), while they are separated on the plane surface (lower row). Exact values are given in Table 8.1. Moreover, the thermochemistry of the NO dissociation is inverted, when changing from the plane to the stepped surface.

Distances (pm)	Rh(111)	Rh(311)
O(r) – O(ts)	226	129
O(ts) – O(p)	121	153
O(r) – O(p)	336	271

Table 8.1: Distances of the oxygen atoms in product, transition state and reactant structure of the NO dissociation on the stepped Rh(311) and the plane Rh(111)

8.2.3 NO Dissociation in Presence of Oxygen

Placing an additional oxygen in a 3-fold hollow of the (111) part of the stepped surface, adjacent to the NO molecule (see Figure 8.4), exhibits direct influence on the electron transfer. Mulliken charge analysis determines the partial charge on the nitrogen atom to be -0.21 e, while -0.23 e on the oxygen atom. On the equivalent low-index (111) surface the electron donation to the NO molecule is only slightly different (N: -0.23 e; O: -0.21 e).

A calculation of the potential energy surface for the decomposition reaction determines the activation energy for the dissociation process to be 1.71 eV. The reaction is still exothermic in presence of this oxygen preoccupation, but the energy gain is smaller (-0.19 eV).

While Mulliken charges of NO on stepped and plane surface are only slightly different, the activation energy is with 2.26 eV considerably higher than on the stepped surface (1.71

eV). The thermochemistry is again inverted when changing the surface from stepped to plane (stepped: $\Delta E_{\text{react}} = -0.19$ eV, plane: $\Delta E_{\text{react}} = 0.14$ eV).

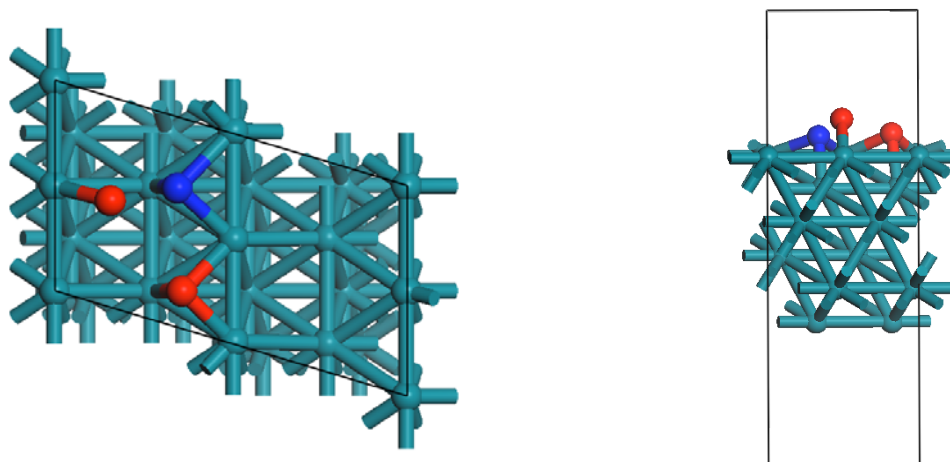


Figure 8.4: Nitrogen monoxide dissociation on rhodium(331) in presence of an oxygen atom

Coadsorbant	E_{act} [eV]	ΔE_{react} [eV]
None	1.50	-0.52
O	1.71	-0.19
2 O	1.76	-0.10

Table 8.2. Activation energy and energy of reaction for the NO dissociation on Rh(311) with different oxygen preoccupations

A placement of two oxygen atoms on the surface and subsequent recalculation of the process shows that the activation barrier increases more and the process becomes less exothermic. An overview over the activation energies of the reaction and their thermochemistry is given in Table 8.2.

8.2.4 NO Dissociation in Presence of Further Coadsorbants

The influence of further molecules that will also be present in the real catalytic converter on the NO dissociation on stepped surfaces must also be considered. Replacing oxygen as coadsorbant on the (111) facet of the Rh(311) surface by atoms and molecules, such as atomic nitrogen or sulphur and SO and CO, and recalculating the PES for the NO dissociation lead to the following kinetic and thermochemical parameters (Table 8.3).

Coadsorbant	E_a [eV]	ΔE_{react} [eV]
Without	1.50	-0.52
N	1.65	-0.1
SO	1.39	-0.4
S	1.51	-0.3
CO	1.60	-0.2

Table 8.3. Activation energy and energy of reaction for the NO dissociation on Rh(311) with different coadsorbants

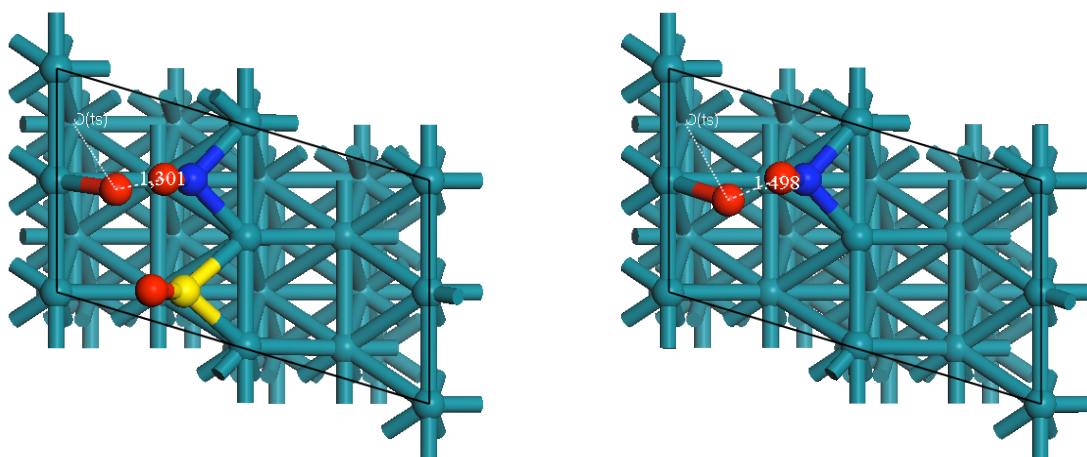


Figure 8.5: Comparison of the oxygen position in reactant and transition state (O(ts)) of the NO dissociation in absence of a coadsorbant and in presence of SO

Since all coadsorbant are electron withdrawing one would expect that the activation energies are all higher than the activation energy for the dissociation of the solely adsorbed NO.

Therefore, it is striking to see that in case of SO as a coadsorbant the activation energy decreases, in contrast to all other coadsorbants. Even though the electron transfer of NO coadsorbed with SO, relative to that of NO solely adsorbed, decreases, the activation energy decreases.

A comparison of the transition state positions of the oxygen atom for the NO dissociation with and without oxygen as a coadsorbant (Figure 8.5) shows that the transition state position of the oxygen atom is shifted when SO is present. The shifting is most likely due to a repulsion of the partially negative charged oxygen atoms (SO and NO). As can be seen from Figure 8.5, oxygen in the transition state of the coadsorbed variant is shifted towards the decomposing metal atom. Furthermore, the distance to its position in the reactant structure decreases. The decrease in activation barrier is thus – in analogy to the observed difference between plane and stepped surfaces – due to steric effects rather than electronic. This result supports the earlier finding that electronic effects do influence the reaction, but are exceeded by steric effects.

8.3 Conclusions

In this Chapter it was shown that steric effects exceed electronic effects on the decomposition of NO on rhodium. The electron donation of NO adsorbed on the (111) facet is almost equal to that on the (311) facet. However, the activation energy of the decomposition is considerably lower on the (311) than on the (111) facet. This is most likely due to the fact that the atoms of the NO are rather close to their position in the product structure. Nevertheless, when considering the same geometry, electronic effects influence the activation barrier of the reaction. This assumption is supported by the findings for the NO dissociation with SO as coadsorbant. Electro-static repulsion directs the oxygen of NO in direction of its transition state position, and, even though the electron transfer decreases, the activation barrier decreases.

The presented material supports the catalytic mechanism proposed by Nakatsuji. If NO decomposes preferably at steps of the rhodium surface [100], a high concentration of atomic nitrogen at those step sites builds up. At this high-nitrogen microenvironment around step sites nitrogen could recombine without diffusing over longer distances. This is a possible explanation of the surface chemistry of the NO_x-decomposition catalyst. To verify this assumption the behaviour of oxygen at these step-sites would have to be studied as well.

Chapter 9: Influence of Coverage-Dependent Kinetics on the Catalyst Behaviour

9.1 Motivation

In order to decide if the coverage dependencies estimated in the previous Chapters are indeed the causality of the inaccurate prediction of the transient behaviour of the heterogeneous catalyst (Chapter 3), kinetic simulations of example cases with and without accounting for the coverage dependent kinetics were carried out. The calculated self-inhibition of the oxygen dissociation on rhodium(111) could possibly explain why NO in an excess of oxygen is decomposed even though initial kinetic simulations support the contrary.

It is known that the surface of metal particles consists mainly of the dense packed (111) surface areas with steps at the interface of those areas (see Chapter 8). As investigated in Chapters 5 – 8 and supported by kinetic data from literature, decomposition reactions proceed much faster on steps than on plane facets. This in turn means that the main part of the surface is rather inactive in case of nitrous oxide and in case of oxygen rather inactive at high coverages. Since it was shown in Chapter 7 that diffusion from and to those more active stepped sites is rather unlikely for atomic species, decomposition at active steps and subsequent diffusion to the plane, inactive areas is rather unlikely either.

Surface science studies report that generating Rh(111) with a complete monolayer of oxygen is difficult to achieve, while partial monolayers are built rather instantaneously.

9.2 Results and Discussion

9.2.1 Oxygen Flow with CO Pulses - Revisited

As explained in Chapter 5 of this thesis, experimental results as well as DFT calculation carried out in our group point towards a level-off of the oxygen at approximately 0.5 ML at room temperature.

However, kinetic simulation of a stream of 2.5 % V/V oxygen in an argon matrix at 300 K show that the rhodium surface is immediately covered by atomic oxygen due to a very fast dissociative adsorption of oxygen (Figure 9.1, square marked lines). Taking the oxygen coverage dependent dissociation energy for molecular oxygen into account (see Chapter 5), shows that kinetic simulations support this levelling-off (Figure 9.1, circle-marked lines).

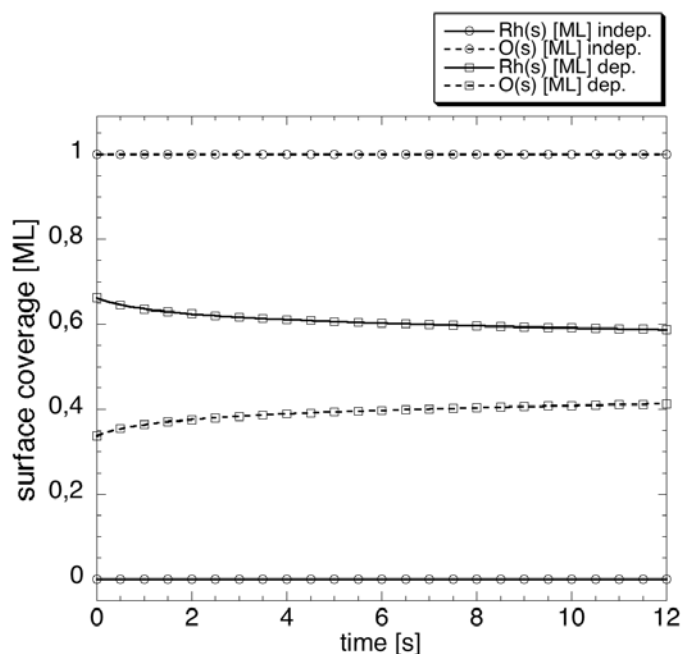


Figure 9.1: Comparison of the simulated surface coverages with and without accounting for surface coverage dependent kinetics

This indicates that for predicting the surface occupation, coverage dependencies have to be taken into account. Furthermore, this could severely influence the over-all behaviour of transient processes since here one has to deal with fast changing surface compositions.

As an example, the same system was calculated with 2 carbon monoxide pulses (2.5 % V/V) of 1 s after 4 s of oxygen in argon. This calculation shows that also in this case the oxygen coverage levels off, while carbon monoxide occupies the remaining vacant adsorption sites shortly after it is dosed into the inlet stream (Figure 9.2). The surface occupation stays constant, because the catalyst temperature (300 K) is beneath the minimum temperature required for the oxidation of CO on rhodium.

The composition of the outlet stream shows that CO goes through the catalytic system completely unaffected. Therefore, microkinetic modelling based on knowledge gained by DFT investigations is in agreement with the overall catalytic behaviour.

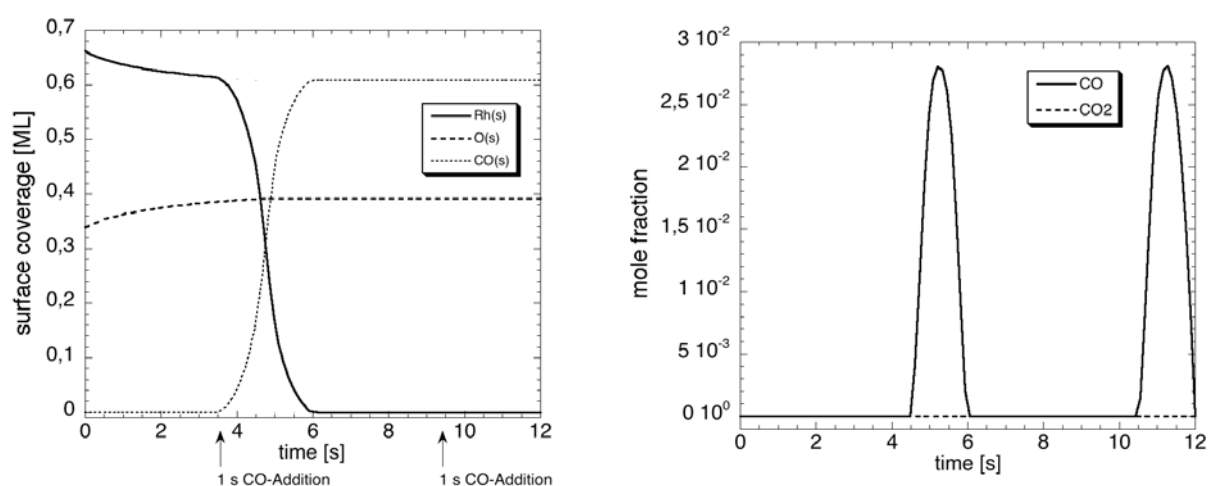


Figure 9.2: CO and O₂ flowing through a rhodium-loaded catalytic channel beneath the oxidation light-off temperature

Recalculation of these systems at a temperature above the ignition temperature of the CO oxidation on rhodium shows that level-off coverage of oxygen is reached faster, while during the phases with CO in the inlet gas oxygen is removed from the surface due to oxidation. The amount of CO on the surface is negligible owing to a fast oxidation by the oxygen preoccupation at 600 K. Comparison of surface coverages with conversions as a function of time supports this assumption, since CO₂ is formed simultaneous to the oxygen coverage reduction (Figure 9.3).

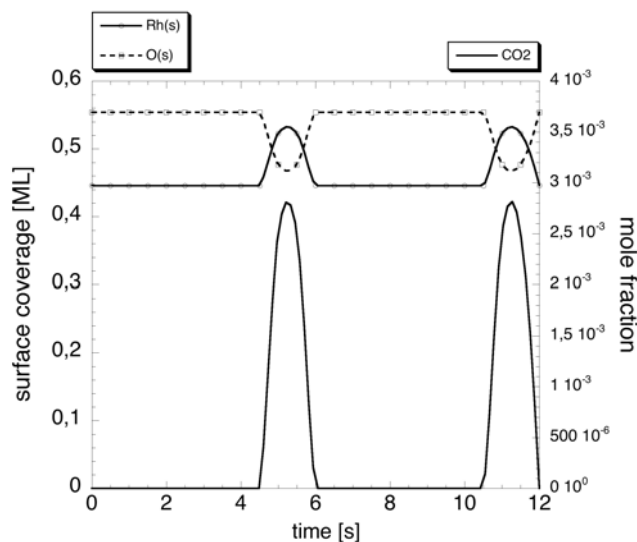


Figure 9.3: Comparison of the surface coverages and conversions

Comparison of the surface coverages calculated for this system with and without accounting the oxygen coverage dependence of the oxygen dissociation leads to the conclusion that this behaviour could not be explained with independent kinetics since the surface is oxygen-poisoned after the pure oxygen phase. In case of the dependent kinetics the simulations predict that there are sufficient vacant adsorption sites for CO to adsorb and to be oxidised (Figure 9.4)

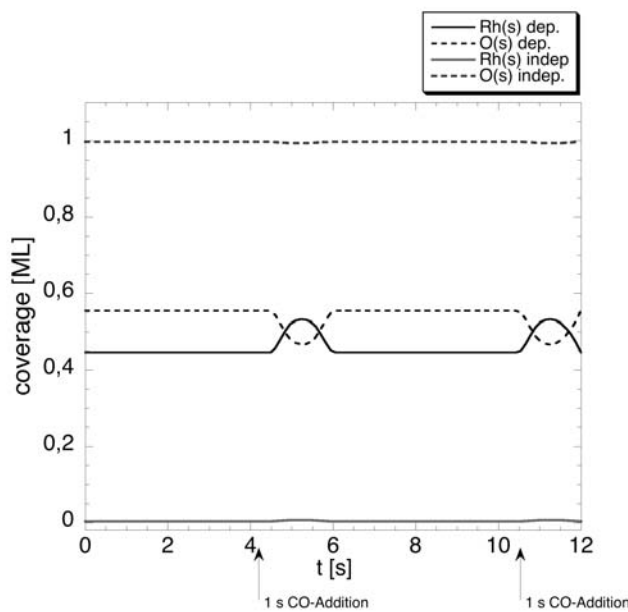


Figure 9.4: Comparison of the surface coverages with coverage dependent and independent kinetics for the oxygen decomposition

For decomposition processes such as the NO_x decomposition discussed in this thesis, this is of severe importance, since the decomposing species not only needs a vacant adsorption site, but also an adjacent vacant adsorption site to decompose, see Chapter 5 .

To enforce stronger gradients on the surface, an analogue system with 8 % V/V oxygen during the CO free phase was simulated at 550 K. The levelling-off of the oxygen occupation is disrupted by the carbon monoxide pulses. During the CO pulse, the gradient of the oxygen coverage is stronger, because at 550 K the CO oxidation dominates the surface chemistry. The simultaneous CO_2 formation (Figure 9.5, left) supports this assumption. Subsequent to these carbon monoxide pulses the oxygen coverage increases, begins to level off, but is again disrupted by the next CO pulse.

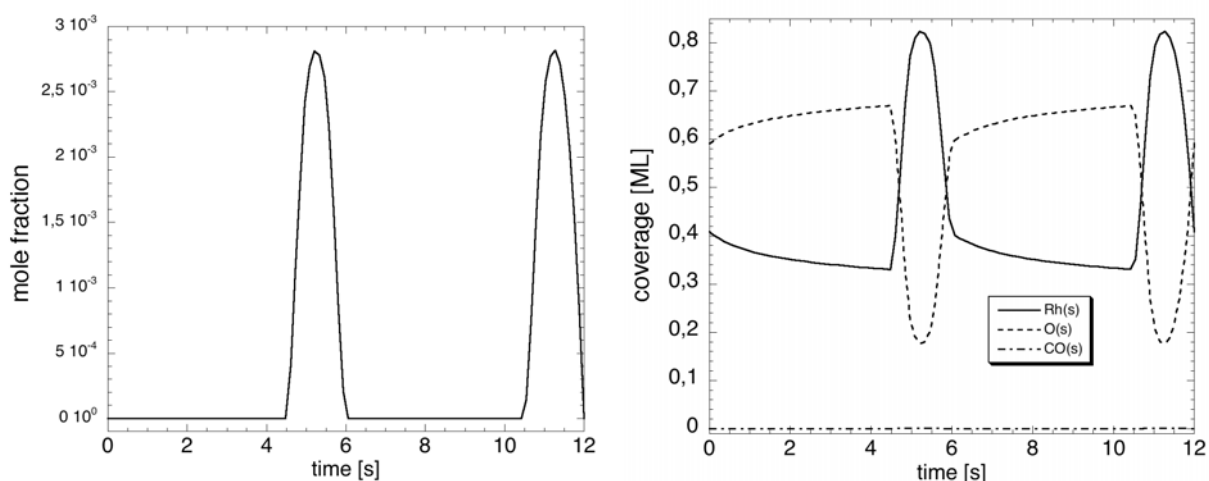


Figure 9.5: Disruption of the levelling-off of the oxygen coverage by CO pulses

Extension of the simulation to 60 s shows that the surface coverage does not reach a steady state in this system owing to the continuous disruptions owing to CO pulses and its oxidation on the surface.

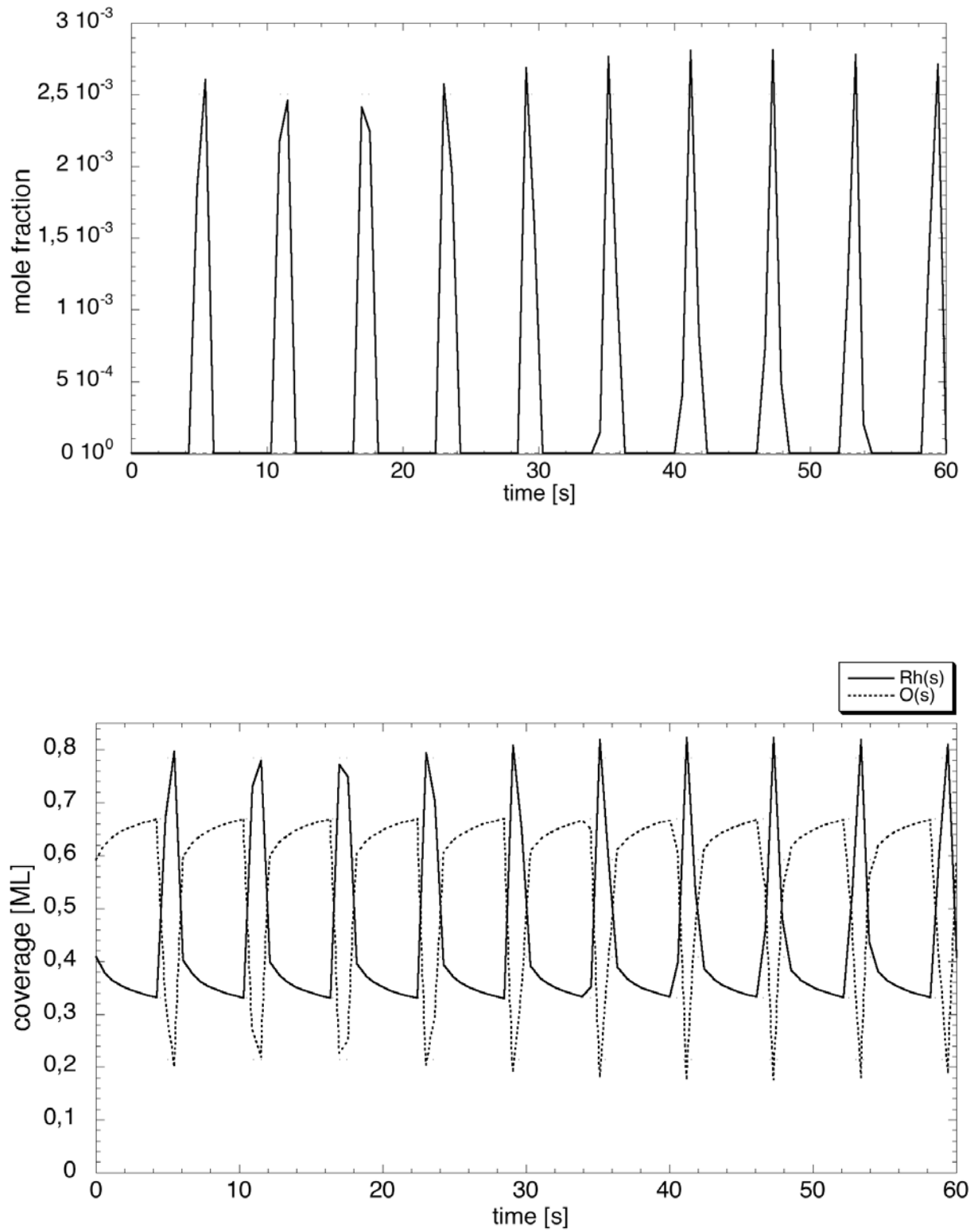


Figure 9.6: Disruption of the levelling-off effect over a longer period of time

9.2.2 NO Reduction and Nitrogen Formation - Revisited

Surface Coverages

The problem of the instant and complete poisoning of the rhodium surface in a catalyst during the lean phase in the system presented in Chapter 3 is reconsidered. (500 ppm of NO in Ar plus 6 seconds 14.5 % O₂ (lean), followed up by a 1-s pulse of 2 % V/V H₂ (rich)). It was shown that using coverage-independent kinetics NO could adsorb and nitrogen could be formed only during the rich phases. This effect is attributed to the very fast oxygen poisoning of the rhodium surface (Figure 9.7, left graph). Only during the rich phases ($t = 6-7$ s & $13-14$ s) the surface is slightly reduced and NO can decompose to form N₂. In the subsequent lean phase the surface is again immediately poisoned by oxygen.

However, results by Nakatsuji and co-workers [15, 16, 63, 64] as well as experiments carried out within the ConNeCat research consortium show that the nitrogen is formed mainly during the lean phase; the rich phase is only required for activation.

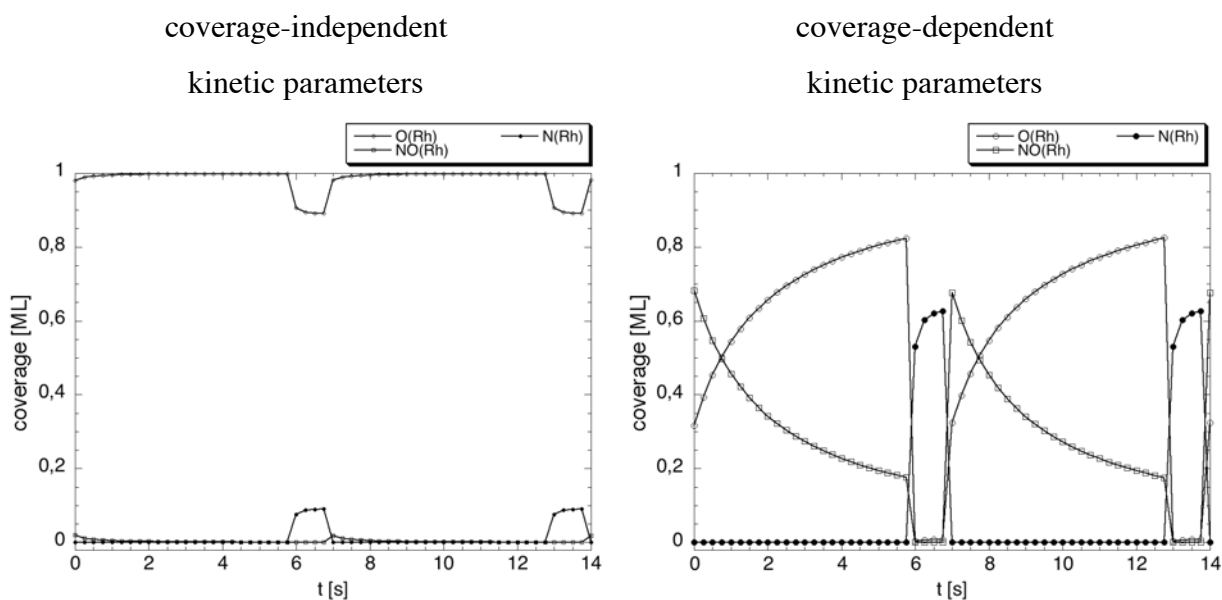


Figure 9.7: Surface coverages of rhodium in a catalyst operated under altering lean-rich conditions

A recalculating of this system using coverage-dependent kinetics gives a possible explanation. In this case, NO has the opportunity to adsorb on Rh simultaneously to oxygen, since the oxygen coverage of the surface levels off (see $t = 1-6$ s, right graph). Moreover, vacant surface sites are available so that NO can decompose. This is a possible explanation for the N_2 formation during the lean phase. During the rich phase oxygen is removed from the surface, nitrogen accumulates (see $t = 6-7$ s, right graph). Subsequent to the rich phase NO is again able to adsorb and decompose on the surface (see $t = 7-8$ s). A comparison of the surface coverages and the calculated nitrogen formation is discussed in the subsequent paragraph.

Influence of Coverage-Dependent Kinetic Parameters on Conversions

A comparison of the calculated coverages with the calculated nitrogen formation shows that the transient behaviour of surface overlayer reflects in the formation of nitrogen (Figure 9.8). The nitrogen formation peaks during the rich period, simultaneous to the nitrogen accumulation on the surface. Furthermore, the catalyst is activated for further NO decomposition, because subsequent to the reduction of the surface, NO can adsorb. This activation reflects in the nitrogen formation during the oxygen-rich phase, which decreases – simultaneously to the NO coverage – during this phase, until the catalyst is again activated by a fuel-rich phase.

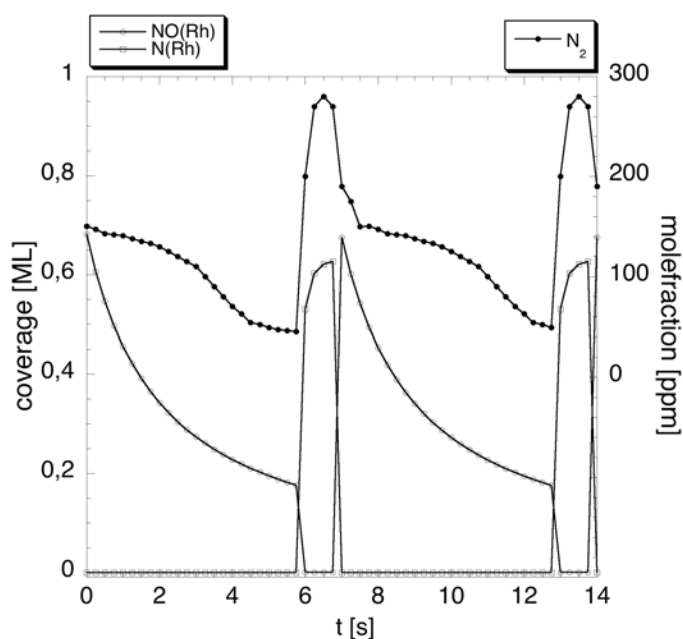


Figure 9.8: Comparison of nitrogen and NO surface coverages with nitrogen formation as a function of time

These observations are all well in accordance with the mechanism proposed Nakatsuji. The fuel-rich phase reduces the rhodium surface and herewith enables NO adsorption (Figure 9.8, NO coverage) and decomposition (Figure 9.8, N coverage) on surface. During the subsequent oxygen-rich phase this activity decreases, which is reflected in a decreasing NO coverage and a reduced nitrogen formation. These findings are in accordance with measurement carried out by industrial partners [67].

In a next step conversions of an analogue system with prolonged lean and rich phases (lean: 60 s, rich: 5s) were calculated as a function of the temperature [101]. The results were compared to experimental data (Figure 9.9). It can be seen that the trend and the value are reproduced quite well. However, in the low temperature region at 160°C the difference between calculated and measured values is immoderate. Overall, and especially in the relevant temperature window (200°C - 400°C), the agreement is satisfactory.

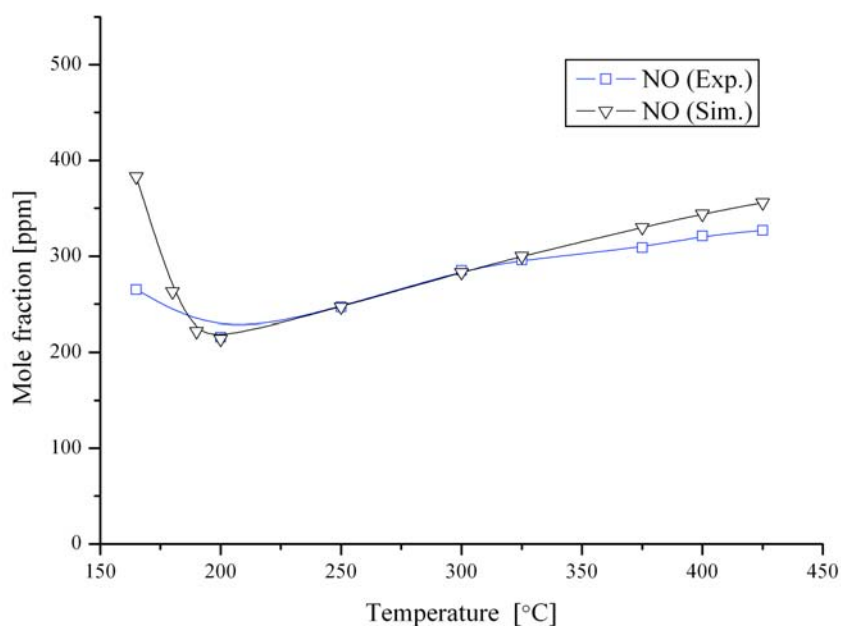


Figure 9.9: Mean NO concentration in the outlet gas as a function of the temperature [101]

9.2.3 Influence of a Coverage-Dependent Kinetic Parameter on the NO Oxidation

In a further study Q. Su investigated the influence of the oxygen-coverage dependent activation energy of the NO oxidation reaction onto the NO₂ formation [101]. Experimental studies of the conversion of a flow of 550 ppm NO_x (500 ppm NO and 50 ppm NO₂) and 14 % V/V O₂ in nitrogen through the standard catalyst under standard condition (see Appendix C)

were compared to simulation results produced by DETCHEM^{TRANSIENT}. The model was based on the reactions of NO and O₂ on rhodium (Appendix A).

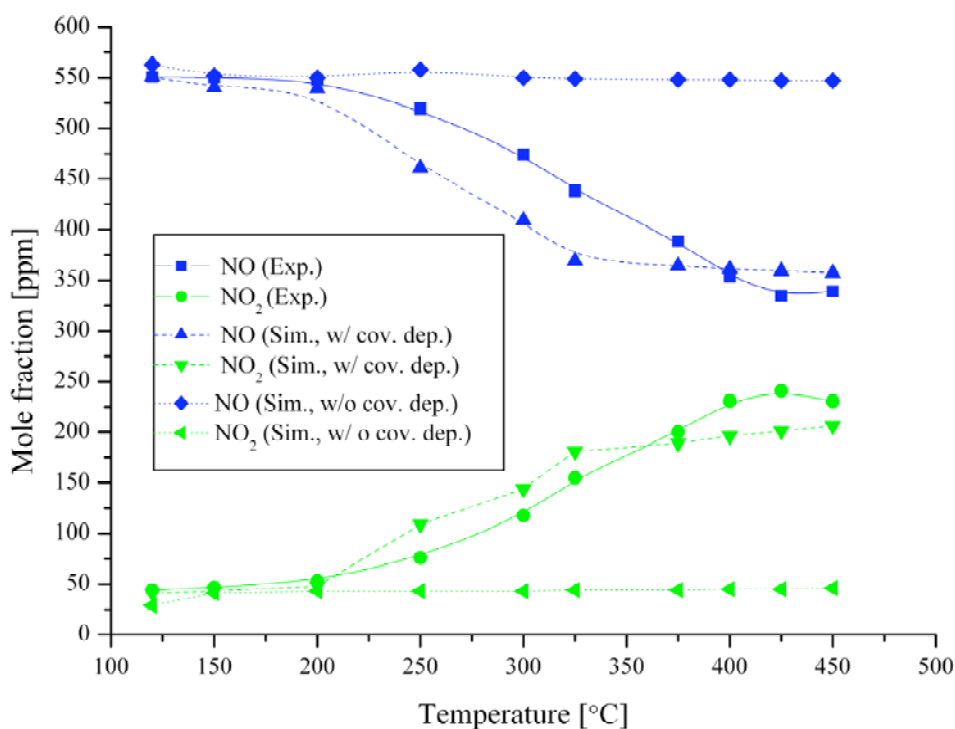


Figure 9.10 NO and NO₂ mole fractions as function of the temperature, comparison of experimental results to simulations based on a chemistry model with and without coverage-dependent kinetic parameters [101]

The NO conversion and NO₂ formation was simulated as a function of temperature and compared to experimental results. As can be seen from Figure 9.10, in the case in which activation of the NO oxidation with increasing oxygen coverage is not taken into account, simulations predict almost no conversion of NO to NO₂ absolutely, contrary to experimental observation [67]. In case the activation is taken into account, the trend of the experimentally determined NO₂ formation and NO conversion is reproduced. These findings emphasise that coverage-dependent activation energies have to be taken into account in microkinetic modelling, in order to simulate conversions in catalytic converters accurately.

9.3 Conclusions

To simulate the transient behaviour of a heterogeneous catalyst, coverage dependent kinetics have to be taken into account, in case coverages vary over a broad range as learned from DFT investigation (Chapters 5 - 8). In this chapter it was shown that the surface coverage and the conversion in the transient CO oxidation on rhodium is not predicted accurately when calculated with initial, coverage-independent kinetics. Moreover, it could be pointed out that in the NO reduction under altering lean-rich conditions, in which the composition of the surface overlayer varies strongly, coverage-dependent kinetic parameters have to be utilised in order to achieve reasonable results. This was exemplified using a transient lean-rich DeNO_x system with an direct comparison to experimental results. Furthermore, it was shown that in order to predict the NO oxidation over rhodium accurately, dependencies of the oxygen coverages are necessary. The results obtained from the presented work will be used to construct a realistic model of a rhodium-based NO_x decomposition catalyst as proposed by Nakatsuji.

Chapter 10: Conclusion and Outlook

In this thesis a code that calculates a transient reacting flow within a heterogeneous catalyst utilising a multiscale modelling approach (DETCHEM^{TRANSIENT}) was presented. By comparing simulation results of DETCHEM^{TRANSIENT} based on a previously verified chemistry model to experimental data of simple model systems, it was shown that the predictions are indeed accurate. However, when investigating more complex systems, it appeared that surface coverages on rhodium (*i.e.*, oxygen coverage) were overestimated and conversion/production of species were not in agreement with experimental findings.

Since kinetic parameter for oxygen reactions on rhodium were already successfully applied in simulations of steady-state processes, it was assumed that they are correct, but specific for a certain coverage.

Therefore, DFT investigations of rhodium surfaces were carried out in order to gain a more detailed insight in the nature of the surface reactions. It could be shown that the predominant plane in real fcc metal catalyst particles is rather inactive towards NO dissociation. This is even more distinct when the surface is covered with oxygen to a high extent. Furthermore, it was shown that oxygen initially dissociates fast on this facet of rhodium, while this process is self-inhibiting, since the activation barrier increases with increasing coverage. Charge analysis carried out supports that these deactivation effects owe to the electron withdrawing effect of electronegative oxygen in case of both decomposition reactions.

Analogue DFT investigations for monatomic steps, the most common defect on rhodium catalyst particles, showed that decomposition is more likely here, while it is also deactivated by electron withdrawing coadsorbants. Furthermore, it could be shown that even though electronic effects can steer the probability of dissociation, steric effects exceed them.

The qualitative knowledge gained by DFT investigation of surface reactants could be directly applied to improve the accuracy of reactive flow simulations. First example cases were shown to illustrate this and further, more realistic models of NO_x decomposition catalysts are being developed.

On this basis it seems obvious that, for accurate simulation of the catalytic system proposed by Nakatsuji, coverage-dependent kinetic parameters of the elementary reaction steps have to be considered. Oxygen coverages simulated with coverage-dependent kinetic parameters lead to results that are much closer to experimental findings. Moreover, measured transient conversions in a catalytic monolith can be described accurately by models based on coverage-dependent kinetics (Chapter 9).

The results presented within this thesis maintain that automotive catalytic converters can indeed be described by a multiscale modelling approach. Processes were described on different relevant levels from the microscopic to the macroscopic, *i.e.*, from the quantum chemistry to the continuum engineering level. In particular, insight gained on the quantum chemistry level could aid the understanding of processes on much higher length and time scales.

12 List of References

1. J. A. Moulijn, P. W. N. M. v. Leeuwen and R. A. v. Santen, "*History of catalysis*" in "*Catalysis: An integrated approach to homogenous, heterogenous and industrial catalysis*", J. A. Moulijn, P. W. N. M. v. Leeuwen and R. A. v. Santen (Eds.) **1993**, Elsevier, Amsterdam
2. J. M. Berg, J. L. Tymoczko and L. Stryer, "*Biochemistry*", **2002**, W.H. Freeman and Co., New York
3. B. Gilland, "*World population and food supply – can food production keep pace with population growth in the next half-century?*" *Food Policy* **2002**, 27, 47-63
4. P. W. N. M. v. Leeuwen, "*Homogeneous catalysis: Understanding the art*", **2004**, Kluwer Academic, Dordrecht ; London
5. G. A. Somorjai, "*Introduction to surface chemistry and catalysis*", **1994**, Wiley, New York ; Chichester
6. G. Ertl, H. Knözinger and J. Weitkamp, "*Handbook of heterogeneous catalysis*", **1997**, VCH, Weinheim
7. H. S. Gandhi, G. W. Graham and R. W. McCabe, "*Automotive exhaust catalysis*", *J. Catal.* **2003**, 216, 433-442
8. R. M. Heck and R. J. Farrauto, "*Automobile exhaust catalysts*", *Appl. Catal. A* **2001**, 221, 443-457
9. O. Deutschmann, U. Riedel and J. Warnatz, "*Modelling of surface reactions in hypersonic re-entry flow fields*", *Proc. of the Second European Symposium on Aerothermodynamics for Space Vehicles* **1995**, *ESA SP-367*, 305-310
10. D. A. King, "*Environment - Climate change science: Adapt, mitigate, or ignore?*" *Science* **2004**, 303, 176-177
11. D. Chatterjee, O. Deutschmann and J. Warnatz, "*Detailed surface reaction mechanism in a three-way catalyst*", *Faraday Discuss.* **2001**, 119, 371-384
12. D. Chatterjee, "*Detaillierte Modellierung von Abgaskatalysatoren*" **2001**, Ph.D. Thesis, University of Heidelberg, Heidelberg
13. L. S. Glebov, A. G. Zakirova, V. F. Tret'yakov, T. N. Burdeinaya and G. S. Akopova, "*State of the art of catalytic conversion of NO_x into N₂*", *Petroleum Chemistry* **2002**, 42, 143-172

14. M. Hilgendorff, "*NO_x abatement by catalytic traps : On the mechanism of NO_x trapping under automotive conditions.*" *Top. Catal.* **2004**, 30/31, 155-160
15. T. Nakatsuji and V. Komppa, "*A catalytic NO_x reduction system using periodic steps, lean and rich operations*", *Catalysis Today* **2002**, 75, 407-412
16. T. Nakatsuji and V. Komppa, "*A catalytic NO_x reduction system using periodic two steps: An operation in oxidizing conditions and a relatively short operation in reducing conditions*", *Appl. Catal. B* **2001**, 30, 209-223
17. S. Kureti, W. Weisweiler and K. Hizbullah, "*Simultaneous conversion of nitrogen oxides and soot into nitrogen and carbon dioxide over iron containing oxide catalysts in diesel exhaust gas*", *Appl. Catal. B: Environmental* **2003**, 43, 281-291
18. I. Orlandini and U. Riedel, "*Oxidation of propene and the formation of methyl nitrate in non-thermal plasma discharges*", *Catalysis Today* **2004**, 89, 83-88
19. I. Orlandini and U. Riedel, "*Chemical kinetics of NO-removal by pulsed corona discharges*", *Journal of Physics D: Applied Physics D* **2000**, 33, 2467-2474
20. I. Orlandini and U. Riedel, "*Modelling of NO- and HC-removal by non-thermal plasmas*", *Combustion Theory and Modelling* **2001**, 5, 447-462
21. O. Deutschmann, "*Interactions between transport and chemistry in catalytic reactors*" **2001**, Habilitationsschrift, University of Heidelberg, Heidelberg
22. <http://www.detchem.com>,
23. S. Tischer, "*Simulation katalytischer Monolithreaktoren unter Verwendung detaillierter Modelle für Chemie und Transport*" **2004**, Ph.D. Thesis, University of Heidelberg, Heidelberg
24. R. Kissel-Osterrieder, "*Detaillierte Modellierung heterogener Katalyse am Beispiel der Oxidation von CO auf Platinoberflächen*" **2000**, Ph.D. Thesis, University of Heidelberg, Heidelberg
25. L. Ciossu, "*Monte-Carlo simulations*" **2005**, Ph.D. Thesis, in preparation, University of Heidelberg, Heidelberg
26. A. Einstein, "*Über die spezielle und allgemeine Relativitätstheorie*", **2001**, Springer, Berlin
27. E. Schrödinger, M. Planck, A. Einstein and H. A. Lorentz, "*Briefe zur Wellenmechanik*", **1963**, Springer, Berlin
28. P. Hohenberg and W. Kohn, "*Inhomogeneous electron gas*", *Phys. Rev.* **1964**, 136, 864-871

29. M. Born and J. R. Oppenheimer, "*Zur Quantentheorie der Molekeln*", *Annalen der Physik* **1927**, *84*, 457-484
30. B. D. Bunday, "*Basic optimisation methods*", **1984**, E. Arnold, London ; Baltimore, MD
31. W. Kohn and L. J. Sham, "*Self-consistent equations including exchange and correlation effects*", *Phys. Rev.* **1965**, *140*, 1133-1139
32. S. Lundqvist and N. H. March, "*Theory of the inhomogenous electron gas*", **1983**, Plenum Press, New York
33. J. P. Perdew, J. A. Chevary, S. H. Vosko, K. A. Jackson, M. R. Pederson and C. Fiolhais, "*Atoms, molecules, solids, and surfaces: Applications of the generalized gradient approximation for exchange and correlation*", *Phys. Rev. B* **1992**, *46*, 6671-668
34. B. Hammer and J. K. Nørskov, "*Theoretical surface science and catalysis - calculations and concepts*", *Adv. Catal.* **2000**, *45*, 71
35. B. Hammer, "*Coverage dependence of N₂ dissociation at an N, O, or H precovered Ru(0001) surface investigated with density functional theory*", *Phys. Rev. B* **2001**, *63*, 205423
36. Z. P. Liu, S. J. Jenkins and D. A. King, "*Car exhaust catalysis from first principles: Selective NO reduction under excess O₂ conditions on Ir*", *J. Am. Chem. Soc.* **2004**, *126*, 10746-56
37. Z.-P. Liu and P. Hu, "*General rules for predicting where a catalytic reaction should occur on metal surfaces: A density functional theory study of C-H and C-O bond breaking/making on flat, stepped, and kinked metal surfaces*", *J. Am. Chem. Soc.* **2003**, *125*, 1958-1967
38. Z.-P. Liu, "*Chemical reactions at surfaces and interfaces from first principles: Theory and application*", *Pure Appl. Chem.* **2004**, *76*, 2069-2083
39. M. D. Segall, P. L. D. Lindan, M. J. Probert, C. J. Pickard, P. J. Hasnip, S. J. Clark and M. C. Payne, "*First-principles simulation: ideas, illustrations and the CASTEP code*", *J. Phys.: Cond. Matt.* **2002**, *14*, 2717-2743
40. H. J. Monkhorst and J. D. Pack, "*Special points for Brillouin-zone integrations*", *Phys. Rev. B* **1976**, *13*, 5188-5192
41. Q. Ge, P. Hu, D. A. King, M. H. Lee, J. A. White and M. C. Payne, "*Site symmetry dependence of repulsive interactions between chemisorbed oxygen atoms on Pt{100}-(1x1)*", *J. Chem. Phys.* **1997**, *106*, 1210-1215

42. V. Milman, B. Winkler, J. A. White, C. J. Pickard, M. C. Payne, E. V. Akhmatkaya and R. H. Nobes, "*Electronic structure, properties and phase stability of inorganic crystals: A pseudopotential plane-wave study*", Int. J. Quant. Chem. **2000**, 77, 895
43. N. Govind, M. Petersen, G. Fitzgerald, D. King-Smith and J. Andzelm, "*A generalized synchronous transit method for transition state location*", Comp. Mater. Sci. **2003**, 28, 250-258
44. H.-R. Volpp and J. Wolfrum, "*Sum-frequency generation (SFG) vibrational spectroscopy as a means for the investigation of catalytic combustion*" in "*Applied combustion diagnostics*", K. Kohse-Höinghaus and J. Jeffries (Eds.) **2002**, Taylor & Francis, London, New York
45. H. Härle, A. Lehnert, U. Metka, H.-R. Volpp, L. Willms and J. Wolfrum, "*In-situ detection and surface coverage measurements of CO during CO oxidation on polycrystalline platinum using sum-frequency generation*", Appl. Phys. B. **1999**, 68, 567-572
46. O. R. Inderwildi, H.-R.-. Volpp, D. Starukhin, L. Ciossu, D. Lebiez, O. Deutschmann and J. Warnatz, "*Reaction processes on catalytically active surfaces*" in "*Reactive flows, diffusion and transport*", R. Rannacher et al. (Eds.) **2005**, Springer, Berlin Heidelberg
47. P. J. F. Griffiths and J. D. R. Thomas, "*Calculations in advanced physical chemistry*", **1983**, E. Arnold, London
48. P. W. Atkins, "*Physical chemistry*", **1998**, Oxford University Press, Oxford
49. J. A. Moulijn, P. W. N. M. v. Leeuwen and R. A. v. Santen, "*Catalysis : An integrated approach to homogeneous, heterogeneous and industrial catalysis*", **1993**, Elsevier, Amsterdam ; London
50. E. S. Lox and B. H. Engler, "*Handbook of heterogeneous catalysis*", **1997**, VCH, Weinheim
51. R. E. Hayes and S. T. Kolaczkowski, "*Introduction to catalytic combustion*", **1997**, Gordon and Breach Science Publishers, Amsterdam
52. D. J. Acheson, "*Elementary fluid dynamics*", **1990**, Clarendon Press, Oxford
53. M. Feistauer, "*Mathematical methods in fluid dynamics*", **1993**, Longman Scientific & Technical ;, Wiley, Harlow, Essex, England, New York
54. C. A. J. Fletcher, "*Computational techniques for fluid dynamics*", **1991**, Springer-Verlag, Berlin ; New York
55. J. Warnatz, D. R. and U. Maas, "*Combustion*", **1996**, Springer, Berlin, Heidelberg

56. R. J. Kee, "*Chemically reacting flow*", **2003**, Wiley, New York
57. H. Schlichting, "*Boundary-layer theory*", **2000**, Springer, Berlin Heidelberg
58. R. Schwiedernoch, S. Tischer, C. Correa and O. Deutschmann, "*Experimental and numerical study of the transient behavior of a catalytic partial oxidation monolith*", Chem. Eng. Sci. **2003**, 58, 633-642
59. P. Deuflhard, E. Hairer and J. Zugk, "*One-step and extrapolation methods for differential algebraic equations*", Num. Math. **1987**, 51, 501-516
60. T. R. Chandrupatla and A. D. Belegundu, "*Introduction to finite elements in engineering*", **2002**, Prentice-Hall, Upper Saddle River, NJ
61. Fluent, Version 5, **1998**
62. L. L. Raja, R. J. Kee, O. Deutschmann, J. Warnatz and L. D. Schmidt, "*A critical evaluation of Navier–Stokes, boundary-layer, and plug-flow models of the flow and chemistry in a catalytic-combustion monolith*", Catalysis Today **2000**, 59, 47-60
63. T. Nakatsuji, "*A highly durable catalytic NO_x reduction in the presence of SO_x using periodic two steps, an operation in oxidizing conditions and a relatively short operation in reducing conditions*", Appl. Catal. B. **1999**, 21, 121
64. T. Nakatsuji, J. Ruotoistenmäki, M. Matsubara, T. Uekusa and Y. Tanaka, "*A new transient NO_x direct catalytic decomposition on a Rh-based catalyst*", SAE Technical Papers **2003**, 2003-01-3243
65. Q. Su, "*Transient simulation of a NO_x decomposition catalyst*" **2005**, Ph.D. Thesis, in preparation, University of Heidelberg
66. C. H. F. Peden, D. W. Goodman, D. S. Blair, J. B. P. G. B. Fisher and S. H. Oh, "*Kinetics of CO oxidation by O₂ or NO on Rh(111) and Rh(100) single crystals*", J. Phys. Chem. **1988**, 92, 1563
67. J. Maier, Measurements, **2004**
68. Q. Su, Simulations, **2004**
69. O. R. Inderwildi, Q. Su, D. Lebiez, O. Deutschmann and J. Warnatz, "*Transient simulations of a NO_x decomposition catalyst*", to be submitted **2005**,
70. O. Deutschmann and L. D. Schmidt, "*Modeling the partial oxidation of methane in a short contact time reactor*", AIChE J. **1998**, 44, 2465-2476
71. O. Deutschmann, R. Schwiedernoch, L. I. Maier and D. Chatterjee, "*Natural gas conversion in monolithic catalysts: Interaction of chemical reactions and transport phenomena*" in "*Natural gas conversion VI, Studies in surface science and catalysis 136*", E. Iglesia, J. J. Spivey and T. H. Fleisch (Eds.) **2001**, Elsevier, Amsterdam

72. L. D. Schmidt, O. Deutschmann and J. C. T. Goralski, "*Modeling the partial oxidation of methane to syngas at millisecond contact times*", **1998**, Elsevier, Amsterdam
73. Z.-P. Liu, S. J. Jenkins and D. A. King, "*Step-enhanced selectivity of NO reduction on platinum-group metals*", J. Am. Chem. Soc. **2003**, *125*, 14660-1
74. M. Gierer, A. Barbieri, M. A. V. Hove and G. A. Somorjai, "*Structural reanalysis of the Rh(111) + (3^{0.5} x 3^{0.5})R30°-CO and Rh(111) + (2 x 2)-3CO phases using automated tensor LEED*", Surf. Sci. **1997**, *391*, 176-182
75. I. Zasada, M. A. V. Hove and G. A. Somorjai, "*Reanalysis of the Rh(111)+(2x2)-3NO structure using automated tensor LEED*", Surface Science Letters **1998**, *418*, L89-L93
76. S. Schwegmann, H. Over, V. D. Renzi and G. Ertl, "*The atomic geometry of the O and CO + O phases on Rh(111)*", Surface science **1997**, *375*, 91-106
77. R. S. Mulliken, "*Electronic population analysis on LCAO-MO molecular wave functions. IV. Bonding and antibonding in LCAO and valence-bond theories*", J. Chem. Phys. **1955**, *23*, 2343-2346
78. M. D. Segall, R. Shah, C. J. Pickard and M. C. Payne, "*Population analysis of plane wave electronic structure calculations of bulk materials*", Phys. Rev. B **1996**, *54*, 16317
79. D. J. Siegel, L. G. Hector Jr. and J. B. Adams, "*Adhesion, atomic structure, and bonding at the Al(111) Al₂O₃(0001) interface: A first principles study*", Phys. Rev. B **2003**, *65*, 085415
80. C. Kittel, "*Introduction to solid state physics*", **1986**, Wiley, New York
81. P. Villars and L. D. Calvert, "*Pearson's handbook of crystallographic data for intermetallic phases*", **1985**, OSM, Metals Park
82. A. Eichler, J. Hafner and G. Kresse, "*Hydrogen adsorption on the (100) surfaces of rhodium and palladium: the influence of non-local exchange - correlation interactions*", J. Phys.: Condens. Matter **1996**, *8*, 7659
83. M. V. Ganduglia-Pirovano and M. Scheffler, "*Structural and electronic properties of chemisorbed oxygen on Rh(111)*", Phys. Rev. B **1999**, *59*, 15533-15544
84. A. F. Holleman and E. Wiberg, "*Lehrbuch der Anorganischen Chemie*", **1995**, Walter de Gruyter, Berlin, New York
85. E. J. Walter, S. P. Lewis and A. M. Rappe, "*Investigation of chemisorbed molecular states for oxygen on rhodium (111)*", J. Chem. Phys. **2000**, *113*, 4388-4391
86. O. R. Inderwildi and A. Sundermann, personal communication **2003**

87. R. A. v. Santen and M. Neurock, "*Concepts in theoretical heterogeneous catalytic reactivity*", Catal. Rev. Sci. Eng. **1995**, 37, 557-698
88. R. A. v. Santen, M. C. Zonneville and A. P. J. Jansen, "*The quantum-chemical basis of the catalytic reactivity of transition metals*", Phil. Trans. R. Soc. Lond. A **1992**, 341, 269-281
89. X. Xu and C. M. Friend, "*Partial oxidation without allylic C-H Bond activation: The conversion of propene to acetone on Rh(111)-p(2x1)-0*", J. Am. Chem. Soc. **1991**, 113, 6779-6785
90. G. S. Hammond, "*A correlation of reaction rates*", J. Am. Chem. Soc. **1955**, 77, 334-338
91. D. Loffreda, D. Simon and P. Sautet, "*Structure sensitivity for NO dissociation on palladium and rhodium surfaces*", J. Catal. **2003**, 213, 211-225
92. M. Mavrikakis, J. Rempel, J. Greeley, L. B. Hansen and J. K. Nørskov, "*Atomic and molecular adsorption on Rh(111)*", J. Chem. Phys. **2002**, 117, 6737-6744
93. O. R. Inderwildi, D. Lebiez, O. Deutschmann and J. Warnatz, "*Coverage Dependence of Oxygen Decomposition and Surface Diffusion on Rhodium (111): A DFT Study*", J. Chem. Phys. **2004**,
94. T. W. Root, L. D. Schmidt and G. B. Fisher, "*Adsorption and reaction of nitric oxide and oxygen on Rh(111)*", Surface Science Letters **1983**, 134, A410
95. R. Burch, P. J. Millington and A. P. Walker, "*Mechanism of the selective reduction of nitrogen monoxide on platinum-based catalysts in the presence of excess oxygen*", Appl. Catal. B **1994**, 4, 65-94
96. G. Comelli, V. R. Dhanak, M. Kiskinova, K. C. Prince and R. Rosei, "*Oxygen and nitrogen interaction with rhodium single crystal surfaces*", Surf. Sci. Rep. **1998**, 38, 165-231
97. A. Santoni, B. C. C. Cowie, G. Scarel and V. R. Dhanak, "*The structure of (3^{0.5} x 3^{0.5})R30°-sulphur on Rh(111) surface studied by X-ray standing wavefield absorption and surface EXAFS*", Surf. Sci. **1997**, 388, 254-261
98. K. C. Wong, W. Liu, M. Saidy and K. A. R. Mitchell, "*Tensor LEED analyses for the (3 x 3)R30° and c(4 x 2) structures formed by sulphur chemisorbed on the (111) surface of rhodium*", Surf. Sci. **1996**, 345, 101-109
99. H. Yanagita, H. Fujioka, T. Aruga, N. Takagi and M. Nishijima, "*Vibrational spectra of hydrogen on the Rh(111) surface*", Surf. Sci. **1999**, 441, 507-514

100. O. R. Inderwildi, D. Lebiez, O. Deutschmann and J. Warnatz, "*Influence of co-adsorbants on the NO decomposition on rhodium(311)*", ChemPhysChem **2005**, submitted
101. Q. Su, Simulations, **2005**

13 Appendices






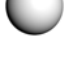
Appendix A: Reaction Mechanism

	A	β	E_a
	[mol,m,s]		[kJ mol ⁻¹]
I Adsorption			
$H_{2(g)} + Rh_{(s)} + Rh_{(s)} \rightarrow H(Rh) + H(Rh)$	$S_0 = 0.015$		
$H_2O_{(g)} + Rh_{(s)} \rightarrow H_2O(Rh)$	$S_0 = 0.01$		
$O_{2(g)} + Rh_{(s)} + Rh_{(s)} \rightarrow O(Rh) + O(Rh)$	$S_0 = 0.01$		
$\theta_{O(Rh)}$			-115.0
$NO_{(g)} + Rh_{(s)} \rightarrow NO(Rh)$	$S_0 = 0.5$		
$N_2O_{(g)} + Rh_{(s)} \rightarrow N_2O(Rh)$	$S_0 = 0.5$		
$CO + Rh_{(s)} \rightarrow CO(Rh)$	$S_0 = 0.5$		
II Desorption			
$H(Rh) + H(Rh) \rightarrow H_{2(g)} + Rh_{(s)} + Rh_{(s)}$	$3.00 \cdot 10^{21}$	0	77.8
$NO(Rh) \rightarrow NO_{(g)} + Rh_{(s)}$	$5.00 \cdot 10^{13}$	0	108.9
$N_2O(Rh) \rightarrow N_2O_{(g)} + Rh_{(s)}$	$1.00 \cdot 10^{13}$	0	50
$\theta_{Rh(s)}$			-100
$\theta_{O(Rh)}$			100
$N_2O(Rh) \rightarrow N_{2(g)} + O(Rh)$	$6.50 \cdot 10^{13}$	0	73.2
$O(Rh) + O(Rh) \rightarrow O_{2(g)} + Rh_{(s)} + Rh_{(s)}$	$3.00 \cdot 10^{21}$	0	293.3
$\theta_{N(Rh)}$			115.0
$CO(Rh) \rightarrow CO_{(g)} + Rh_{(s)}$	$1.00 \cdot 10^{14}$	0	132.3
$\theta_{CO(Rh)}$			18.8
$\theta_{N(Rh)}$			41.9
$N(Rh) + N(Rh) \rightarrow N_{2(g)} + Rh_{(s)} + Rh_{(s)}$	$1.11 \cdot 10^{19}$	0	136.9
$H_2O(Rh) \rightarrow H_2O_{(g)} + Rh_{(s)}$	$3.00 \cdot 10^{13}$	0	45

			A	β	E_a
			[mol,m,s]		[kJ mol ⁻¹]
III Surface Reactions					
H(Rh)	+	O(Rh)	→	OH(Rh) + Rh _(s)	5.00 · 10 ²² 0 83.7
NO(Rh)	+	Rh _(s)	→	N(Rh) + O(Rh)	2.22 · 10 ²² 0 79.5
		$\theta_{\text{O(Rh)}}$			-50
NO(Rh)	+	N(Rh)	→	N ₂ O(Rh) + Rh _(s)	3.68 · 10 ²¹ 0 79.5
OH(Rh)	+	Rh _(s)	→	H(Rh) + O(Rh)	3.00 · 10 ²⁰ 0 37.7
H(Rh)	+	OH(Rh)	→	H ₂ O(Rh) + Rh _(s)	3.00 · 10 ²⁰ 0 33.5
H ₂ O(Rh)	+	Rh _(s)	→	OH(Rh) + H(Rh)	5.00 · 10 ²² 0 106.4
OH(Rh)	+	OH(Rh)	→	H ₂ O(Rh) + O(Rh)	3.00 · 10 ²¹ 0 100.8
H ₂ O(Rh)	+	O(Rh)	→	OH(Rh) + OH(Rh)	3.00 · 10 ²¹ 0 224.2
CO(Rh)	+	O(Rh)	→	CO _{2(g)} + Rh _(s) + Rh _(s)	3.70 · 10 ²⁰ 0 59.9

Nota bene: Rh_(s) denotes a free adsorption site on solid rhodium, species followed by (Rh) denote that they are adsorbed on a such a solid rhodium adsorption sites (Rh_(s)), *e.g.*, CO(Rh) denotes CO adsorbed on Rh_(s). Within the mean field approach the surface is considered uniform and therefore only one possible adsorption site (Rh_(s)) is given.

Appendix B: Atom Colouring in Surface Visualisations (Chapters 4 to 8)

Atom	Visualisation
Rhodium	
Oxygen	
Nitrogen	
Carbon	
Sulphur	
Hydrogen	

Appendix C: Catalyst characterisation & Experimental Techniques (Chapters 3 & 9)

Catalyst characterisation

Washcoat loading	8.11 g
Number of channels of the monolith reactor	9
Binding material	4.03 g
Rhodium loading	0.3 mg 2.92 μ mol
Active rhodium surface (determined by CO chemisorption)	0.80 m ² /g
$F_{\text{cat/geom}}$ (Active rhodium surface/surface of the catalysts inner wall)	110
Channel diameter	1 mm
Channel length	30mm
Superficial velocity (STP)	0.926 m/s

Experimental Techniques

Analytic Tool	Model	Manufacturer
FT-IR spectrometer	Protégé 460	Nicolet
Mass spectrometer (Quadropol)	QMG 422	Pfeiffer
Lambda sensor	LSU 4.2	Bosch
Nitrogen oxide analyser	CLD 700 EL ht	Ecophysics

Danksagung

Herrn Prof. Dr. Dr. h.c. Jürgen Warnatz und Herrn Prof. Dr. Olaf Deutschmann danke ich für die Bereitstellung der interessanten Aufgabenstellung und die Betreuung der Arbeit.

Dr. Dirk Lebiedz danke ich für die tägliche wissenschaftliche Betreuung sowie für die Unterstützung an vielen kritischen Punkten.

Dr. Steffen Tischer möchte ich meinen Dank für die vielfältigen Hilfestellungen bei der Programmierung des in der Arbeit verwandten DETCHEM-Moduls aussprechen.

Herrn Qingyun Su M.Sc. und allen anderen Kollegen der Forschungsgruppe „Reaktive Strömungen“ möchte ich für die kollegiale Zusammenarbeit danken.

PD Dr. Hans-Robert Volpp, Herrn Prof. Dr. Jürgen Wolfrum sowie allen Kollegen am Physikalisch-Chemischen Instituts möchte ich für die angenehme und gewinnbringende Zusammenarbeit danken.

Des Weiteren möchte ich den Mitgliedern des ConNeCat-Arbeitskreises „Ruß und NO_x aus Dieselabgasen“ für die anregenden Diskussionen im Rahmen der Projekttreffen danken.

Im Speziellen möchte ich Herrn Dr. W. Strehlau, Frau Dr. O. Gerlach, Herrn Dipl.-Ing. J. Maier, Dr. F. Rohr und Herrn Dr. A. Sundermann danken.

PD Dr. Uwe Riedel möchte ich meinen Dank für die Unterstützung in allen organisatorischen Fragen aussprechen.

Herrn Ravindra Aglave M.Sc. möchte ich für das Korrekturlesen der Arbeit und die daraus entstehenden Diskussionen danken.

Bei Frau Ingrid Hellwig und allen anderen Mitarbeiterinnen des Sekretariats möchte ich mich für die Unterstützung bei allen Verwaltungsangelegenheiten bedanken.

Auch möchte ich meiner Familie für die jahrelange Unterstützung danken ohne die diese Arbeit nicht zustande gekommen wäre.

Last but not least, Herrn Dr. Joost Reek der mir vor dem Aufgeben gezeigt hat, dass Chemie doch Spaß macht.

Diese Arbeit wurde finanziert durch das Bundesministerium für Bildung und Forschung (BMBF) durch ein ConNeCat-Leuchtturmprojekt, das Bundesministerium für Wirtschaft und Arbeit (BMWA) sowie über den Sonderforschungsbereich 359 der Deutschen Forschungsgemeinschaft.

Erklärung

Hiermit versichere ich, dass ich diese Arbeit selbstständig verfasst habe und keine anderen als die angegebenen Quellen und Hilfsmittel verwendet habe.

Heidelberg, den

